PHOTODYNAMIC ANTICANCER AND ANTIMICROBIAL ACTIVITIES OF NOVEL BACTERIOCHLORINS

A thesis submitted to Rhodes University in partial fulfilment of the requirements for the degree of

Master of Science (Chemistry)

By

KAISANO G. TAUYAKHALE

Supervisor: **Professor John Mack**

Co-supervisor: **Dist. Prof Tebello Nyokong**

Dedication

This goes out to the marginalised, the underdogs, the 'unworthy ones', the ones who have had far too many downs than ups in their lives, the ones who have been waiting for the light at the end of the tunnel for so long that the dark doesn't deter them anymore. I am talking about the ones who have to work twice, if not thrice as much, in order to just be acknowledged, the ones who have so many odds stacked against them that daring to believe is simply daunting, but they choose to anyway.

-KG.

"The wisdom of God tells us that God will bring about the best possible results, by the best possible means, for the most possible people, for the longest possible time." -*Charles Ryrie*

Acknowledgements

This is going to be a mouthful…

Well, without Jesus, I would have probably dropped out and given up a long time ago, but I am still here. I am grateful for the relationship I have with HIM. HE is my Unconditional Friend, Lover of my Soul, and MY GOD.

Prof John Mack, I still cannot “see” the potential you “see” in me. Your confidence and surety of my being a researcher, coupled with your support, patience, and tolerance of my being a maverick (to say the least), are really encouraging, and I thank you.

Prof Tebello Nyokong, thank you for installing a culture of hard-work, determination and confidence (in particular the emphasis on presentations, it is a pain, it is daunting but I am beginning to realise how crucial it is).

To the S22 “LEADERSHIP”, I really appreciate the peer-pressurising work ethic, humour and intellectual stimulation (which is nowhere near meant to sound sarcastic). Multi, thank you for the beakers and columns (even though you either broke or lost them, it is the gesture that counts 😂) and for those impromptu venting sessions. They helped. To Leadership, Leader, Leader, Leader, my Leader, Comrade, Veteran and Honourable member (if I have called you by any of these names), thank you for making the journey bearable 😁.

Choonzo and Mahlatse, thank you for bending over backwards for me by choosing to help me. I really appreciate it. Kris, that dark sense of humour and banter did wonders, mate.

To the Fam…Deputy parents, GM 😘, Nephews, Nieces, Bestie and Ps I and Mama Milcah, thank you for the prayers and the encouragement. They were a crutch in times of despondency. Witness aka Witty aka Weetbix aka Foundation Ya Papa aka Skhokho, thank you for always being there and choosing to be my friend given that I am very awkward. It means a lot ngwana wakokgae🙈.

Lastly, I would like to thank Rhodes University and the Pearson-Young Memorial Trust for funding my MSc studies.

ABSTRACT

The World Health Organization cautioned that the major contributing factors of cancer amongst people are the excessive usage of alcohol, smoking, lack of exercise and low intake of fruits, vegetables, and high-fibre foods. Furthermore, cancer by far is reported to be the most common and leading cause of death worldwide (1 in 6 deaths is due to cancer). Moreover, it is reported that cancer kills more people than tuberculosis, malaria and AIDS combined every year. Chemotherapy has been utilised as a mode of rehabilitation for complete being used in conjunction with surgery or to improve the state of well-being of patients until their point of death. However, it is well known for its adverse effects, such as loss of hair, altered gastric metabolism, vomiting and nausea, dehydration, weight loss, and loss of appetite. For this reason, photodynamic therapy (PDT) was developed as an alternative. A molecular dye (photosensitiser/PS) and light of a specific wavelength produce cytotoxic singlet oxygen species, which induce cell death.

The aim of this project is to prepare novel structurally modified porphyrin-type dyes that absorb far into the near-infrared region. Identifying suitable dyes that absorb significantly in the 700−800 nm region is particularly important from an African perspective, since melanin significantly limits the penetration of laser light into human tissue in the 600−700 nm region, where first- and second-generation photosensitiser dyes usually absorb. The porphyrin analogues that will be investigated in this regard are bacteriochlorins (BChls), which are known to have suitable optical properties that are potentially suitable in this regard.

The first step of the study would be to synthesise tetraarylporphyrins with electron-withdrawing *meso*-aryl rings because their reduction to BChls is more readily

attainable than is the case with electron-donating rings. However, these contrasting properties can be combined to tailor the BChls for effective photodynamic therapy, so the type of porphyrins synthesised will be tetraarylBChls with different *meso*-aryl groups to first analyze the induction of different chemical properties in this case, the impact of introducing electron donating (4- and 3-quinoline substituents) or electron-withdrawing (pentafluorophenyl substituents) groups on the *meso*-positions of the dyes and more specifically whether the position of the quinoline nitrogen atom relative to the core of the BChl has any significant impact on the reactivity of the dye (the 4- or 3-position of the quinoline).

The next factor to be considered is the induction of the heavy atom effect by introducing a metal in the centre of the dye in order to try to increase the singlet oxygen quantum yields for high production of reactive oxygen species and singlet oxygen and further red shift the lowest energy absorption band of the BChls in the therapeutic window for deep tissue penetration for effective. Lastly, the goal will be to explore whether the delivery of bacteriochlorin photosensitisers to cancer cells can be enhanced by introducing quaternised nitrogen atoms to the *meso*-aryl ligands.

Legend

Table of Contents

List of Figures

List of Schemes

List of Tables

List of Symbols

^{o}	Degrees
Δ	Change in/delta
ε	Molar extinction coefficient
f	Oscillator strength
IC_{50}	Half-maximal inhibitory concentration
λ	Wavelength
μM	Micromolar
Φ_F	Fluorescence quantum yields
Φ_Δ	Singlet oxygen quantum yield
S_0	Ground state
S_1	First singlet excited state
T_1	First triplet excited state
τ_T	Triplet state lifetime

List of Abbreviations

^{1}H NMR	Proton Nuclear Magnetic Resonance
B3LYP	Becke, 3-parameter, Lee–Yang–Parr
BChl	Bacteriochlorin
BSA	Bovine serum albumin (BSA)
CAM-B3LYP	Coloumb-attenuating method-B3LYP
Chl	Chlorin
BCE	Before Christian Era
CFU	Colony forming units
DMA	9,10-Dimethylanthracene
DMEM	Dulbecco's modified Eagle's medium
DMSO	Dimethylsulfoxide
DNA	Deoxyribonucleic acid
DPBS	Dulbecco's phosphate-buffered saline
DPBF	1,3-Diphenylisobenzofuran
FCS	Fetal calf serum
FDA	Food and Drug Administration
HOMO	Highest occupied molecular orbital
HSA	Human serum albumin
ISC	Intersystem crossing
Laser	Light Amplification by Stimulated Emission of Radiation
LED	Light-emitting diode
LUMO	Lowest unoccupied molecular orbital
MALDI-TOF	Matrix-assisted laser desorption/ionisation time-of-flight
MCF-7	Breast cancer cell line
MO	Molecular orbital
MS	Mass spectrometry
MTT	Trypan blue and tetrazolium dye

Nd:YAG	Neodymium-doped yttrium aluminum garnet
PACT	Photodynamic antimicrobial chemotherapy
PBS	Phosphate-buffered saline
PDT	Photodynamic therapy
PET	Photoelectron transfer
PS	Photosensitiser
ROS	Reactive oxygen species
TD-DFT	Time-dependent density functional theory
TFA	Trifluoroacetic acid
TLC	Thin-layer chromatography
TPP^+	Triphenylphosphonium
UV-vis	Ultraviolet visible
ZnTPP	Zinc tetraphenylporphyrin

1.INTRODUCTION

1.1 History of Cancer

Karkinos, now called cancer in English, was coined by a Greek physician called Hippocrates to describe carcinoma tumours.[1] The task of trying to cure cancer has been in progress since around 1500 BCE, with the oldest case being a breast cancer record in the Egyptian archives.[2] Cancerous cells develop from healthy ones due to unrepairable deoxyribonucleic acid (DNA) damage. These cells with damaged DNA are said to be mutations that can either be benign, i.e. harmless, or malignant, i.e. fatal. This happens when mutated cells possess elevated abilities to proliferate, dividing at uncontrollable rates, and is referred to as hyperplasia.[3] There are two types of cancerous cells, namely *in situ* and invasive. The *in situ* type involves mutated cells that have not penetrated through any boundaries between the adjacent tissues and are usually contained and, therefore, not that lethal. The invasive type, on the other hand, refers to mutated cells not only invading/penetrating the underlying tissues but also shed their cells into the lymph nodes or in the bloodstream, which will, in turn, form more tumours and may end up disrupting the function of vital organs as illustrated by **Figure 1** below.[4]

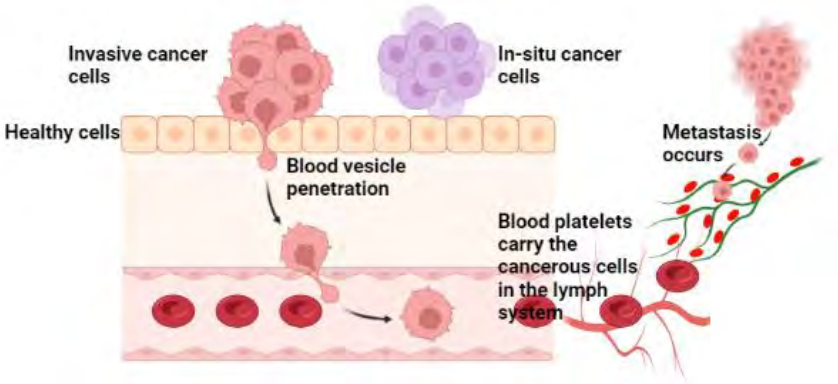

Figure 1: A schematic diagram showing the major differences between the invasive and *in situ* types of cancerous cells.

1.2 Cancer therapies

The National Cancer Institute states that there are several different cancer therapies, starting with the primitive and still effective approaches to the more recently discovered[5], **Figure 2**.

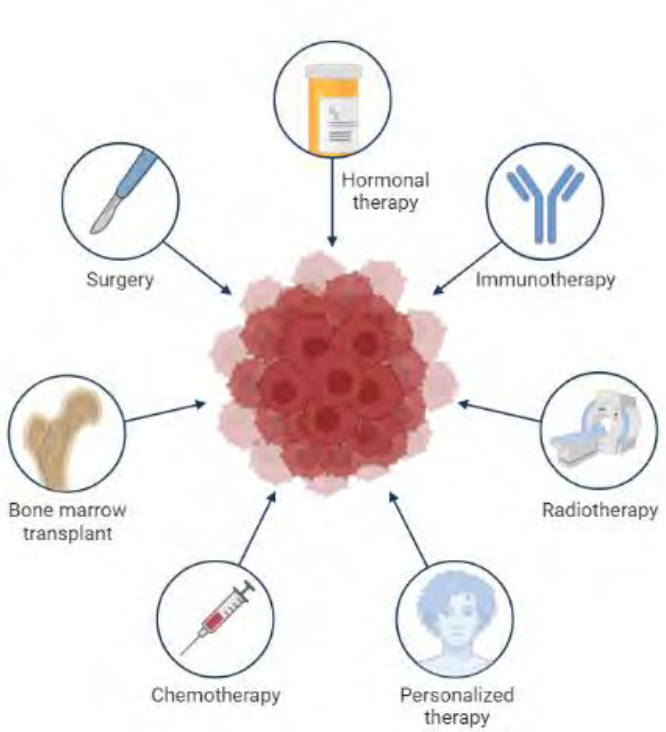

Figure 2: A scheme showing the different therapeutic techniques for cancer.

Surgery

Surgically removing cancer cells has been practised for several generations and is claimed to be the most efficient way of eradicating cancer. This type of therapy is said to be a local type of treatment, since it treats only the part of the body with the cancer. Furthermore, surgery can be used to remove the entire tumour or debulk the tumour, i.e. to remove a fraction of the tumour. This is done to reduce the risk involved if the whole tumour is removed, which might damage the host organ, or to help other

treatments work better by lowering the pain or pressure of cancer symptoms.[7] Surgery relies heavily on anaesthesia (drugs that cause loss of physical feeling). There are local, regional, and general anaesthesia, which, respectively, cause a loss of feeling in one small area of the body, a specific part of the body (like the leg or arm), and lastly, a complete loss of feeling and awareness.[8] Be it as it may, this treatment type has its limitations because as mutations become more and more complex, like in the case of leukaemia, which is reported to produce liquid tumours instead of solid ones, with their origin site often undetermined (because of their constant movement within the blood vesicles).[9] For this reason, amongst others, more accommodating/effective therapeutic routes were explored.

Hormonal therapy

The second type of treatment is hormone therapy. It is used to slow down or stop the tumour growth. It is reported that it can only be used to remedy cancer symptoms of prostate cancer amongst other hormone-dependent tumours.[10] Hormonal therapies fall under two major categories, namely those that block the ability of the body to produce hormones and those that alter/interfere with the behaviour of hormones in the body.[11] For this therapy to be efficient, it has to be used in conjunction with other therapies, such as making a tumour smaller before surgery or radiation therapy. This is called neoadjuvant therapy. Another reason is to lower the probability of the tumour coming back after the main therapy. This is referred to as adjuvant therapy.[12] The treatment is administered orally in the form of pills, intravenously into the arm, thigh, hip muscles or in the belly fat or *via* surgery where the organ producing certain hormones is removed (ovaries or testicles in women and men respectively).[13] This has

some drawbacks, such as hormonal side effects, including fatigue, nausea, mood swings, hot flashes and diarrhoea, to mention the least. The obvious limitation of this treatment is that it can only be used to remedy cancers that rely on hormones to grow.

Immunotherapy

The third therapy is immunotherapy, which is used to help the immune system combat cancer.[14] The immune system acts naturally against foreign and or harmful objects. It becomes tricky when it comes to cancer because these cells can elude the immune system, like in the case of them having surface proteins that turn off the immune system or alter the normal cells around the cancerous cells so that they interfere with how the immune system usually responds to cancerous cells.[15] There are about five categories of immunotherapy treatments. Firstly, immune checkpoint inhibitors regulate the sensitivity of the immune system. T-cell transfer therapy improves the action of T-cells to attack cancer cells. This is done by selecting and transferring the most effective T-cells in the body against cancer cells. These are then modified in the laboratory, replicated and transferred back into the body intravenously. The following type of immune therapy is the use of Monoclonal antibodies. These antibodies are modulated in the laboratory and are used to mark or target cancer cells. The other alternative is the use of vaccines, which are primarily used to boost the immune system and are similar to immune system modulators as the last immune therapy.[14,15] The modes of administration of this type of therapy are intravenously (to the veins), intravesically (to the bladder), orally (pills and capsules), and topically (to the external surface of the body). Nevertheless, there are some effects apart from resistance from the cancer cells. The major one is the action of the modified immune system against normal healthy cells.[16]

Stem cell transplant

Another type of cancer therapy is stem cell transplant/bone marrow transplant. These treatments restore blood-forming stem cells, which grow into an array of blood cell types (white blood cells for the immune system, red blood cells for oxygen transportation and platelets for clothing).[17] It is reported that this therapy does not usually work directly against cancer cells but instead helps the body recover its ability to form stem cells. Examples of rare cases of stem cells acting against cancer cells are leukaemia or multiple myeloma. This arises because of the graft-versus-tumour effect, which happens when white blood cells from the graft (donor) attack cancer cells that remain in the body after high-dose treatments.[18] This treatment is administered intravenously. Healthy blood-forming stem cells from the umbilical cord, bloodstream or the bone marrow of the donor enter the bloodstream and travel to the bone marrow, replacing the destroyed stem cells and begin forming blood cells. The transplants can either be autologous (this means that the healthy stem cells were taken from the patient), allogeneic (the stem cells were donated by someone else who is blood-related), and lastly, syngeneic (the stem cells were taken from a biological twin).[6] One of the effects of this type of treatment is graft-*versus*-host disease, whereby the white blood cells from the donor recognise the cells in the body of the host as foreign and attack them, damaging the internal and external organs.[19]

Hyperthermia

The fifth type of cancer therapy is hyperthermia/thermal therapy or thermal ablation. This treatment uses heating to *ca.* 45°C to eradicate cancer cells with little harm to healthy cells[20]. Different techniques can be used to create heat for this type of treatment, such as ultrasound, lasers, radio waves, heating fluids, microwave probes

and/or putting the body in a heated chamber/hot water or wrapping the patient with heated blankets.[21] This treatment can be used along with other treatments like radiation and chemotherapy to shrink cancer cells. The treatment area is numbed, tiny thermometer probes are inserted into the tumour, and CT scans are used for imagery. There are many types of hyperthermia, categorised by the intensity, mode of administration and target organs, including local, external, intraluminal or endocavitary, interstitial and regional hyperthermia.[20,6] Because this treatment is heat-based, the major side effects are burns, blisters, pain and altered metabolism, including diarrhoea, nausea and vomiting.[22]

Radiotherapy

Radiotherapy uses radiation to obliterate cancer cells and shrink tumours.[23] Radiation at high doses damages the DNA of cancer cells and hence destroys them. It does this over a prolonged period. There are two categories of radiation therapy, namely internal and external beam radiation therapy, depending on the type of cancer treated, its location, its size, age, health, and other medical conditions of the patient.[24] External beam therapy utilises a large spinning machine that directs radiation at the cancer site from different angles. On the other hand, internal therapy uses a liquid source (systematic therapy), meaning that the liquid travels intravenously to tissues seeking cancerous cells. These treatments can also remedy cancer symptoms, such as breathing irregularities, abnormal bowel movement, bladder control, joint and bone pains and radiopharmaceuticals.[25] This type of treatment, however, is also notorious for destroying healthy cells as well.

Chemotherapy

The use of chemicals to alleviate or eradicate cancer has been explored for decades, and one prevailing method thus far has been reported to be chemotherapy.[26] The term chemotherapy describes the use of chemicals to inhibit malignant cells or micro-organisms without interfering with the host cell. The first reported chemotherapy procedure was in the 1940s after World War II.[27] Based on the use of nitrogen mustards during the war, these organic compounds were determined to exhibit cytotoxic properties on the lymphatic system. They were then used to treat patients with lymphoma, and their tumours relapsed.

During the 1950s, the metabolism of these compounds was studied in depth, and it was found that they disrupt the DNA structure by adding alkyl groups to the guanine base, which prevents the cells from growing and hinders their mitotic process.[28] This led to the discovery of antimetabolites, such as methotrexate, cytarabine, 5-fluorouracil and many more. The 1960s to 1980s marked the revolution of chemotherapeutic compounds with the discovery of cisplatin, which was found to be very effective against a wide range of solid tumours. Moreover, the discovery of taxane was significant, and topoisomerase inhibitors have shown high activity against breast cancer.[29]

The chemotherapy procedure involves the intravenous, injection, intrathecal, intraperitoneal, intra-arterial, topical and oral administration of the cytotoxic drug at specific time intervals over a period of *ca.* 20 to 28 days, varying with the type of drug used, on most occasions, the compounds are combined for targeting and remission.[30] Total remission (a decrease or disappearance of signs and symptoms) is reported to be highly rare, while partial remission is often the result. It is believed that this is due

to the lack of sensitivity of the tumour cells.[31] Nonetheless, chemotherapy is reported to cause damage to not only the surrounding cells but sometimes organs too and thereby cause effects such as fatigue, nausea, hair loss and mouth sores.[32] This is said to be because the drugs used in chemotherapy “kill” rapidly dividing cells because malignant tumour cells divide rapidly, but the problem arises when these drugs kill normal healthy cells that divide rapidly, such as hair cells, nail cells and other rapid metabolic processes in the body.[33]

Photodynamic therapy

The last type of therapy that is of particular interest for this study is photodynamic therapy. It will be discussed thoroughly and compared to the previously mentioned therapies above because it will be the main application for this study.

Photodynamic therapy (PDT) was developed to provide a more effective alternative therapy than chemotherapy and radiation therapy. This type of therapy utilises a molecular dye (photosensitiser/PS) and light of a specific wavelength to produce cytotoxic singlet oxygen species, which induce cell death, **Figure 2**.[34] This procedure is relatively benign compared to chemotherapy because the PS used can be modified to target only cancer cells, and most importantly, they are usually derivatives or naturally occurring metabolic molecules, so this means that they do not pose a threat to the immune system or metabolic processes when administered and thereby not cause any adverse effects.[35]

PDT has been the subject of intense study in recent decades, since it provides an alternative to other treatments, such as chemotherapy and surgery, for treating not only cancer but also microbial infections.[36] PDT is more effective when dealing with

tumours that are readily accessible with Ultraviolet-visible light (UV-vis), such as skin, oesophagus, bladder, urinary, ophthalmologic and lung cancers.

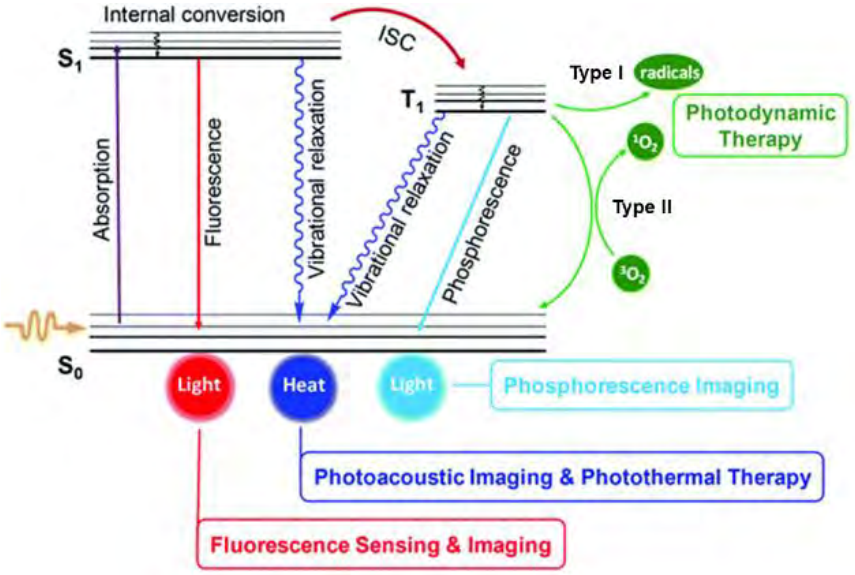

Figure 3: A Jablonski diagram illustrating the photophysical processes of a molecule upon photoexcitation. Reproduced with permission from Ref. 37, © Royal Society of Chemistry 1972.

PDT depends upon the combined action of light, a photosensitiser dye and molecular oxygen to cause tissue and cellular damage.[37] When a photosensitiser dye absorbs an incident photon (**Figure 3**), the absorbed energy is transferred to the ground state triplet state of molecular dioxygen to generate highly reactive singlet oxygen, $^1O_2$ (type II mechanism of action), which is believed to be the main cytotoxic species that is responsible for the observed damage to cancer tumours during PDT.[37,38] In Type I, however, reactive oxygen species (ROS) are formed instead, which in turn induce microbial death and that is referred to as photodynamic antimicrobial chemotherapy (PACT).[39] The PS dyes explored thus far include several porphyrin and phthalocyanine dyes that have been approved for use in this context, but there is still a need to identify new dyes with more favourable properties for this application.[40]

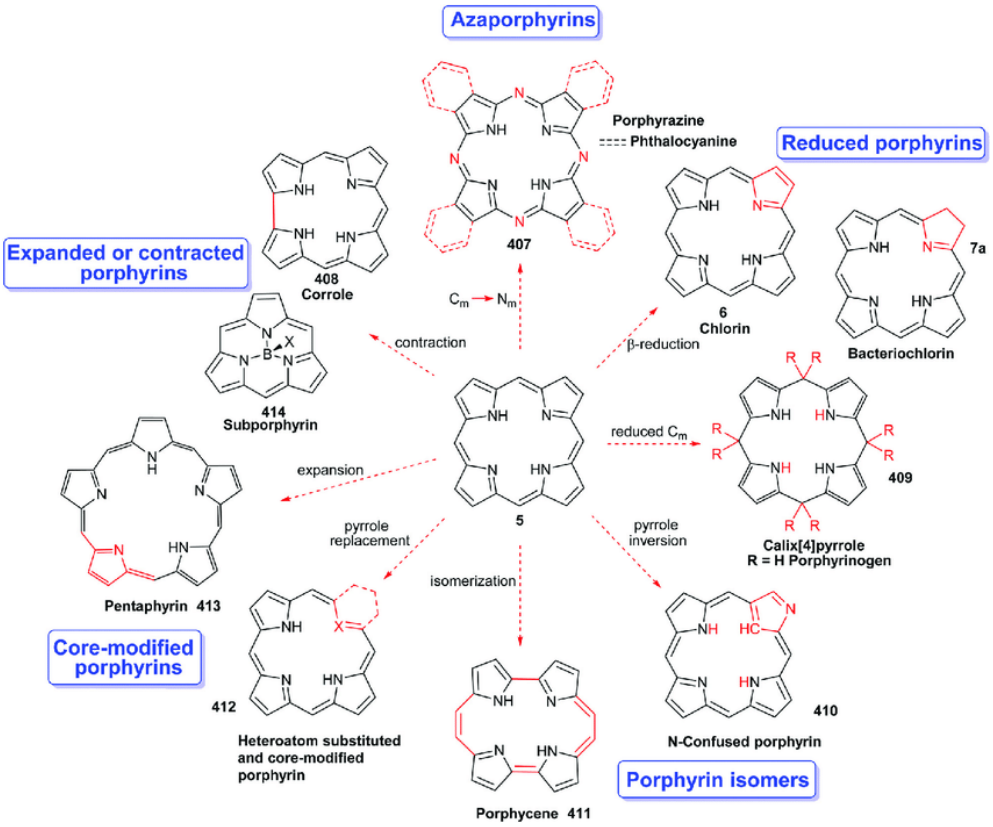

Figure 4: Different porphyrinoids stemming from the free base. Reproduced with permission from Ref. 40, © Royal Society of Chemistry 2021.

The main drawback with the first porphyrin-base photosensitiser dye (**Figure 4**), Photofrin®, is that it absorbs very weakly in the therapeutic window (620−850 nm) in which human tissue is optically transparent to incident laser light at around 620 nm. As a result, relatively high concentrations have to be used.[41] Furthermore, it is reported that it takes a long time for this PS to be expelled from the body after treatment. Patients, therefore, have to avoid direct sunlight for prolonged periods after their treatment. A second generation of phthalocyanine photosensitisers were later developed.[42] Although phthalocyanines have intense bands in the therapeutic window, their large planar π-systems limit their solubility and make these dyes prone to aggregation, which can deactivate their photophysical properties and their ability to generate singlet oxygen.[41,42,43] There is an ongoing need to develop photosensitiser

dyes with more favourable properties for PDT. This project will focus on using novel bacteriochlorins as PS dyes for PDT.

1.3 Photosentiser dyes

Photosensitisers are chromophores/dyes/nanoparticles/metal complexes that absorb visible region light. These dyes can sensitise the triplet oxygen in the vicinity after absorbing light to produce reactive oxygen species like hydrogen peroxide, superoxide (radical anion), hydroxyl radical or singlet oxygen.[43] These radicals are reported to effectively oxidise a variety of biomolecules and thereby cause damage, whereas $^1O_2$ usually causes oxidation of biomolecules such as lipids and proteins and hence cell death. In order for PDT and PACT to be efficient, the PS must have the folowing:

1.3.1. Suitable optical properties

The PS must have a high extinction coefficient (ε) at the excitation wavelength. This parameter is related to the maximal absorption of light of a specific wavelength in the near-infrared (NIR) region for deep tissue penetration.[44] The extinct coefficient is a quantity that determines how deep an object absorbs or reflects light of a specific wavelength.[45] The log ε value ideally should be > 5. This property depends on properties such as the concentration of the absorbing solution per volume, chemical structure and atomic makeup of the chromophore, its molecular weight, molecular refractivity, its solubility, polarity, pathlength, which is the distance that the light travels through the solution and most importantly the intensity of the radiation and its wavelength. Deep tissue penetration can be attained by taking into consideration the therapeutic window when synthesizing the appropriate PS. The therapeutic window is the spectral region where most endogenous molecules such as haemoglobin, water molecules and most metabolic proteins do not absorb light (**Figure 5**).[46]

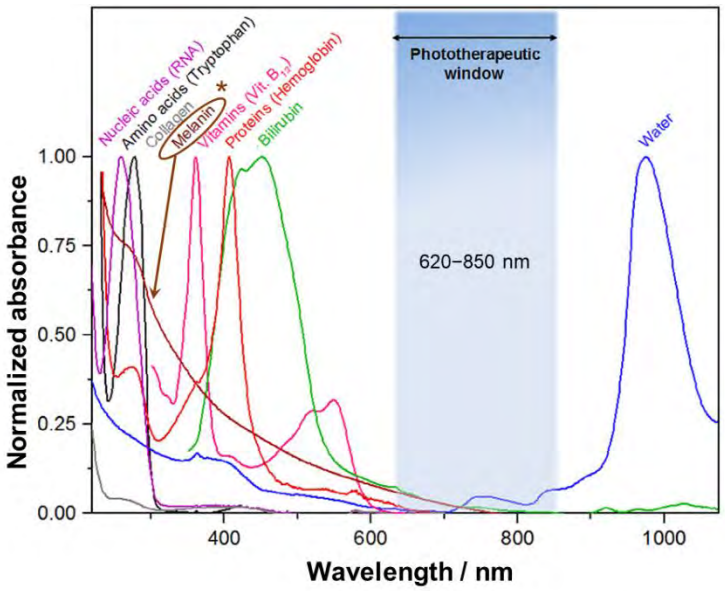

Figure 5: The therapeutic window for optical penetration of tissue. A second generation of phthalocyanine photosensitisers was later developed. Reproduced with permission from Ref. 136, © Elsevier 2016.

In this region, the human tissue is optically transparent to incident light around 620 nm to *ca.* 850 nm. So ideally, the PS used should absorb light at this region not only for deep tissue penetration but also to not interfere with the metabolic properties of the body.[47] Moreover, this is very significant from an African perspective, since melanin significantly limits the penetration of laser light into human tissue in the 600−700 nm region, where the first and second generations of PS dyes usually absorb (**Figure 5**).

1.3.2. Long triplet lifetimes

Efficient intersystem crossing (ISC) is a prerequisite for generating singlet oxygen and other reactive oxygen species.[48] As indicated above by the Jablonski diagram, upon irradiation, the PS gains energy and goes up to the triple excited state where either it will lose its energy and fall back into the ground state *via* fluorescence/vibrational relaxation, or it can undergo ISC. ISC is the nonradiative transition between two electronic states of different multiplicity (**Figure 6**).[49]

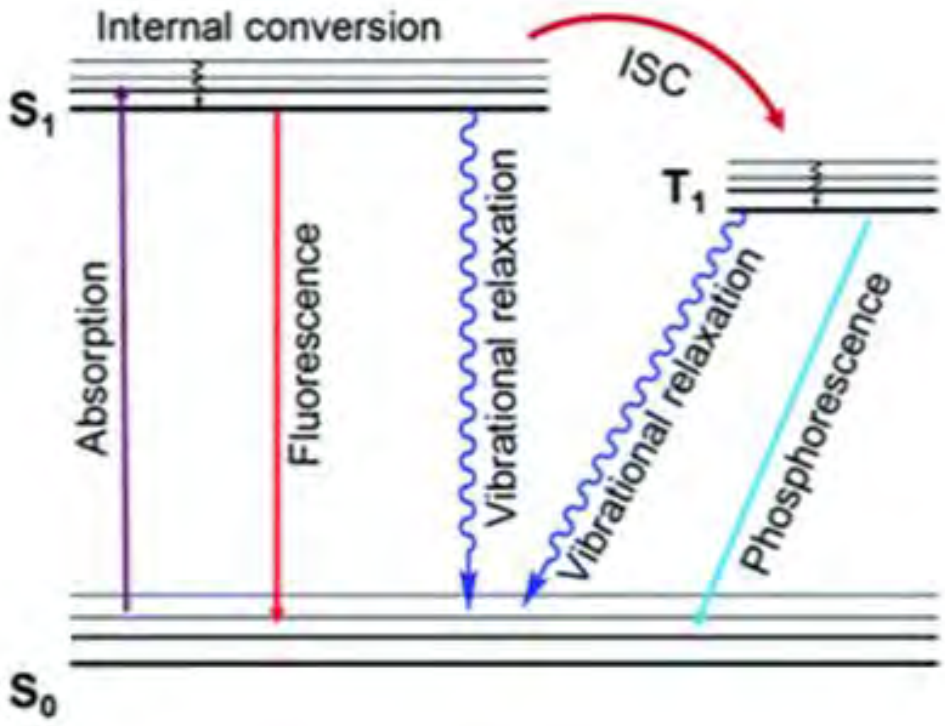

Figure 6: A detailed schematic of the ISC conversion. Reproduced with permission from Ref. 37, © Royal Society of Chemistry 1972.

After the photoexcitation of the PS, radiative and nonradiative deactivation occurs, followed by internal conversion (IC), which is the nonradioactive transition between two states of equal spin multiplicity. Then, the photons are emitted exclusively from the lowest excited state of the given multiplicity (i.e. Kasha's rule). Lastly, ISC, the nonradiative transition between two states of different multiplicity, occurs. The rate at which the triplet state is populated or depopulated plays a role in the functional properties of a chromophore. High triplet quantum yield coupled with a slow ISC leads to photobiological transformations, in this case, the production of $^1O_2$/ROS. On the contrary, compounds with deactivated triplet states are said to be quenchers and thereby increase the photostability of chromophores.[50]

1.3.3. High photo and chemical stability

The PS should remain integral throughout the irradiation process. The photostability and photosensitising ability of a chromophore may be influenced by minor changes in its molecular structure.[51] The "heavy atom effect" is a well-known illustration of this phenomenon, whereby swapping over a lower-atomic-number atom for a higher-atomic-number one increases the likelihood that a triplet state would develop, triggering a photosensitisation reaction. The qualities of a compound as a photosensitiser are typically improved by replacing hydrogen with a halide. For instance, the bromination of Rhodamine 123 to form tetrabromorhodamine 123 boosts the singlet oxygen quantum yield by around 50 times. Increasing the π-conjugation bond length is reported to be another factor that can either stabilise or destabilise most PS dyes.[51,52]

A perfect example would be the mesomeric effect, which is the change of polarity induced by the alternating π bonds and sometimes the introduction of electron donating or withdrawing groups on the chromophore. This can result in a red shifting of its wavelength into the infrared region.[53] On the topic of polarisation, it is reported that introducing polar/nonpolar charges influences changes in the photophysical properties of chromophores. The other factor to consider is the conjugation of nanomaterial to chromophores. It is reported that this improves the rigidity and thermal stability of the chromophores. By extension, the addition of bulky groups, whether on the ortho, para or *meso* positions, on cyclic chromophores decreases aggregation and thereby reduces photobleaching, which is when a fluorophore loses its fluorescence permanently as a result of covalent alteration and photon-induced chemical degradation.[54]

1.3.4. High water solubility and cancer cell localisation

Amphiphilic compounds can be produced *via* the ester, amide, urea, hydrazone, and carbamate bonding of polysaccharides with hydroxyl, carboxylic acid, and amino functional groups with a variety of hydrophobic moieties.[55] Small hydrophobic compounds like bile acids, fatty acids, and cholesterol, as well as macrohydrophobic substances like polyester and polyanhydride and hydrophobic pharmaceuticals like paclitaxel, are among the hydrophobic moieties. The covalent chemical linkages between polysaccharides and hydrophobic moieties may be labile for effective drug release, such as pH-sensitive (hydrazone bond), enzyme-cleavable (ester bond), and reductive (disulfide bond) approaches under cancer cell circumstances.[56] Hydrophobic interactions cause the resulting amphiphilic polymers to have a tendency to self-assemble into NPs in an aquatic environment.[57]

Examples of non-covalent interactions are electromagnetic contact, host-guest recognition, π-π stacking, hydrogen bonding, metal-ligand interactions, and charge transfer interactions. Such interactions are frequently weaker than covalent ones. The resulting amphiphilic complexes are typically classified as supramolecular amphiphiles since they are created from such non-covalent interactions (namely superamphiphiles).[58] Because of their unique characteristics, these supramolecular amphiphiles show promise as stimuli-responsive nanocarriers. The most often employed non-covalent interactions used to create supramolecular amphiphilic systems in carbohydrate-based amphiphilic systems for drug delivery include electrostatic interaction, host-guest recognition, π-π stacking, or the combined use of these processes.[59]

Ionic cross-linkers use electrostatic attraction between molecules with cationic and anionic groups to combine molecules to create polyelectrolytes, which are

macromolecules with charges. Many NPs can be self-assembled from some polyelectrolytic complexes.[60] The less stable ionic cross-linker networks, however, cause the resultant NPs to be labile in the external environment. In general, both internal and external factors of polyelectrolytes, including ionic strength, temperature, chain flexibility, pH level, and mixing method, affect the formation and stability of complexes.[61] Internal factors of polyelectrolytes include charge density, chain flexibility, molecular weight, and charge distribution. Polysaccharides play a crucial role in the formation of polyelectrolytes.[60,61,62] For instance, negatively-charged hyaluronan, heparin, and positively-charged chitosan can all combine with other polyelectrolytes (polysaccharides, for example) to create complexes.

Non-covalent interactions between aromatic rings are referred to as π-π stacking. Catalysis, interactions between proteins and ligands, and molecular recognition all heavily rely on these interactions.[63] Intermolecular π-π stacking attraction has recently received more interest and has been used for medication delivery. Drugs with aromatic (π-rich) groups, such as the anti-cancer medication doxorubicin, and aromatic (π-rich) groups in nanostructures, such as graphene, carbon nanotubes, fullerene, and carbon black nanoparticles, can be used to create this kind of drug delivery system.[64] These carbon nanostructures, however, are unable to disperse in water without suitable surface modification, which restricts their use. Because polysaccharides are often biocompatible and biodegradable, they are well suited to be conjugated with aromatic moieties for the intermolecular stacking attraction-based transport of aromatic medicines.[65] Conversely, non-aromatic medicines can likewise be changed into Prodrugs that can introduce aromatic moieties through cleavable chemical bonds suitable for drug delivery.

In addition to π-π stacking, hydrophobic interactions can also have a synergistic effect on drug encapsulation and self-assembly to produce nanostructures such as micelles or vesicles.[66] Lastly, apart from using the delivery strategy to solubilise the PS dye, the most recent and highly effective PS solubility strategies include quaternisation, which is the charging of the alkyl halide functional group or conjugating with a positively charged/hydrophilic moiety on the PS (whereby a cationic charge is introduced).[67] This does not only help with solubility but also helps with localizing and binding the PS to negatively-charged cell membranes like *E. coli* during PACT, while during PDT, it is used to exploit the fact that cancerous cells have a higher than normal negative electrical charge.[68] This is primarily because, under normal metabolic processes, the mitochondria reduce oxygen into water molecules, which induces alkalinisation of the inner membrane and, in turn, creates a proton gradient in the transmembrane called the proton motive force (Δp). This comprises the pH gradient (ΔpH) and the electrical membrane potential (Ψ), resulting in a negative charge of −220 mV. For this reason, this positively charged moiety ideally accumulates in the matrix of the mitochondria.[69] The presence of oxygen in the mitochondria maximises the production of ROS, hence enhancing the effectiveness of PDT.

1.3.5. Low dark toxicity

Low dark toxicity refers to the ability of a PS (in this case) to be non-active/harmless prior to photoirradiation.[70] In a different investigation, Ahmed and colleagues found that adding glycosyl units to a quaternised mono-pyridyl-triphenyl-porphyrin derivative reduced the cytotoxicity of the compound when compared to cationic porphyrins lacking glycosyl moieties. Due to the incorporation of the sugar residues, these scientists suggested increasing targeting.[71] Pheophorbide A was reported to be cytotoxic when incubated with Jurkat cells by Paul and co-workers in Al-Omari.

Therefore, pheophorbide, human serum albumin, and pheophorbide compound cytotoxicity was discovered.[72] Wieder *et al*. discovered dark toxicity when porphyrinoids were covalently attached to biomolecules. Furthermore, they noted that dark toxicity was observed when these PS compounds were present over a specific concentration.[73] This phenomenon has been observed in most PDT-mediated cancer therapies. Some researchers argue that this indicates that PS dyes can be toxic for use in biological processes, claiming that there are other contributors to cell death apart from the known $^1O_2$ or ROS production.[74]

These arguments lead to the study of other factors that might contribute to phototoxicity. It was discovered that copper is over-expressed in cancer cells because it plays a huge role in the production of blood components, and there is a lot of vasculature.[75] In addition to this, it is reported that copper is a crucial cofactor in the synthesis of several enzymes involved in human physiological activities. For this reason, Gu *et al*. observed that fluorescence probes they used to monitor their *in vitro* and *in vivo* studies underwent fluorescence amplification or quenching upon interaction with copper. Be it as it may, lots of studies have indicated that porphyrinoids exhibit fluorescence enhancement when they react with copper (II) complexes.[76,77,78] Al-Omari and Al-Noaimi further cautioned that from a series of metal porphyrinoid complexes used during PDT, pyropheophorbide-a methyl ester (PPME) molecules had the highest affinity for copper and hence fluorescence enhancement, which resulted in elevated dark toxicity.[79]

1.3.6. Minimal long-term sensitisation

This means that the PS must completely and quickly clear out of the body after the therapeutic procedure.[80] As reported above, PDT selectively destroys cancerous tissue by using a PS (photosensitizing substance) and light in the presence of O_2.

Specialised optical equipment, such as optical fibres, are used to illuminate the sick tissue after the PS has been allowed to build in the tissue for a period that normally lasts between 3 to 96 h. When oxygen is present, the PS absorbs the light and creates $^1O_2$ and other ROS.[81] This type of ROS production damages cellular activities and essential structures, which ultimately leads to the complete obliteration of tumour tissue. However, if this process occurs for a prolonged period, effects include the infiltration of macrophages, leukocytes, and lymphocytes into PDT-treated tissue due to the immune system being activated and blocking the provision of oxygen to the tumour.[82] Photofrin is problematic in this regard because it was found that 24 h later, post-treatment with the PS was still localised in the adrenal gland, the urinary bladder, and the liver to a greater extent than the pancreas, kidney, and spleen. Furthermore, the higher molecular weight components of Photofrin were partially retained in the liver and spleen at 75 days after injection. It is postulated that elimination will likely occur through lymphatic drainage and return to the bloodstream *via* the thoracic duct.[83] The PS will be eliminated from the body. The liver excretes many PS dyes used in clinical settings into the bile, which travels to the gut and is eliminated through faeces. The time it takes to clear out of the body relies on but is not limited to its molecular weight, internal metabolic interactions, membrane penetration and passage and its binding affinity to the target area, so the excretion of PS will be different due to their modifications.[83,84]

1.3.7. Light source

The role of light is very crucial for the activation of the PS. The wavelength of light used for photoactivation must be safe for host cells in order for it to produce ROS effectively. It was previously mentioned that for deep penetration to happen during

PDT, the PS has to absorb light in the therapeutic window, and there are a plethora of light sources used for PDT, including the following:[85,86,87,88]

1.3.8. Lasers[89,90,91]

Light Amplification by Stimulated Emission of Radiation, or laser, is the most frequently mentioned light source for PDT. Lasers produce highly radiant monochromatic, coherent, and collimated light. For PDT, there are a number of popular laser options, including argon ion lasers, metal vapour-pumped dye lasers, Nd: YAG lasers, and diode lasers. They both have the advantage of delivering high irradiance ranging from hundreds of mW cm^{-2} to several W cm^{-2}. Their irradiances are greater than those of other light sources, yet they only cover a narrow region. They can specifically target the main absorption peak of the photosensitiser due to their limited emission bandwidth. The use of dye lasers, which use organic dye molecules as the gain medium to enable a wide range of wavelengths to be created to match the absorption of various photosensitisers, is sometimes necessary due to the restricted number of wavelengths that are currently available.

1.3.9. Lamps[90-92,93,94]

Since the "Finsen lamp" was initially employed to treat lupus vulgaris in the late nineteenth century, lamps have played a significant role in light therapy. Nowadays, tungsten filament, Xenon arc, metal halide, sodium, and fluorescent lamps are among the lights used for APDT. Lamps emit light irradiance from a few to hundreds of mW cm^{-2} and are typically less expensive and easier to handle than lasers. Contrary to lasers, fluorescent and sodium lamps can be used to treat broad areas without connecting to fibres. Moreover, a wide range of wavelengths is emitted from the broadband lamps, covering the entire visible spectrum and allowing for absorption by most of the regularly used photosensitisers. However, unfavourable consequences,

including tissue deterioration from UV light and heat generated by infrared light, might be problematic. Due to this, spectral filters are typically used to block wavelengths that do not coincide with the main absorption band of the photosensitiser.

1.3.10. Light-emitting diodes (LEDs)[95,96,97]

Common light sources like LEDs work by applying a voltage to a semiconductor, which causes charges to be injected and light to be released. The semiconductor can be organic or inorganic (like GaAs or GaN). However, in actual use, organic LEDs are referred to as OLEDs, while the term LED is generally reserved for those based on inorganic semiconductors. LEDs are widely utilised in lighting and displays and as light sources for medical procedures. InGaN, AlGaInP, AlGaAs, and GaP are common materials for LEDs. Depending on the material, the emission wavelength can range from the ultraviolet to the infrared portions of the spectrum depending upon the band gap of the semiconductor. When compared to other light sources, many LEDs, particularly those that emit visible and near-infrared light, are inexpensive and capable of producing high irradiances of up to hundreds of mW cm^{-2}. LEDs are neither coherent nor monochromatic, like lamps, although their emission spectrum is significantly smaller—typically 20–40 nm wide. Since most photosensitisers are covered by the emission wavelengths of LEDs, LEDs can be chosen to match the main absorption band of a photosensitiser so they can be used without a filter.

1.3.11. Daylight[98,99,100]

In recent years, PDT using daylight has been pushed as an alternative to artificial light sources. It has a wide spectral range from the UV to the IR region, meaning that a wide variety of photosensitisers can be used. It has a few appealing qualities, including being cost-free, accessible without going to a clinic, and able to uniformly illuminate a sizable area. These characteristics indicate that scalp actinic keratosis has been

successfully treated with daylight PDT. Radiant exposure is, however, poorly managed during daylight PDT because sunlight has a wide range of irradiance.

1.4 Experimental factors

As reported above, a variety of light sources can be used in PDT, but for each case, there ought to be some consideration of the type of light source used. Below are detailed factors to consider.

a) Spectrum of the light source, or wavelength, if a laser is involved:

The amount of light absorbed depends heavily on its overlap with the photosensitiser. When it comes to lasers, the precise wavelength is displayed; however, investigations employing other light sources typically involve ranges of wavelengths.[101]

b) Area illuminated and distance between the light source and sample:

These parameters are useful in comprehending the experimental design, particularly the possibility of heat transmission from the source to the sample.[102]

c) Fractionation:

In some circumstances, turning the light source on and off is used to deliver the radiant exposure of light. The specifics should be given if this is done.[103]

d) Irradiation time and temperature:

It is important to note the experimental conditions to make the data reproducible.[104]

e) Irradiance (mostly mW cm^{-2}):

Enables the estimation of radiant exposure if the exposure time is known.[105]

f) Radiant exposure (J cm^{-2}):

The quantity of radiant energy falling on or radiated from a surface over a specific amount of time divided by the surface area.[106]

g) The initial amount of the photoinactivation target (cells, CFU or PFU):

The quantity/amount of target cells used substantially affects the outcome of the PDT procedure.[107]

h) Photosensitiser concentration at the start of illumination:

While some articles mention the initial concentration, the working concentration of the PS used should be acquired.[108]

i) The solvent used for photosensitiser solutions:

Certain solvents, such as methanol and ethanol, may be hazardous to the pathogen itself, necessitating special precautions when using them.[109]

j) Appropriate control experiments:

Three control experiments are required for APDT. The most basic is a control sample kept in the same environmental conditions as the sample exposed to PDT but without light or photosensitisers. Moreover, a control experiment without light but with photosensitiser is required. Dark control is a common term for this. Due to the real or potential toxicity of the photosensitiser, even in the absence of light, the dark control is not the primary foundation for sample comparison or computations. The final control that needs to be carried out is a "light control," which involves illuminating the sample in the absence of the photosensitiser.[110]

1.5 PDT mechanism

The fundamental mechanism underlying PDT is the production of ROS/$^1O_2$ by photosensitisers in response to light stimulation. Cell death results from one too many hindered/altered metabolic processes. It is reported that the species responsible for apoptosis during PDT affect an array of organelles such as ribosomes, endoplasmic reticulum, cell membranes, lysosomes, proteins and mitochondria, to name the least **Figure 7**.[111]

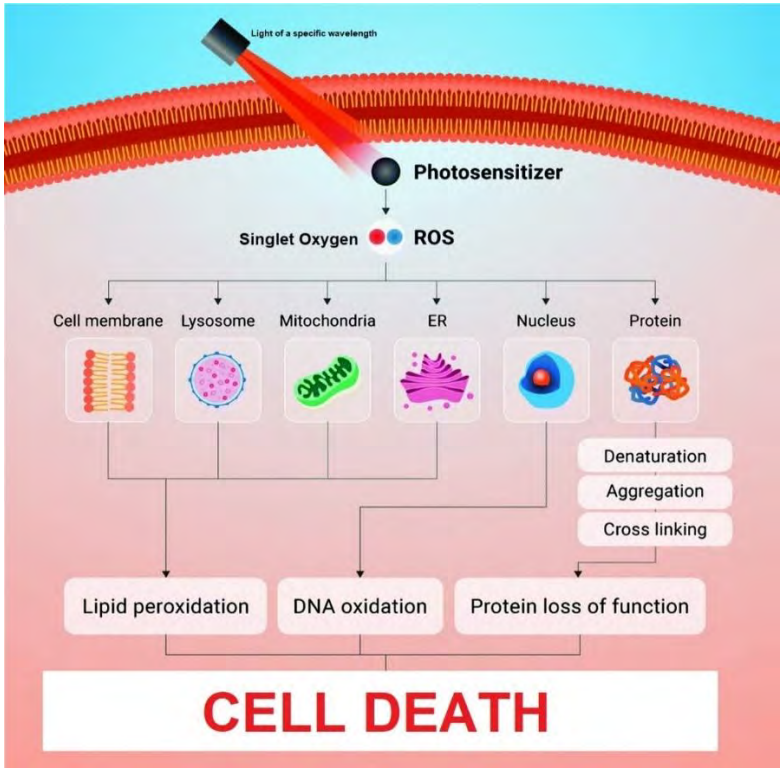

Figure 7: The different molecular organelles that are affected by PDT. Reproduced with permission from Ref. 195, © Royal Society of Chemistry 2021.

1.6 Strategies employed to increase the production of ROS/$^1O_2$

1) The use of PDT beacons where a second molecule is connected to the PS, suppressing the photodynamic activation until a chemical interaction with the

tumour occurs (e.g. enzymatic or pH cleavage of the linker or opening by hybridisation to a complementary oligonucleotide sequence).[112]

2) Altering the type of PS dyes used from traditional 2nd generation PS dyes by preparing photoactive nanostructures or their conjugates with 3rd generation PS dyes.[113]
3) Modification of the tissue microenvironment, specifically by enhancing oxygenation (usually in hypoxic environments).[114]
4) Versatile PS dyes that have been extensively utilised in PDT treatment include transition-metal complexes (the heavy atom effect) with long-lived T_1 states in order to enhance the rate of ISC, which will, in turn, afford enough time for ROS/$^1O_2$ production.[115]

1.7 The ISC working principles

i. Fluorescence resonance energy transfer (FRET):

FRET is accomplished through a long-distance dipole-dipole interaction based on donor-acceptor energy transfer. There are two main mechanisms for energy transfer: (1) resonance energy transfer (RET), also known as Förster resonance energy transfer (FRET), between the singlet states of the donor and acceptor; and (2) RET, also known as the Dexter electron transfer mechanism, between the triplet states of the donor and singlet states of the acceptor. FRET happens when: (1) D and A's spectra overlap; (2) D and A's proper distance, often less than 10 nm; and (3) the donor's relative quantum yield is high. Activatable photosensitisers can be evaluated easily because the FRET fluorescence quenching always correlates with $^1O_2$ quenching.[116]

ii. Photoinduced electron transfer (PET):

The effectiveness of ISC can be greatly increased by PET, which will increase the $^1O_2$ quantum yield. As a result, altering the PET process can influence the production of $^1O_2$. Furthermore, stimuli, including ions, polarity, pH, carbohydrates and phosphates, can control the PET process.[117]

iii. Intramolecular charge transfer (ICT):

$^1O_2$ production can be efficiently suppressed by ICT. The pH level and solvent polarity can result in the formation of a charge-transfer (CT) state of the donor and acceptor. ICT can also affect the fluorescence and singlet oxygen quantum yields.[118]

1.8 Cell death principles

Cell death induced by PDT/PACT can occur in different ways, but the three prominent ones are illustrated in **Figure 8** below:[119]

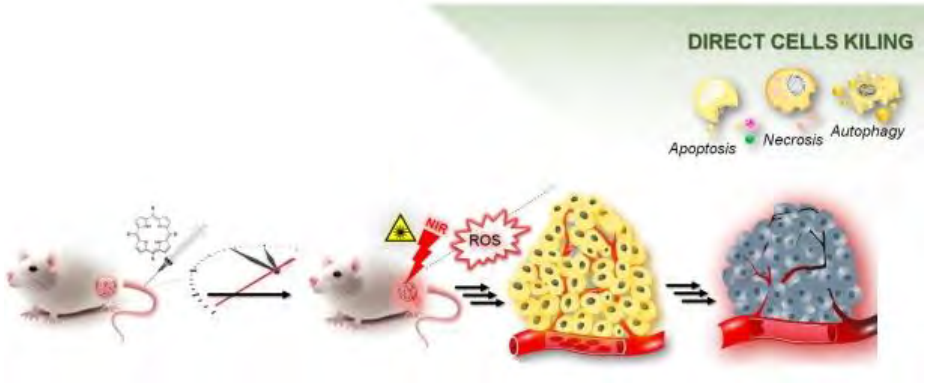

Figure 8: The three types of cell deaths that occur during photodynamic therapy action. Reproduced with permission from Ref. 119, © Elsevier 2020

1.8.1 Apoptosis:

Apoptosis is a genetically encoded multi-pathway cell-death program that exists in all cells. The death receptors can be activated, or cytochrome c can be released from the

mitochondria to start it. The activation of "executioner caspases", such as caspase-3, -6, and -7, is the result of both processes. Then, in order to cause the typical biochemical and morphological changes seen in dying cells, the active executioner caspases break cellular substrates. Chromatin condensation and nuclear shrinkage occur after the cleavage of nuclear lamins, while DNA fragmentation results from the cleavage of the inhibitor of DNase CAD (caspase-activated deoxyribonuclease). Lastly, apoptotic bodies are created when cytoskeletal proteins are cleaved, which causes cell fragmentation.[120]

1.8.2 Necrosis:

Necrosis is a fast and violent form of cell death that affects substantial portions of the cell population. Necrosis is characterised by cytoplasmic enlargement, organelle destruction, and plasma membrane disruption, which leads to the release of intracellular contents, causing inflammation. It is also known as unintentional cell death and is thought to be an *ad hoc* process brought on by physical or chemical injury. Its defining features are a pyknotic nucleus, cytoplasmic enlargement, and gradual cytoplasmic membrane disintegration. These features all cause cellular fragmentation and material discharge into the extracellular compartment. Proteolytic activity is primarily responsible for mediating decomposition in necrosis, although the specific identities of the proteases and the substrates they operate on are little understood. It is highly agreed upon that low doses of PDT tend to predispose cells to apoptotic cell death, but high doses of PDT (either a high photosensitiser concentration or a high light fluence or both) tend to cause necrosis.[121]

1.8.3 Autophagy:

A catabolic cellular process known as autophagy enables the cell to balance the creation, breakdown, and recycling of cellular products. There are numerous autophagic processes, all of which rely on the lysosomal breakdown of cellular proteins and organelles. The most widely recognised mechanism works as follows: The target region is encircled by an autophagosome, a double-membrane structure that isolates its contents from the surrounding cytoplasm and forms a vesicle. The autophagolysosome is formed when this vesicle is transferred and fused to the lysosome. Its contents are then broken down by lysosomal hydrolases. Under times of hunger or stress, autophagy not only makes it easier to eliminate undesirable proteins, organelles, and microbes but also enables a cell to redistribute nutrients from unneeded to vital functions.[122]

Deducing from the review above regarding the most versatile and effective PS, type of light source and the type of cells being treated for either PDT or PACT. The initial aim of this project is, therefore, to utilise bacteriochlorins conjugated to nanoparticles for PDT and PACT applications.

1.10 The preferred PS dyes for this work

The ultimate set of target compounds in this study are bacteriochlorins (BChls), which are porphyrin analogues. Porphyrinoids are organic molecules with heteroaromatic tetrapyrrole macrocycles. The parent porphyrin ligand has a 22-π electron system with no more than 18-π electrons incorporated into any one conjugative path (delocalisation system). Porphyrinoids are chromophores that can be obtained from natural pigments such as bacteriochlorophyll, chlorophyll, and the heme group.[123] Phthalocyanines, texaphyrins, sapphyrins, porphycene, porphyrins, chlorins

(dihydroporphyrins) and bacteriochlorins (tetrahydroporphyrins), as depicted by **Figure 4**, are some examples of porphyrinoids that are suitable for PDT applications. In porphyrinoid complexes, the macrocyclic core is substantially conjugated and is reported to have effective resonance. Moreover, they are reported to follow Huckel's 4n+2 rule (with n = 4) of aromaticity because they are cyclic and planar.[124,125]

Bacteriochlorins (BChls) were chosen as the main target PS dye because, unlike their counterparts, porphyrins and chlorins, they absorb light near the infrared region (NIR) well within the therapeutic window. This enhances tissue penetration when excited by a complimentary light source, **Figure 9**. NIR photons can give direct access to biological targets because they are the most invasive and least harmful to human tissues. A phototherapeutic window is the region of spectra between 650 and 850 nm, where light can penetrate tissue up to 1−3 cm.[125,126]

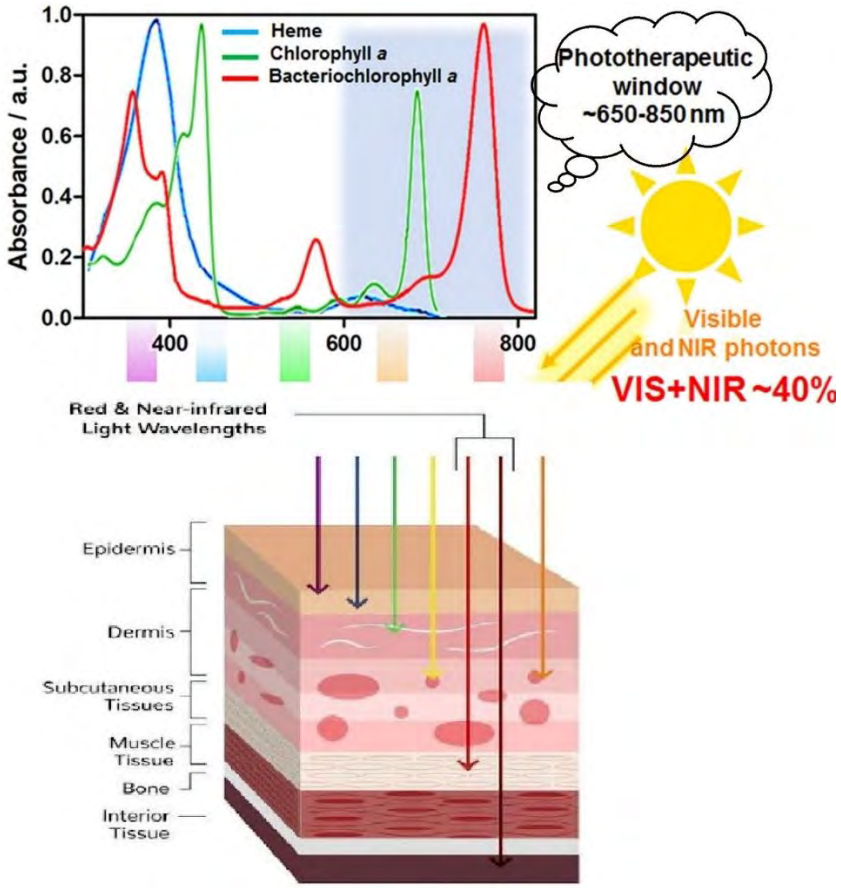

Figure 9: The electronic absorption spectra of heme, chlorophyll a and bacteriochlorophyll a. Tissue penetration of different portions of the visible region and NIR. Reproduced with permission from Ref. 119, © Elsevier 2020.

Another favourable feature of BChls is that, along with all the other types of porphyrinoids, BChls have distinctive three-band absorption spectra, comprising an intense B (or Soret) band and two spectrally distinct Q bands, Q_x and Q_y, with the longer wavelength absorption band Q_y band (also known as the "max band") lying considerably above 700 nm. Furthermore, they are structurally similar to porphyrins and chlorins. In contrast to porphyrins, which contain a complete tetrapyrrolic system, chlorins only have one reduced pyrrole, while bacteriochlorins have two reduced pyrroles on the other side of the macrocycle. Although the differences between these macrocycles appear to be negligible, their spectroscopic, photophysical, and redox characteristics are very different.[127] A chlorin is created by reducing one of the

peripheral pyrrole bonds of a porphyrin. As a result, the symmetry is lowered. Further reduction of another opposite peripheral bond results in a BChl with a split Soret band and a Q band in the 720−800 nm region.[128] According to Gouterman's 4-orbital theory that a fully unsaturated porphyrin has a D_{4h} symmetry and has a degeneracy of its two lowest unoccupied molecular orbitals (LUMOs) along with its highest occupied molecular orbitals (HOMOs). It is reported that transitions from these orbitals have/require the same amount of energy and that configurational interactions remove the default degeneracy, and as a result, the Soret and Q bands form.[129]

During the reduction of porphyrins to form Chls and BChls, **Figure 10** shows that two of the four frontier MOs are unaffected, whereas the other two are destabilised. This is because there are large Molecular orbital (MO) coefficients on the reduced bond, while the opposite is true for the other unaffected orbitals. This property can be exploited in the design of PS dyes that absorb at the NIR. This can be done by attaching electron-donating or -withdrawing functional groups at specific locations on the porphyrin structure to modify the energies of the frontier π-MOs, thereby shifting the main absorption bands.[130] Added to this, the change in the molecular structure causes a broadening of the pairs of transitions associated with the Soret and Q bands, increasing the oscillator strength of the Q bands.[119]

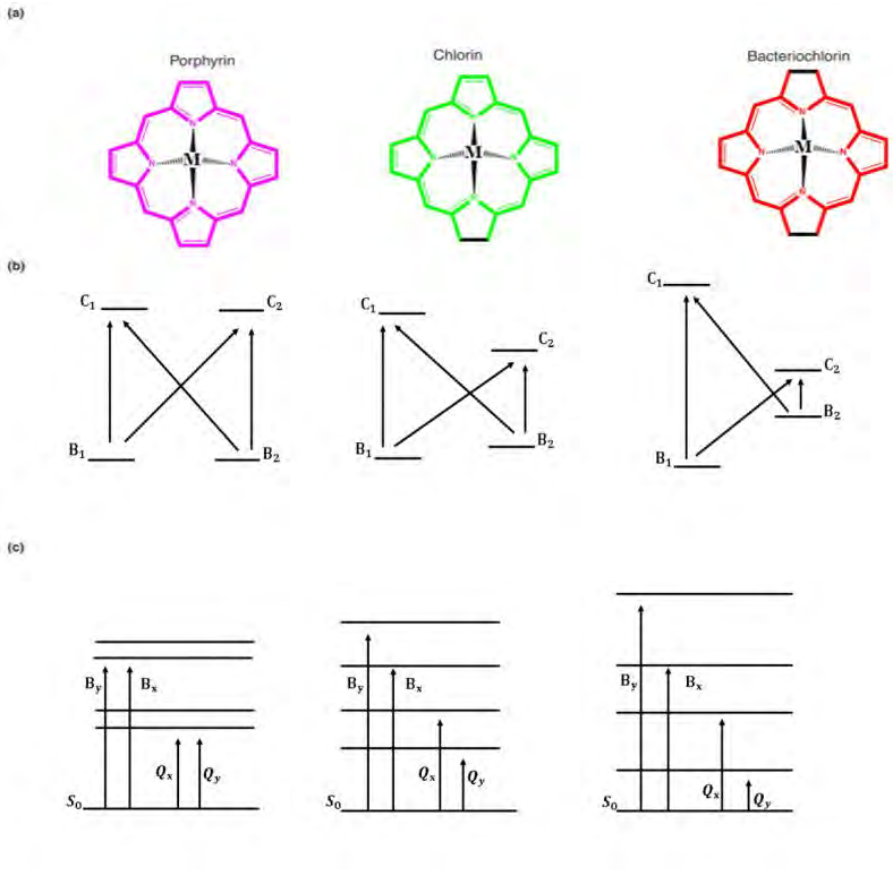

Figure 10: The effects of the reduction of a metal porphyrin to form chlorin and bacteriochlorin complexes, respectively. (a) The molecular structures of the metal porphyrin, chlorin and bacteriochlorin complexes, (b) the changes in the relative energies.

Over the years, BChls have been under heavy scrutiny and criticism due to their instability. The reason for this is that BChls are prone to dehydrogenation, thereby leading to the formation of chlorins, which are relatively stable. Another discouraging factor is due to the molecular rigidity of BChls. It has proven to be difficult to extract reasonable quantities from their natural sources, so synthetic dyes are likely to be the best way to develop new BChl PS dyes.[132] There are a couple of strategies to remedy these limitations, with the first one being the substitution of the peripheral carbons with poor leaving groups to inhibit dehydrogenation.

As reported above, this not only leads to significant changes in the optical properties like the change of symmetry from D_{2h} to D_{4h}, followed by the degeneration of the LUMO

orbitals as well as a drop from four to two Q bands in the electronic absorption spectra and lastly a batho- or hypsochromic (red or blue) shift of the Soret band is observed and of most importance is the increase in the molar extinction coefficient which indicates how far radiation of a specific wavelength can penetrate a substance before being absorbed (the higher the coefficient, the deeper the penetration).[133]

Another factor to consider is the solubility of the BChls. As indicated earlier, the mode of administration of PDT is intravenous injection, so it is of the utmost importance that the BChl is soluble in aqueous media. WST11, padeliporfin, or TOOKAD®Soluble) a BChl PS dye with a negative charge proved to be soluble in PDT applications. It was determined that the presence of negatively charged -SO_3H groups provides WST11 with its hydrophilic properties.[134] In contrast, recent studies have reported that porphyrinoid PS dyes can be quaternised to induce a cationic charge that enhances aqueous solubility and the permeability of the PS in lipid biomembranes. This was postulated to have been because the cellular surfaces are normally negatively charged, so a positively charged PS dye will have higher permeability relative to anionic or neutral PS dyes.[135] Moreover, and advantageously, it has been reported that cationic porphyrinoids have high affinities towards proteins such as bovine serum albumin (BSA) and human serum albumin (HSA).[136]

The introduction of halogens like fluorine and chlorine in the *ortho*-position, on the other hand, is reported to destabilise BChls by causing polarity, which plays a role in accelerating the movement of physiologically active substances (in this case, BChls) through lipid membranes.[137] In contrast, the attachments in the *meta*-position promote hydrophilicity and hence solubility. Additionally, introducing a positive charge on the BChls (cationic BChls) is reported to be the most effective solubilizing factor.[138]

Nanoparticles, micelles and liposomes are reported to aid the solubility of BChls by introducing charges that induce hydrophilicity, encapsulating the BChls and transporting them to their designated locations without the complications of insolubility.[139] Lipophilicity describes the ability of BChls and other molecular dyes to interact with or penetrate the lipid bilayer of an array of cells. The first option is to introduce branched alkyl chains (swallowtail) to mimic the phospholipids around the cell membrane, thereby helping the BChl interact with the membrane.[140] These chains are also thought to enhance the solubility of BChls. Aggregation is the last factor considered in the design of the BChls that are used in this study. Aggregation is said to be brought about by the π-π stacking of the orbital bonds of the chromophore molecules. A broadening of the Soret and Q bands is observed when this occurs.[141] To solve this problem, bulky moieties are attached to the BChl molecule to afford steric hindrance, which also hinders π-π stacking.

Mack and coworkers stated that certain metalated porphyrinoids undergo H- and J-aggregation because of hydrophobic π-π stacking interactions.[142] Aggregation through exciton coupling modifies the porphyrins' electrical structure, which has a detrimental effect on the effectiveness of PDT. Another method used to reduce aggregation is the insertion of axial ligands bound to metallic centres such as tin (Sn^{4+}) or phosphorus (P^{5+}). They also demonstrated that introducing *trans*-axial ligands hinders aggregation, and the presence of the heavy central metal ion efficiently increases the population of the T_1 state. In another study, they inserted bulky *trans*-axial 2-naphtholate ligands, which also increased the solubility of the PS and prevented aggregation.[143]

The tailoring of PS dyes to actively target certain organelles that play a significant role in PDT. A variety of these organelles are specifically targeted, such as the cell membrane, nucleus, lysosome, endoplasmic reticulum and mitochondria.[144,145]

1.11 PDT target organelles

a) The nucleus

The nucleus is the control centre of every cell and consists of genetic material such as chromosomes and nucleolus. Targeted sites include DNA, RNA, mRNA, nucleus-specific ribosomes, and a range of proteins found in the nucleus only.[146]

b) The endoplasmic reticulum (ER)

The endoplasmic reticulum controls both the movement of materials and the biological synthesis of macromolecular substances. It is mainly composed of ribosomes, which are responsible for the production of most amino acids, which, in this case, can be targeted.[147]

c) Lysosomes

Lysosomes are responsible for the degradation and recycling of cell components. They are reported to have approximately 50 digestive enzymes, which contribute to the degradation of sugars, lipids, DNA and RNA. Most of these enzymes are acid hydrolases with a pH in the 4−5 range, since hydrogen peroxide plays an important role in the degradation processes, creating byproducts such as hydroxyl radicals and $^1O_2$, hence contributing to effective PDT.[148]

d) Mitochondria

Mitochondria are primarily responsible for the generation of energy through oxidative phosphorylation. In addition, it oversees control of the cell's metabolic activities.

Moreover, they encourage cell division and expansion and are critical for apoptosis or programmed cell death.[149] Mitochondria have not been studied extensively when it comes to PDT targeting. Recently, in a study conducted by Mack and coworkers whereby they attached a bulky cationic triphenylphosphonium (TPP^+) moiety on the *meso*-position of their PS of choice to target the mitochondria, this organelle was preferred because by default, as indicated above, it regulates apoptosis and that even though its matrix is reported to having low concentrations of oxygen (referred to as being hypoxic).[150] The efficacy of PDT is reduced in hypoxic conditions. Due to the availability of oxygen species in the transmembrane, it is reported that alkalisation takes place to form water molecules, thus making this a good site for ROS and $^1O_2$ generation. Furthermore, due to the regulation of apoptosis, the mitochondria have an extremely negative membrane potential ($\Delta\Psi_m$), approximated to be *ca.* −220 mV. The TPP^+ moiety is ideal to use in this context because it will accumulate to the negatively charged mitochondria, so mitochondria targeting was chosen as a structural modification strategy for this project.[151]

e) Nanoparticles (NPs)

Nanoparticles have size ranges on the nanometre scale.[152] Their discovery dates back to the 1940s, with Hoar and Schulman reporting what they termed “a dispersion system” (**Figure 11**). A considerable amount of research led to the development of gold nanoparticles around the 1960s. NPs are used widely in medical applications, solar energy and diagnostic procedures, to name a few. In a medical context, they are used extensively in cancer therapy for both detection and eradication. This is often termed theranostic.[153,154] Apart from modifying the PS of choice to target the cancerous tumours, nanoparticles can also transport the PS to the target site.

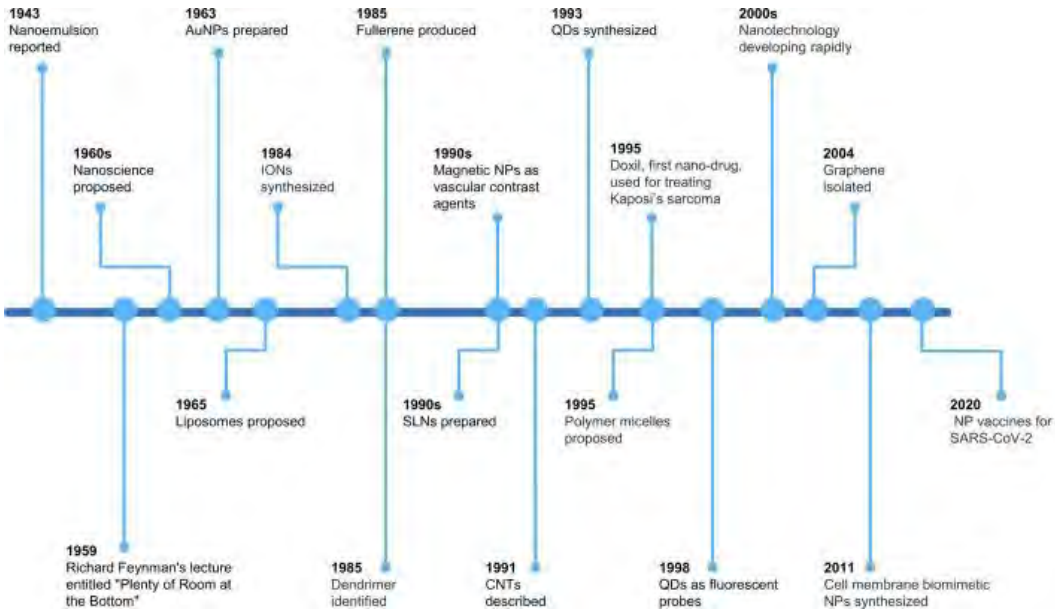

Figure 11: The history of the discovery of NPs to date. Reproduced with permission from Ref. 153, © Nature Portfolio 2022.

NPs are preferred because they possess favourable chemical properties. These include thermal stability, high surface area, biocompatibility, optical and plasmon characteristics, low toxicity, controlled drug release, and catalytic activity.[155] They are also easy to functionalise. NPs are grouped into the following categories.

1) Inorganic: These include quantum dots, metallic, ionic and mesoporous NPs.[156]
2) Lipid-based: Liposomes, solid lipids and NPs.[157]
3) Polymeric: Polymersome, micelle and dendrimer NPs.[158]
4) Carbon-based: Carbon quantum dots, fullerenes, carbon nanotubes and graphenes.[159]

Although the formation of gold nanoparticles is topical and tends to be preferred in the medical field, carbon dots (CDs), which were more recently discovered, show promising potential. CDs are said to have size ranges < 10 nm.[160] This is considered advantageous in PDT because the smaller the NPs, the more effective the enhanced

permeability retention effect (EPR effect). The EPR effect refers to the tendency of NPs or macromolecular drugs to accumulate more in tumours than in healthy tissues.[161] The greater pore size of neo-vasculatures and the poor lymphatic clearance of tumours are the main causes of the EPR effect, which is also greatly influenced by the size of tiny molecules, including nanoparticles. The EPR effect facilitates passive targeting as well.[162] CDs have a quasi-spherical shape. Not only are they biocompatible, highly stable, and exhibit efficient light harvesting, but most importantly, they are reported to facilitate photoinduced electron transfer. This makes them ideal candidates for PDT applications.[163] It is for this reason that CDs were selected for *in vitro* PDT and PACT studies in this study.

1.12 Photodynamic antimicrobial chemotherapy

Having discussed the factors affecting PDT in-depth, it is important to also introduce the connected field of photodynamic antimicrobial chemotherapy (PACT). PACT also makes use of $^1O_2$ and reactive oxygen species (ROS) to eradicate bacteria, fungi and viruses.[164] In this study, we will specifically focus on multi-drug-resistant bacteria. Bacteria have always been problematic for human health. Some of their well-known detrimental effects date back to 2650−2600 BC when Egyptian physicians used mouldy bread to treat infected wounds. Typically, a fungus causes mould formation. Penicillium, aspergillus and rhizopus are examples of common mould fungi that hinder or alter the growth of bacteria. The Egyptians were aware of this factor and exploited it to treat cuts and wounds.[165]

It was not until 1928 that Alexander Fleming, a Scottish bacteriologist, formally discovered that penicillin was the compound that caused the death of bacteria in the mould.[166] This marked the beginning of the antibiotic era. Human health issues

historically caused by bacteria include the Plague of Athens. The Peloponnesian war was affected by *Salmonella enterica serovar Typhi*, which also causes typhoid fever. This bacterium was responsible for the deaths of *ca.* 25% of the Athenian soldiers engaged in combat and also affected both the troops returning to Athens and the citizens living in the city itself.[167] Bubonic plague, on the other hand, ravaged *ca.* 50% of the European population. *Yersinia pestis* has been reported to be the bacteria that also caused the Black Death, which was reported to have originated in China and spread through Europe carried by rat fleas. It was reported to have taken the lives of *ca.* 100 million people.[168]

The 20th century sparked the development of antibiotics to combat bacteria. **Figure 12** below depicts the timeline of clinically used antibiotics.

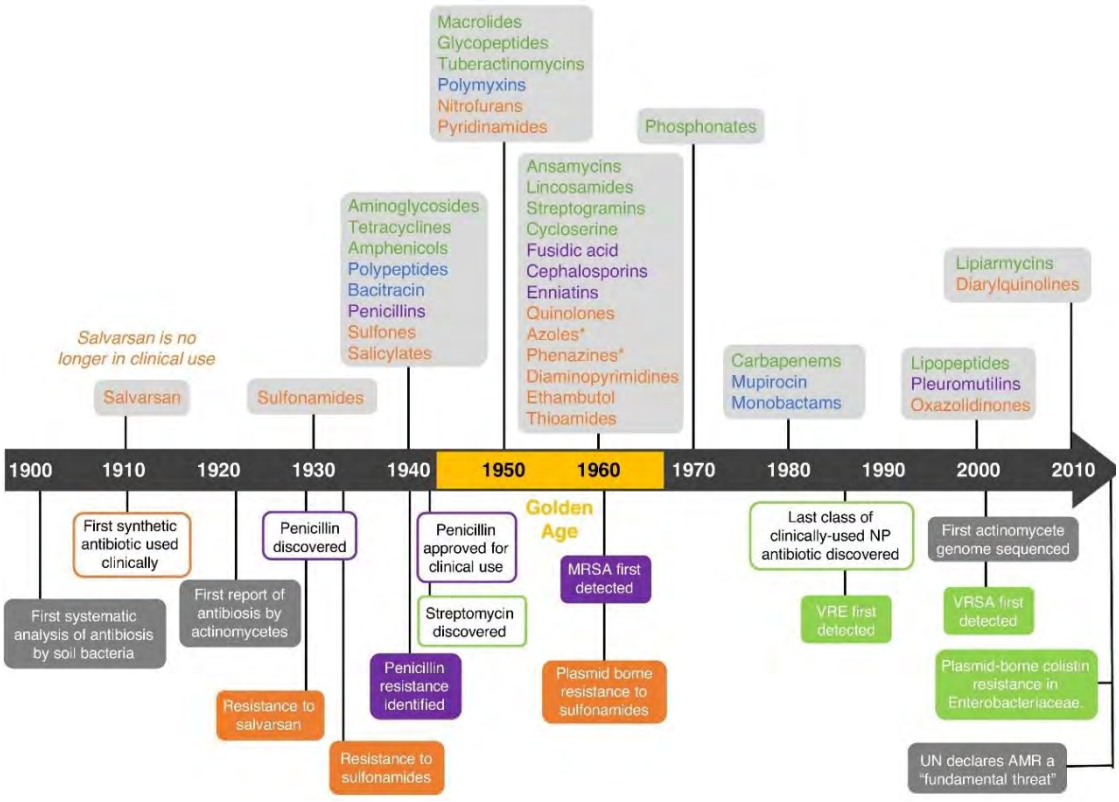

Figure 12: The timeline of the development of antibiotics until the 21st century. Reproduced with permission from Ref. 196, © Elsevier 2019.

The development of antibiotics proved to be crucial for human health. However, as bacteria evolved, some strains developed ways to elude them. This resistance became prevalent due to bacterial replication. As observed in the figure above, in the 1960s, cases of *Methicillin-resistant Staphylococcus aureus* (MRSA), a family of Gram-(+) bacteria, were recorded. Then, around the 2000s, the resistance of Enterobacteriaceae organisms, Gram-(−) bacteria including *Enterobacter, Klebsiella, Citrobacter, Salmonella and Escherichia coli*, was reported. This led to the United Nations highlighting antimicrobial resistance as a fundamental global threat.[169]

As indicated above, Gram-(+) bacteria were the first to develop resistance against antimicrobial resistance. The Gram-(+) terminology refers to bacteria with a thick cell wall due to the thick peptidoglycan layer, which is between 30−100 nm in diameter (**Figure 13**).[170] This layer is embedded with lipoteichoic and teichoic acid. Underneath it is the cell membrane with membrane proteins. In contrast, the Gram-(−) cell wall consists of lipopolysaccharides and membrane proteins on the outer membrane layer, followed by the peptidoglycan layer, which is between 1.5−10 nm in diameter. Directly below it is the periplasmic space. Then, lastly, there is the cell membrane with embedded membrane proteins.[171]

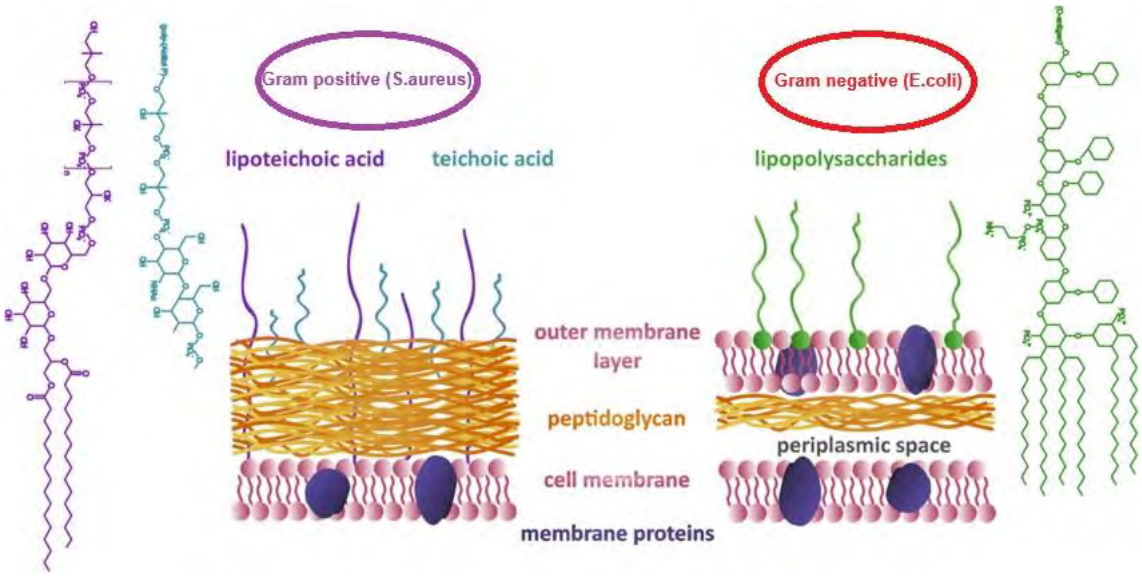

Figure 13: The difference between a Gram-(+) and Gram-(−) bacteria cell wall. Reproduced with permission from Ref. 197, © Springer 2019.

Around the 1900s, Oskar Raab and Hermann von Tappeiner discovered that the staining of protozoa by acridine, followed by the irradiation of bright light, resulted in their death. This marked the beginning of PACT.[171] Using PACT to tackle AMR bacteria like *Staphylococcus aureus* (*S. aureus*) and *Escherichia coli* (*E. coli*) is reported to be more effective because of the immediate obliteration of the microbes. Furthermore, what is more advantageous is that the microbes are unlikely to develop resistance towards $^1O_2$ and other ROS.[41] Therefore, studying the efficacy of PACT on these two microbes will also be explored in this project.

1.13 Synthesis of Porphyrins and Bacteriochlorins

1.13.1 Porphyrinoid structures

It is important to outline the nomenclature and synthesis of porphyrins before focusing on the synthetic routes of BChls. **Figure 14** below illustrates the standard porphyrinoid nomenclature.

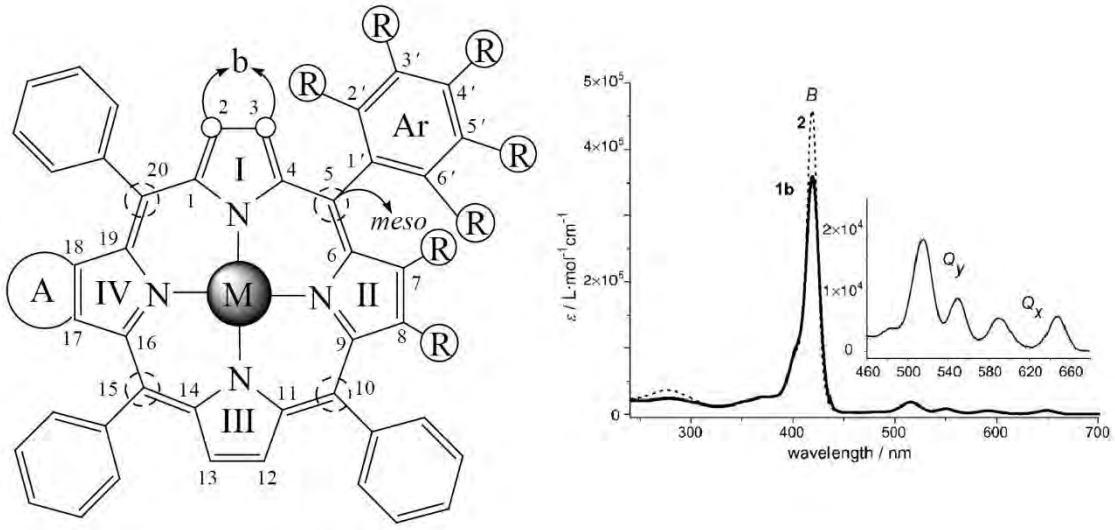

Figure 14: The generic structure of a functionalised porphyrin showing the nomenclature alone with the standard Fischer numbering system. A typical UV-visible absorption spectrum is provided as an insight. Reproduced with permission from Ref. 171, © Springer 2022.

I-IV denotes the four pyrrolic rings that make up a porphyrin, M is any metal substituent in the core of the molecule, b is the beta position on the ring, *meso* is another designated region of the ring, AR denotes a meta aryl substituent, R is any functional group attached to the aryl substituent. The absorbance spectrum on the right depicts a typical porphyrin with a Soret/B-band in the 400−440 nm region and the four Q bands (Q_y and Q_x).[174]

1.13.2 Porphyrinoid history

The strategies of porphyrinoid synthesis have drastically evolved over the decades. The first attempt was by Rothemund and colleagues in 1935 (**Scheme 1**).[175] A one-pot thermal condensation involves the reaction of choice aldehydes and pyrrole to produce porphines or isoporphines.

Scheme 1: Rothemund's condensation reaction of porphyrins.

Different yields can be obtained under various situations depending on the reaction parameters for this condensation. The inclusion of heterocyclic bases, such as 2,4,6-collidine or metal ion species like Cu(I) and Co (II) can result in higher yields of the porphyrin target products. The substituent on the aldehyde determines how the reaction proceeds, with an electron-deficient aldehyde often yielding a higher yield of porphyrin than an electron-rich aldehyde. However, the reaction has many limitations, such as very low yields, harsh reaction conditions resulting in low conversion or degradation of the starting material, and it is challenging to separate pure porphyrin due to the creation of additional porphyrin analogues, including chlorins, sapphyrins, isosmaragdyrins, ozaphyrins, hexaphyrins, and corroles. The other major disadvantage is the requirement of large quantities of harsh oxidants such as DDQ

with prolonged reaction at high temperature. This led to the development of other relatively safer reaction routes.[176]

In 1965, Adler and colleagues modified Rothemund's reaction to make it "greener" by reducing the hefty usage of harsh reagents (**Scheme 2**).[177] The one-pot acid catalysis reaction employed an aldehyde and pyrrole reflux for about 30 min at 140 °C. This mild route provided an enhanced yield of 20%. The omission of extremely harsh reagents significantly increases the yield, and minimal porphyrin analogue side products are produced.

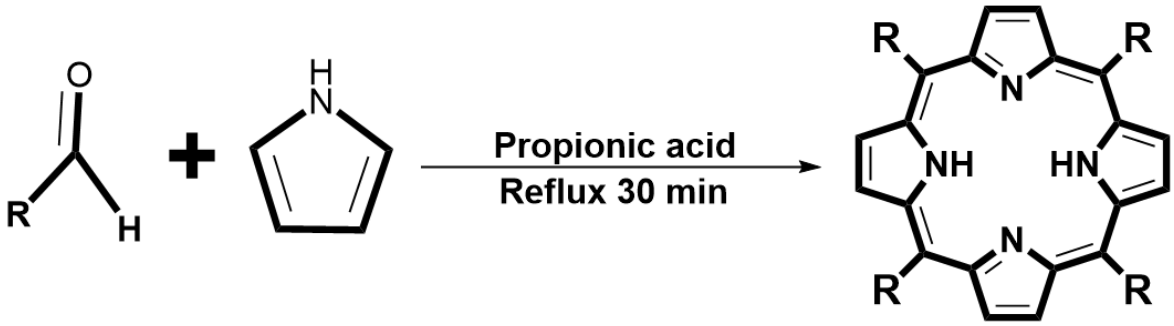

Scheme 2: Adler-Longo porphyrin synthetic route.

Although this reaction was considered to be mild and fast, there are some limitations to be noted as well. Firstly, propionic acid can degrade acid-sensitive aldehydes and render the reaction null or lower the yield. Secondly, purification problems are encountered because of the tar byproduct, which interferes with the separation process. Lastly, it is widely reported that this methodology has low batch reproducibility because it is highly sensitive to various conditions.[178]

Synthetic route modifications continued throughout the early to mid-1980s by researchers such as Someikin and colleagues (1983) and Gonsalves and colleagues (1985), as indicated below by the timeline in **Figure 15**. Then, in 1986, Lindsey and

coworkers introduced a more user-friendly porphyrin and readily upscaled synthetic route, which facilitated the use of sensitive aldehydes and resulted in fewer byproducts.[173] The Lindsey method is adapted from the Adler-Longo mentioned above, **Schemes 2** and **3**.

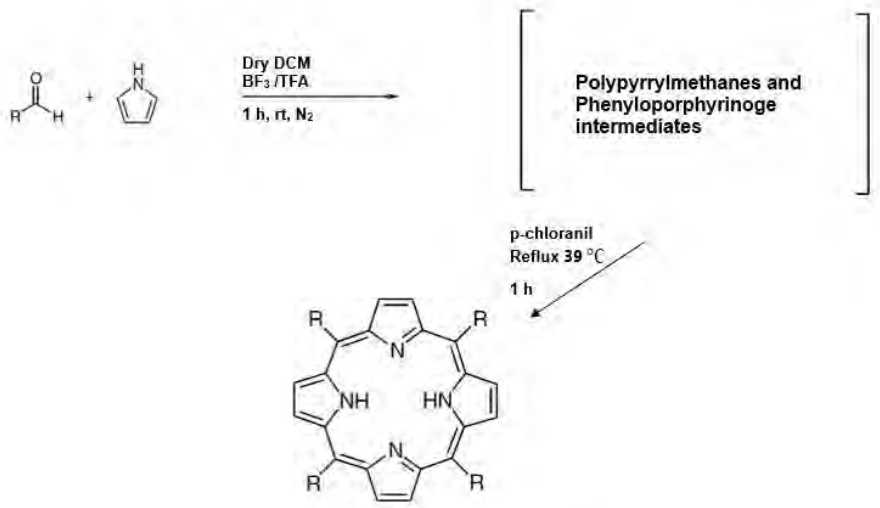

Scheme 3: The Lindsey synthesis route.

In a similar manner to the earlier developed routes, a choice aldehyde is reacted with pyrrole in dried dichloromethane with an acid (either BF_3 or TFA) at room temperature under inert gas for an hour. This will lead to the formation of polypyrrylmethanes and then polypyrrylmethenes. An oxidant, *p*-chloranil, is added. Then, the reaction is refluxed for about an hour at 39 °C to obtain the desired porphyrin.[179]

Subsequently, too many synthetic routes have been developed to describe each one in detail, particularly given the continuing dominance of the Aldo-Longo and Lindsey methods, but the timeline below in **Figure 15** summarises the events well.

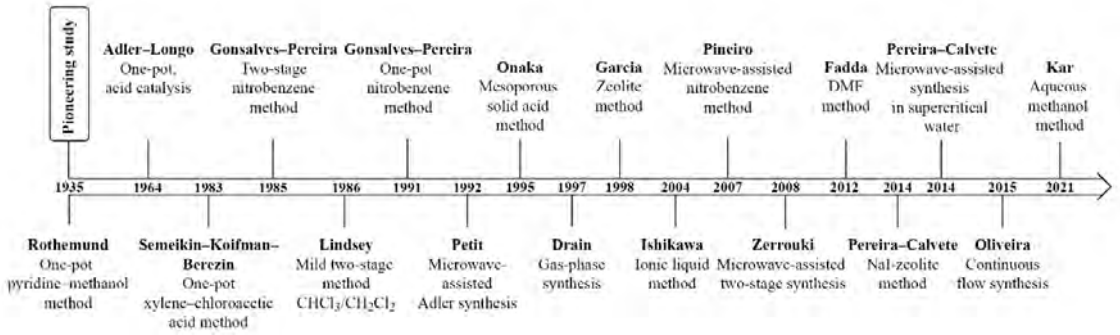

Figure 15: The evolution of porphyrin synthesis from 1935 to 2021. Reproduced with permission from Ref. 171, © Springer 2022.

Having explored the different synthetic routes for porphyrins, the next objective is to discuss the synthetic routes that are available for bacteriochlorins (**Figure 16**).

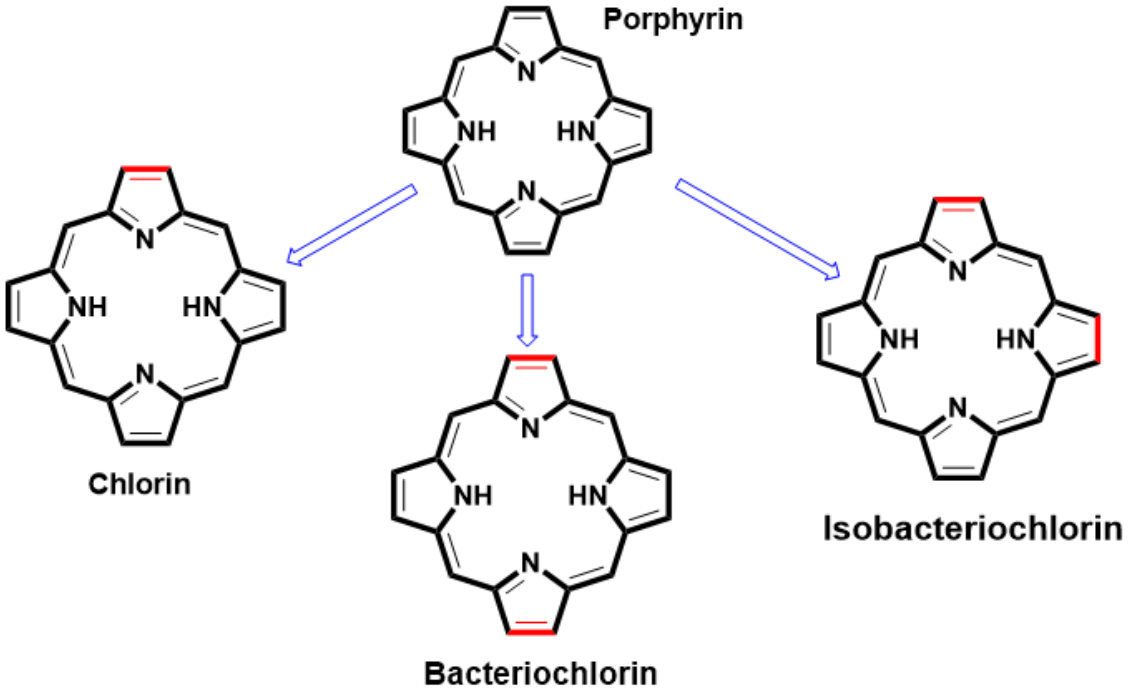

Figure 16: The structural differences between porphyrins (no reduction), chlorin (one reduced pyrrolic ring), isobacteriochlorin (two adjacent reduced pyrrole moieties), and bacteriochlorin (two oppositely aligned reduced pyrrole moieties).

As previously indicated, porphyrins are saturated tetrapyrrole macrocycles linked by methylene carbons. They have an 18 π-electron system cross-conjugated with β-β'

double bonds. These bonds can be reduced, leading to the formation of chlorins, BChls or their isomers, *iso*-BChls.[180] This reduction can be accomplished via an addition reaction, thereby causing the β-carbons to be sp^3 hybridised. Even though the π-system remains an 18 π-electron system after the reduction, some significant changes happen as a result. One noticeable difference is the large changes observed in the UV-visible absorption spectrum, **Figure 17**, including a large splitting of the Q bands and a red shift of the lower energy Q band. It has been reported that BChls are less basic than Chls and porphyrins.[181] An increase in flexibility of the conformation of the molecule results in decreased basicity of the inner imine nitrogens.

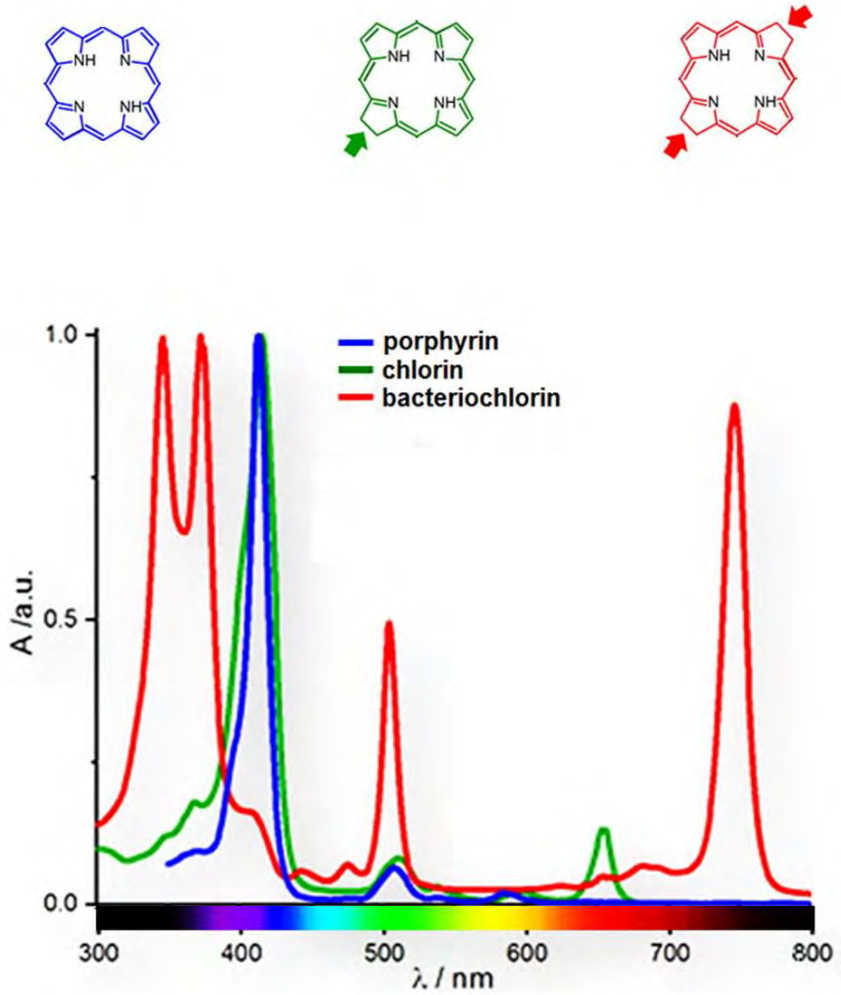

Figure 17: The UV-visible absorption spectral differences between porphyrins, Chls, and BChls. Reproduced with permission from Ref. 137, © Elsevier 2016.

BChls are found naturally in photosynthetic pigments, such as bacteriochlorophylls a (BChl a), b (BChl b), and g (BChl g). BChl a is the precursor of BChls. BChls can be synthesised in a variety of ways, such as:[119]

Semi-synthesis of BChls from natural products[183]

This process includes the isolation of BChls from natural sources, which are then modified (**Figure 18**). Over the years, there have been a lot of studies in this area that are too numerous to mention. The most common route is the extraction of chlorophyll-a and bacteriochlorophyll-a to form this chromophore. In a study conducted by Dukh *et al.,* they used the above-mentioned extracts and modified them to obtain ester-linked chlorin-bacteriochlorin dyads.

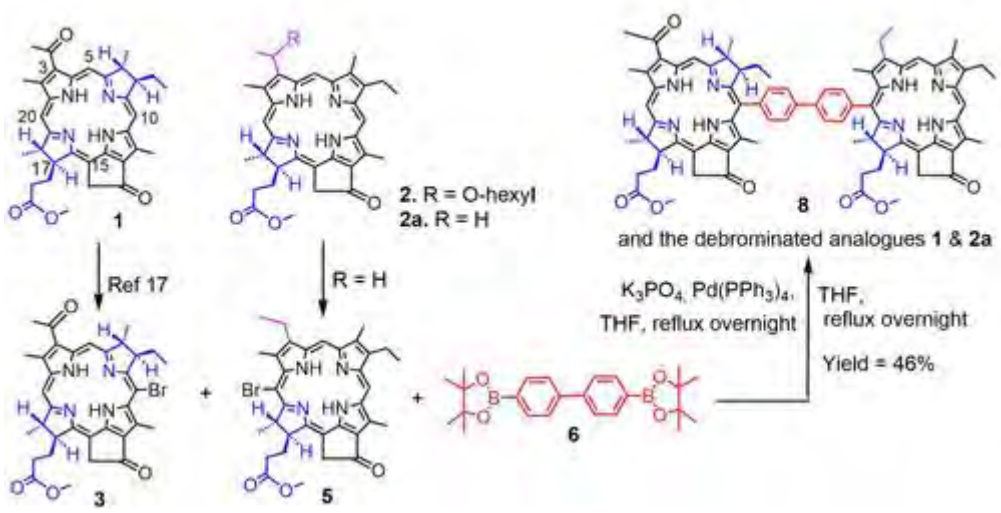

Figure 18: The semi-synthesis and modification of chlorophyll a and bacteriochlorophyll a to produce Chl and BChl, respectively. Reproduced with permission from Ref. 180, © John Wiley and Sons 2020.

The authors reported that the bacteriopyropheophorbide (indicated by **1** in **Figure18**) was extracted from *Rhodobacter sphaeroides*, a group of purple bacterium that are photosynthetic. When it was reacted with N-bromosuccinimide (NBS), its 10-bromo analogue (**3**) was formed. The Chls (**2** and **2a**), which were also extracted, were further

modified to be linked to the BChls. Apart from the complexity of this type of reaction, the large number of functional groups in these extracts makes the tailoring of the BChls tedious. Furthermore, factors such as chemo and regio-selectivity make their manipulation complex and drastically decrease the desired yield. This method is quite tedious and hence requires improvement.[183]

Total synthesis

Total synthesis refers to the complete chemical synthesis of a complex molecule, frequently a natural product, and, in this case, the synthesis of BChls from simple commercially available components. Lindsey and co-workers played a significant role in the development of BChls by pioneering effective synthetic routes (**Scheme 4**). These routes are mainly based on retrosynthetic mechanisms in which the target chlorin is synthesised by combining a dipyrromethene with a gem-dimethyldihydrodipyrrin. This is referred to as the [2+2] Chl and BChl approach. BChls, in particular, can be obtained by the fusion of two similar gem-dimethyldihydrodipyrrin molecules.[184] This is referred to as a head-to-tail fusion.

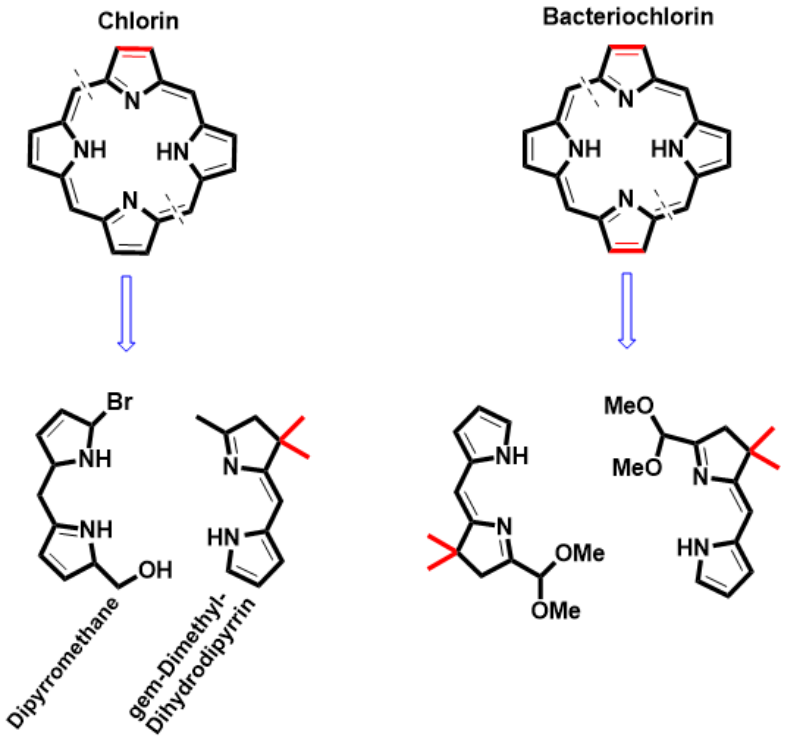

Scheme 4: The retrosynthetic route of Chl and BChl synthesis.

The cyclisation of the ring occurs via an acid-catalysed condensation of the two dihydrodipyrrin dimethyl acetals. These moieties are stirred at room temperature in a polar solvent with the addition of an acid as a catalyst. Lewis acids are said to be ideal for the synthesis of the BChls. This reaction route is said to produce few byproducts, thereby yielding a largely pure product. The main drawback of this method is the lengthy synthesis of the dihydrodipyrrin precursors, which requires about eleven steps.[185] This is both time and energy-consuming.

Conversion of Porphyrins or Chlorins into BChls

This method is reported to be straightforward. First and foremost, it is cautioned that the use of classical reductants such as palladium on carbon (PD-C) or platinum and hydrogen (H_2/Pt) are not ideal for this type of reaction because they reduce *meso*-positions of the macrocycles, thereby not producing the desired BChls. In contrast, the use of ascorbic acid produces dyads with Chl and BChl-like spectra, but these

chromophores were reported to revert to their unreduced form in the dark. It was later discovered that the use of diimide as a reductant, on the other hand, has proved to be effective in this regard. This compound is reported to be an excellent syn-reduction reductant for the β–β'-double bonds of porphyrins and proceeds to completion upon producing *iso*-BChls or BChls.

p-Toluenesulfonylhydrazide is converted into diimide when a base such as potassium carbonate is present. This methodology is, however, reported to produce a mixture of Chls and BChls (**Scheme 5**) which can be difficult to separate due to the closeness of their molecular weights.

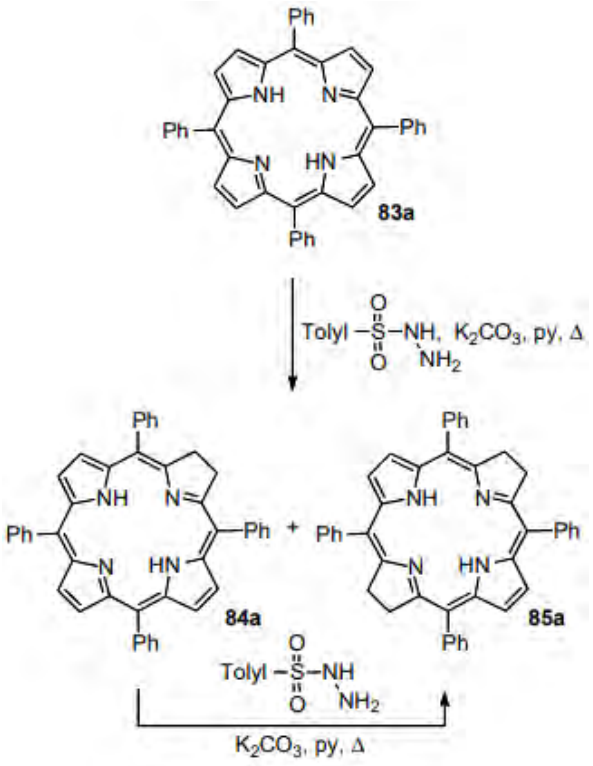

Scheme 5: The reduction of a free base porphyrin using *p*-toluenesulfonylhydrazide and potassium carbonate.

Reduction can also be performed under solvent-free conditions by working with a temperature above 150 °C and excess *p*-toluenesulfonylhydrazide under vacuum.

This method is reported to be faster than the one mentioned above, with the added advantage of producing higher yields of BChls than Chls.[185]

1.14 Metal insertion

Having briefly discussed the different synthetic routes for porphyrinoids, it is important to also discuss how metals are inserted in the core of these molecules in order to induce the much-needed heavy atom effect (**Scheme 6**).

To date, there are four types of routes followed for metalation.

The acetic acid acetate method.

1. The pyridine method.
2. The Buchler's acetylacetonate method.
3. Adler's dimethylformamide (DMF) method.

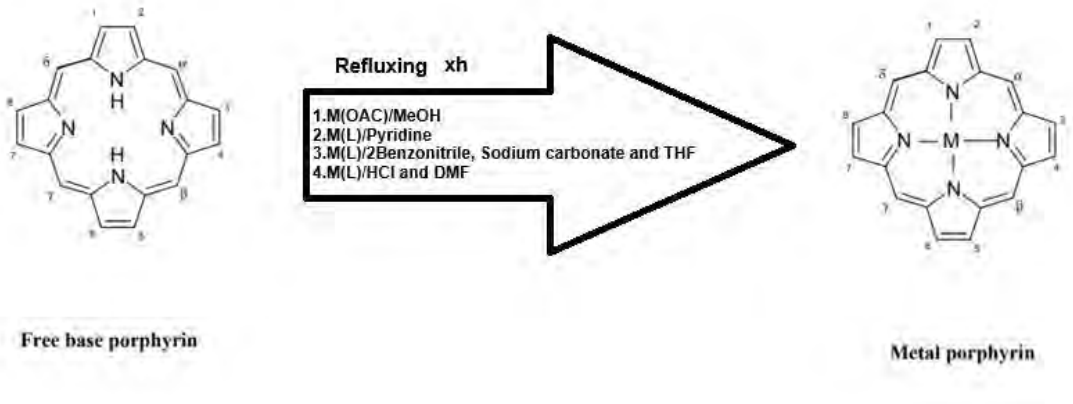

Scheme 6: The different metalation routes that are available for porphyrinoids.

Metalating porphyrinoids is a multi-step process that begins with the deprotonation of the free base porphyrinoids, followed by the dissociation of the metal from its salt and

ligand coordination. This then induces charge adjustment across the newly formed complex. Lastly, the complete coordination of the metal ion takes place. It is reported that the deprotonation of the porphyrinoid and the complete dissociation of the metal salt are highly dependent on the type of solvent used, since it has to solubilise both the chromophore and the metal salt. Furthermore, it is highly cautioned that this solvent should not be too acidic as that could lead to the decomposition of the reactants. A wide range of organic solvents have been tested and tried for this role. The ones that proved efficiency coupled with refluxing included acetic acid, formic acid, propionic acid, methanol, benzonitrile and *N,N*-dimethylformamide.[186,187,188]

The other objective is to introduce a charge to the porphyrinoids. Reports show that inducing a charge on these chromophores significantly increases their solubility and, thereby, their cellular uptake. This can be achieved by metalating the macrocyclic ring, protonating nitrogen atoms on the *meso*-aryl or attaching a charged moiety to the porphyrinoid. In a similar manner to metalation, the latter process relies on the solvent used. Organic solvents such as dimethylformamide, tetrahydrofuran and toluene are preferred to fulfil this purpose.[189] A study conducted by Magadla *et al.* (**Scheme 7)** and an MSc thesis by Choonzo Chiyumba illustrated this phenomenon excellently.[151,188]

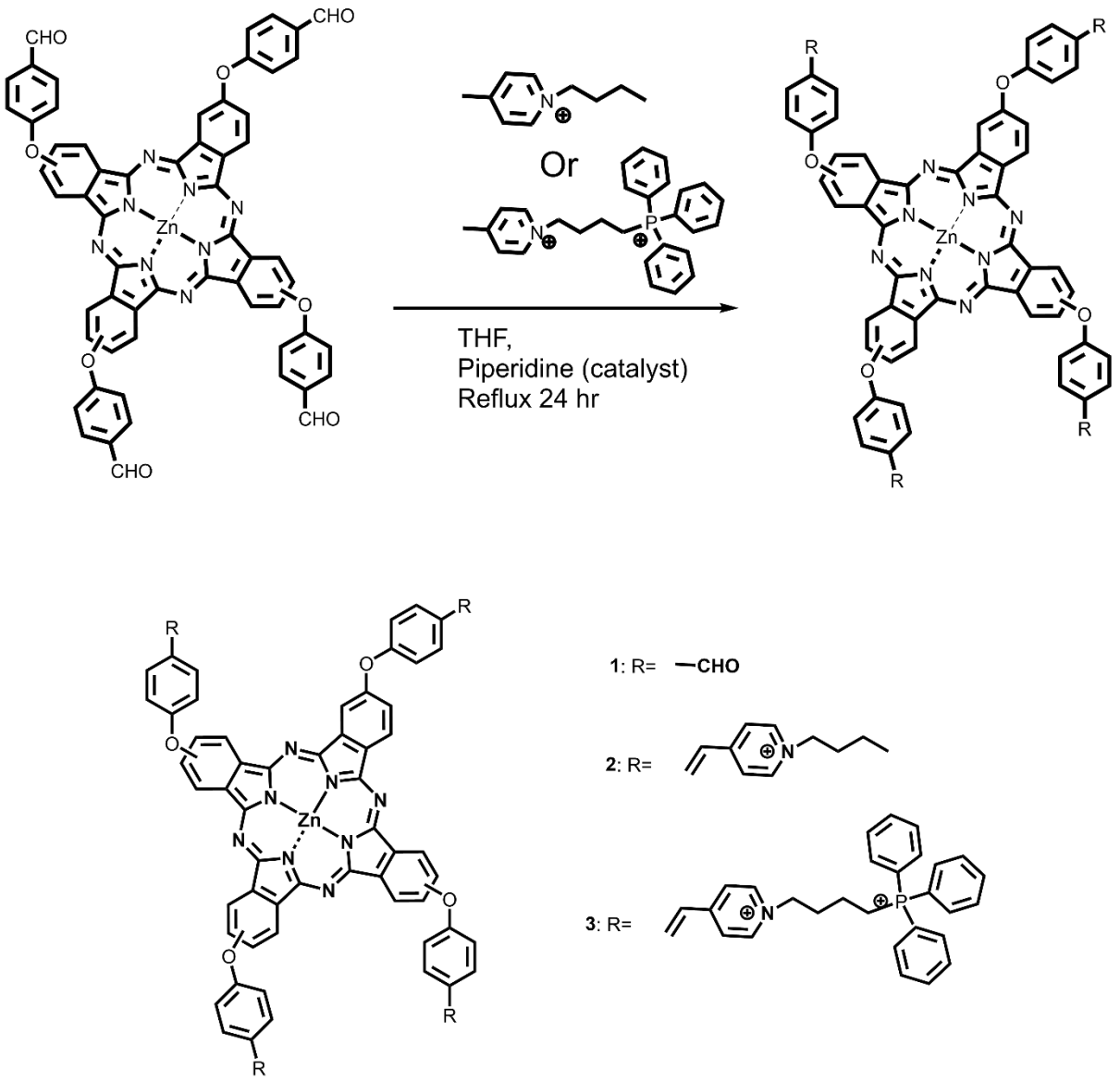

Scheme 7: Different routes taken to induce a charge on porphyrinoids. Reproduced with permission from Ref. 150, © Royal Society of Chemistry 2021.

Aims and Rationale

The aim of this project is to prepare novel structurally modified porphyrin-type dyes that absorb far into the near-infrared region. Identifying suitable dyes that absorb significantly in the 700−800 nm region is particularly important from an African perspective, since melanin significantly limits the penetration of laser light into human tissue in the 600−700 nm region, where the first and second-generations of photosensitiser dyes usually absorb. The porphyrin analogues that will be investigated in this regard are bacteriochlorins (BChls), which are known to have suitable optical properties that are potentially suitable in this regard. The reduction of two peripheral pyrrole bonds modifies the energies of the frontier π-MOs and results in a marked red shift of the main spectral bands. My motivation will be to conduct research that will provide novel photosensitiser dyes that will enhance the use of PDT and PACT in an African context as a treatment for a wide range of different cancers and microbes.

The second step would be to metalate the BChls in order to introduce a heavy central metal to increase the singlet oxygen quantum yields for high production of reactive oxygen species and singlet oxygen and further red shift the lowest energy absorption band of the BChls in the therapeutic window for deep tissue penetration for effective PDT. Thirdly, the dyes will be positively charged to promote solubility and lipophilicity. Then, the last step will be to conjugate the BChls with nanoparticles to transport them to the target site via the enhanced permeability and retention effect.

Objectives

1. Synthesis, purification, characterisation and photophysicochemical studies of the porphyrins and BChls.
2. Molecular modelling studies.
3. Synthesis and characterisation of the nanoparticles and their conjugation to the dyes.
4. PDT studies against MCF-7 breast cancer cells.
5. PACT studies against Gram-(+) and Gram-(−) bacteria.

2. EXPERIMENTAL

REAGENTS USED

3-Quinolinecarboxaldehyde, 4-quinolinecarboxaldehyde, 2,3,4,5,6-pentafluorobenzaldehyde, propionic acid, nitric acid, pyrrole, sodium hydroxide, pyridine, potassium carbonate, *p*-toluenesulfonylhydrazide, dimethysulfoxide (DMSO), hexane, Tin(II)Chloride, $CDCl_3$, DMSO-d_6 and D_2O were obtained from Sigma-Aldrich. Chloroform was obtained from Minema. Type II water for the *in vitro* studies was sourced from an Elga Purelab Chorus 2 (RO/DI) system. Dulbecco's modified Eagle's medium (DMEM) and phosphate-buffered saline (DPBS) were supplied by Lonza®. MCF-7 cells were obtained from Cellonex®, while heat-inactivated fetal calf serum (FCS), 100 µg/mL streptomycin-amphotericin B, penicillin-streptomycin-amphotericin B mix, and 100 units/mL penicillin at tissue culture grade were obtained from Biowest®. Photodynamic antibacterial studies were carried out with *S. aureus* and *E. coli* (ATCC® 25923™ and 25922™). Pyrrole and pyridine were distilled before use. Soot was collected from a generator exhaust. The synthesis of (4-bromobutyl)triphenylphosphonium that is used to introduce a TPP^+ moiety has been reported previously by Mack and coworkers.[151]

INSTRUMENTATION

- Bruker AMX 600 and 400 MHz and 85 MHz benchtop NMR spectrometers were used to obtain the ^1H NMR data. The spectra were measured at ambient temperature using deuterated solvents ($CDCl_3$, DMSO-d_6 and D_2O).
- Mass spectra were obtained using a Bruker Auto-FLEX III Smartbeam MALDI-TOF mass spectrometer using α-cyano-4-hydroxycinnamic acid as a matrix in either negative or positive ion mode with an m/z range of 400−1500 amu.

- A Shimadzu UV-2550 spectrometer was used to measure ground state electronic absorption spectra at room temperature with a wavelength range of 300−800 nm in a 1 cm path length cuvette.
- A Varian Eclipse spectrofluorimeter was used for fluorescence quantum yield studies.
- An Ekspla NT 342B-20-AW laser with an Nd:YAG that pumps a 420−2300 nm optical 30 parametric oscillator (OPO) (355 nm, 2.0 mJ/7 ns, 20 Hz) to provide monochromatic light at a crossover wavelength for the standard and sample for singlet oxygen quantum yields.
- The Eskpla NT342B-20-AW laser also provided the pump beam for an Edinburgh Instruments LP980 transient absorption spectrometer fitted with a PMT-LP (Hamamatsu R928P) and ICCD camera (Andor DH320T-25F03). This instrument was used to determine the triplet state lifetime values.
- A Modulight® Medical Laser (ML) 7710-680 system, fitted with a Thorlabs LED for PDT and PACT studies.
- A Scan® 500 automatic colour colony counter was used for the PACT activity studies.
- Synergy 2 multi-mode microplate reader (BioTek®) was used for the PDT activity studies.
- Porvair 25 cm^2 vented flasks were used during MCF-7 cell culture preparations.

SYNTHESIS

Free Base Porphyrins

To synthesise the porphyrins, the Adler-Longo method was utilized (**Scheme 8**). The reaction process entailed refluxing at a 1:1 molar ratio of the appropriate benzaldehyde (2 g), which in this instance were 3-quinoline carboxaldehyde, 4-quinoline carboxaldehyde, and 2,3,4,5,6-pentafluorobenzaldehyde, respectively, with distilled pyrrole for roughly 2 h or more depending on the aldehyde used, at 140°C in 50 mL propionic acid. Then, the cooled mixture was neutralised with a solution of sodium hydroxide pellets, gravity filtered, and the filtered porphyrin product was purified on a silica column chromatography with 50:50 Hexane/Chloroform eluent. **Scheme 8** below depicts the reaction process.

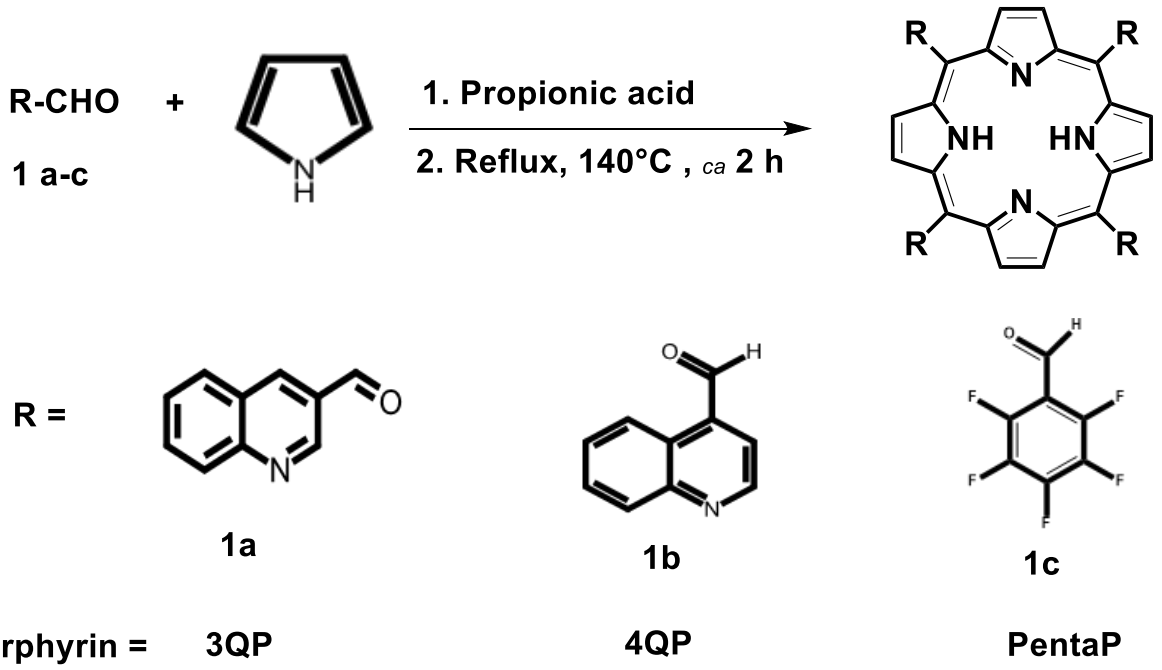

Scheme 8: The synthesis of free base porphyrins.

The synthesised free base porphyrins were as follows:

5,10,15,20-tetra(quinolin-3-yl)porphyrin (**3QP**) – Brown crystals yield (1.50 g, 52.3% yield) ^{1}H NMR (80 MHz, DMSO-d_6) δ 9.84 (s, 2H), 8.95 (s, 8H), 8.49 (s,2H), 8.07 (s, 2H), 7.95 (s, 4H), 7.30 (s, 8H), 7.02 (s, 2H), 6.38 (d, J = 15.3 Hz, 4H), −2.58 (s, 2H) ppm. (MALDI-TOF) = 819.71 m/z $[M+H]^+$ obtained, 818.71 m/z calculated.

5,10,15,20-tetra(quinolin-4-yl)porphyrin (**4QP**) – Black crystals yield = (2.00 g, 69.7% yield) ^{1}H NMR (80 MHz, DMSO-d_6) δ 9.75 (s, 2H), 9.36 (s, 2H), 8.52 (s, 2H), 8.34 (s, 2H), 7.72 (s, 8H), 7.08 (s, 8H), 6.45 (s, 8H), −2.36 (s, 2H) ppm. (MALDI-TOF) = 819.59 m/z $[M+H]^+$ obtained, 818.71 m/z calculated.

5,10,15,20-tetrakis(perfluorophenyl)porphyrin (**PentaP**) – Red crystals (1.00 g, 37.3% yield) ^{1}H NMR (80 MHz, $CDCl_3$) δ 9.40 (s, 8H), 2.43 (s, 8H), −2.43 (s, 2H) ppm. (MALDI-TOF) = 975.71 m/z $[M+H]^+$ obtained, 974.06 m/z calculated.

Sn(IV) Porphyrins

For the insertion of Sn(II) chloride, quantities of 3:1 metal salt and 1 g of the relevant porphyrin, respectively, were refluxed in 15 mL pyridine at 170 °C for 2 h, then cooled, washed with deionised water and lastly purified by a silica column chromatography using 100% chloroform. **Scheme 9** below depicts the reaction.

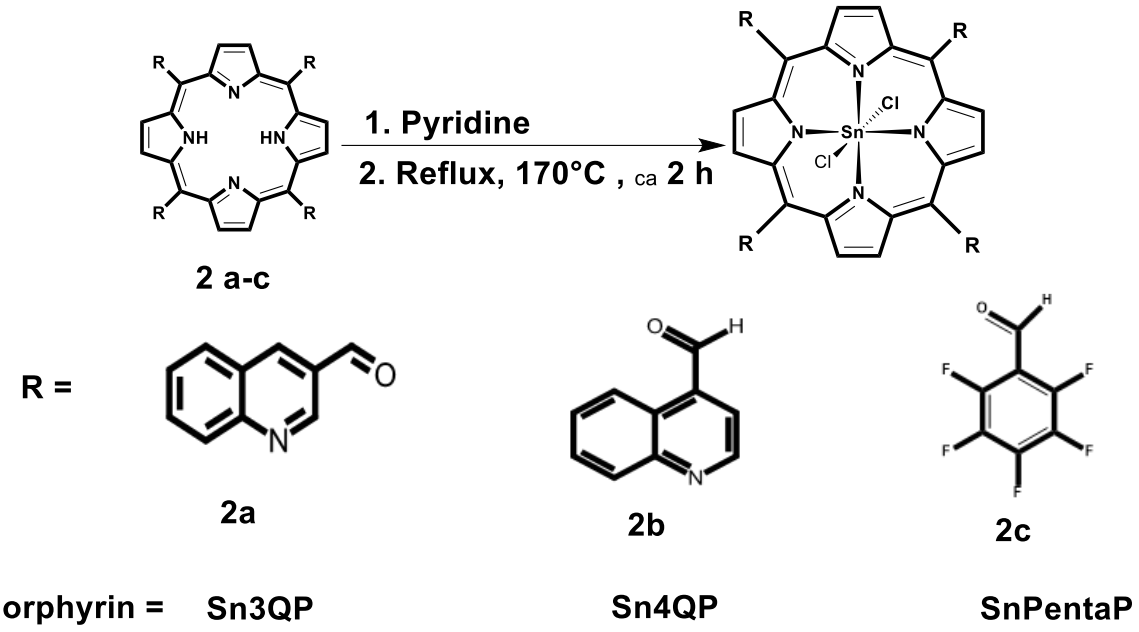

Scheme 9: The synthesis of metal porphyrin complexes.

5,10,15,20-tetra(quinolin-3-yl)porphyrin tin(II)-dichloride (**Sn3QP**) - Green crystals (0.61 g, 20.3% yield) ^{1}H NMR (80 MHz, DMSO-d_6) δ 9.75 (s, 2H), 9.36 (s, 2H), 8.52 (s, 2H), 8.34 (s, 2H), 7.72 (s, 8H), 78H), 6.45 (s, 8H) ppm. (MALDI-TOF) = 971.49 m/z $[M\text{-}Cl]^+$ obtained, 1006.53 m/z calculated.

5,10,15,20-tetra(quinolin-4-yl)porphyrin tin(II)-dichloride (**Sn4QP**) - Green crystals (1.00 g, 33.3% yield) ^{1}H NMR (80 MHz, DMSO-d_6) δ 9.75 (s, 2H), 9.36 (s, 2H), 8.52 (s, 2H), 8.34 (s, 2H), 7.72 (s, 8H), 78H), 6.45 (s, 8H) ppm. (MALDI-TOF) = 971.49 m/z [M-Cl] obtained, 1006.53 m/z calculated.

5,10,15,20-tetrakis(perfluorophenyl)porphyrin tin(II)-dichloride (**SnPentaP**) – Blue/Purple crystals (0.85 g, 28.3% yield) ^{1}H NMR (80 MHz, $CDCl_3$) δ 9.39 (s, 8H) ppm. (MALDI-TOF) = 1127.39 m/z $[M-Cl]^+$ obtained, 1162.15 m/z calculated.

Quaternised Porphyrins

In order to induce a cationic charge on the porphyrins, TPP^+ moieties were conjugated to the quinoline-substituted porphyrins at the nitrogen atom of the *meso*-groups via butyl linkers. This was done by stirring (4-bromobutyl)triphenylphosphonium (4.00 g, 90 mmol) with the metalated porphyrin (1.00 g, 10 mmol) in DMSO for 72 h. The solvent was removed under vacuum, and the product was obtained in near quantitative yield. **Scheme 10** below depicts the reaction.

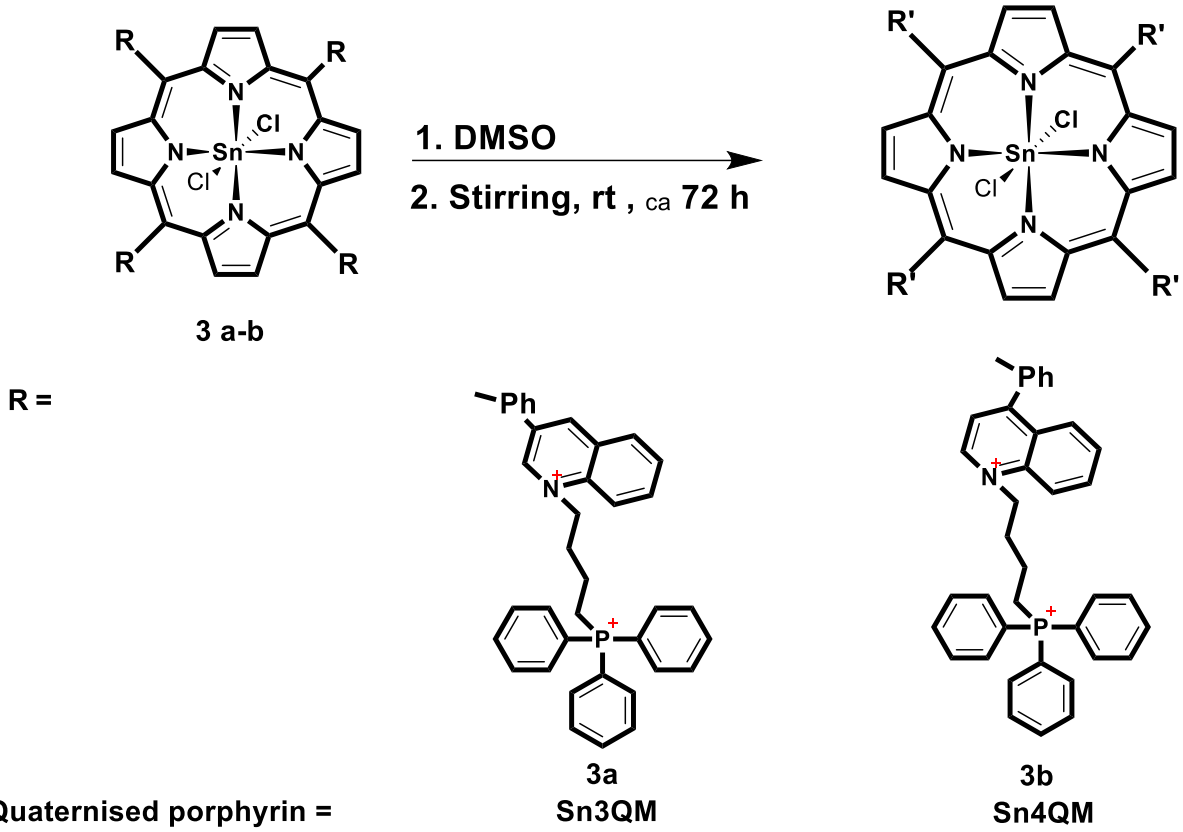

Scheme 10: The synthesis of quaternised porphyrins.

5,10,15,20-tetra(quinolin-3-yl)porphyrin tetra(butyltriphenylphosphonium) tin(II)-dichloride (**Sn3QM**) – Milky Green crystals. ^{1}H NMR (80 MHz, D_2O + DMSO-d_6) δ 9.74 (s, 11H), 7.91 (s, 44H), 5.04 (s, 13H), 3.84 (s, 21H), 2.58 (s, 16H), 2.31 (s, 24H) ppm. (MALDI-TOF) = 2222.31 m/z obtained, 2222.66 m/z calculated.

5,10,15,20-tetra(quinolin-4-yl)porphyrin tetra(butyltriphenyl-phosphonium) tin(II)-dichloride (**Sn4QM**) – Creamy crystals. ^{1}H NMR (80 MHz, D_2O + DMSO-d_6) δ 9.74 (s, 11H), 7.91 (s, 44H), 5.04 (s, 13H), 3.84 (s, 21H), 2.58 (s, 16H), 2.31 (s, 24H) ppm. (MALDI-TOF) = 2222.66 m/z obtained, 2222.66 m/z calculated.

Bacteriochlorins

The solvent-free method was utilised with slight modifications to obtain optimal yields while minimising destabilisation/degradation of the desired product. Firstly a 3:1 *p*-toluenesulfonylhydrazide / porphyrin(0.50 g) mixture was ground for 30 min with 10 min UV-visible absorption monitoring intervals to constantly check the disappearance of the chlorin peak around 650 nm and a subsequent increase in the BChl peak at *ca.* 740 nm. When this peak becomes more intense than that of the chlorin, the mixture was heated with constant stirring at 80°C instead of at reflux. It took 15 min to obtain the stable BChl target product. The product was purified by silica column chromatography with chloroform as the eluent. **Scheme 11** depicts the reaction route.

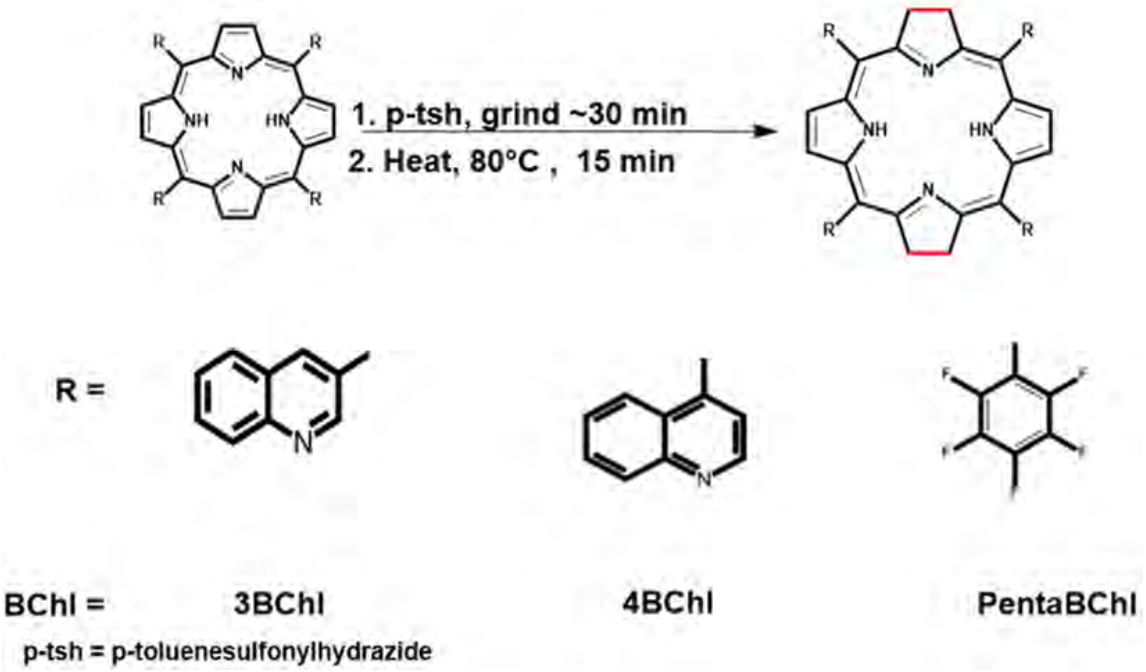

Scheme 10: The synthesis of free base BChls.

5,10,15,20-tetra(quinolin-3-yl)-7H,8H,17H,18H-porphyrin (**3QBChl**) – Brown crystals (0.5 g, 41.7% yield) were obtained. ^{1}H NMR (80 MHz, $CDCl_3$) δ 7.94 (s, 6H), 7.84 (s, 4H), 7.49 (s, 4H), 7.38 (s, 6H), 7.24 (s, 4H), 7.14 (s, 2H), 6.32 (s, 4H), 2.54 (s, 8H) ppm. (MALDI-TOF) = 823.31 m/z $[M+H]^+$ obtained, 822.32 m/z calculated.

5,10,15,20-tetra(quinolin-4-yl)-7H,8H,17H,18H-porphyrin (**4QBChl**) – Black crystals (0.43 g, 35.8% yield) were obtained. ^{1}H NMR (80 MHz, D_2O) δ 7.83 (s, 4H), 7.72 (s, 2H), 7.68 (s, 2H), 7.58 (s, 4H), 7.49 (s, 4H), 7.34 (s, 4H), 7.24 (s, 4H), 7.10 (s, 4H), 2.43 (s, 8H), −2.67 (s, 2H) ppm. (MALDI-TOF) = 822.32 m/z obtained, 822.32 m/z calculated.

5,10,15,20-tetrakis(perfluorophenyl)-7H,8H,17H,18H-porphyrin (**PentaBChl**) – Black crystals (1 g, 83.3% yield) were obtained. ^{1}H NMR (80 MHz, $CDCl_3$) δ 9.39 (s, 8H) ppm, 7.46 (s, 2H), 7.16 (s, 2H), 2.34 (s, 8H), −2.74 (s, 2H) ppm. (MALDI-TOF) = 978.09 m/z obtained, 978.40 m/z calculated.

Sn(IV) Bacteriochlorins

The insertion of tin(II) chloride into the BChls proved to be futile for the quinoline-substituted porphyrins. The methodology followed to metalate **PentBChl** involved refluxing the BChl (1.00 g, 0.43 mmol) dissolved in Methanol with the metal salt (2.00 g, 10 mmol) dissolved in chloroform at 15 °C for 24 h in, the solvent ratio was 1:1 (v/v). This was then followed by vacuum drying and silica chloroform column chromatography. **Scheme 12** depicts the reaction route.

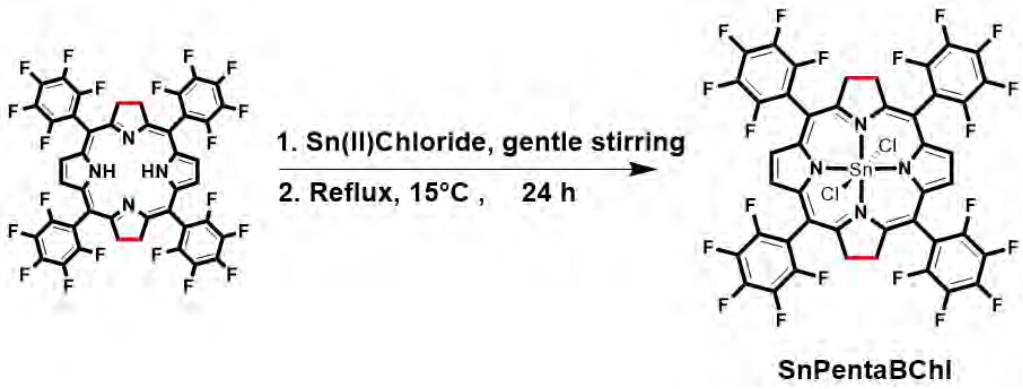

Scheme 11: The synthesis of metal BChl complexes.

5,10,15,20-tetrakis(perfluorophenyl)-7H,8H,17H,18H-porphyrin (**SnPentBChl**) – Green crystals (500 mg, 16.7% yield) were obtained. ^{1}H NMR (80 MHz, $CDCl_3$) δ 7.53 (s, 2H), 7.38 (s, 2H), 2.41 (s, 8H) ppm. (MALDI-TOF) = 1164.65 m/z, $[M-H]^-$ obtained, 1166.17 m/z calculated.

Quaternised Bacteriochlorins

The quinoline-substituted BChls were quaternised in the same manner as the porphyrins above (**Scheme 13**), with the only difference being the duration of the reaction, which was 4 h, to avoid destabilisation of the BChls.

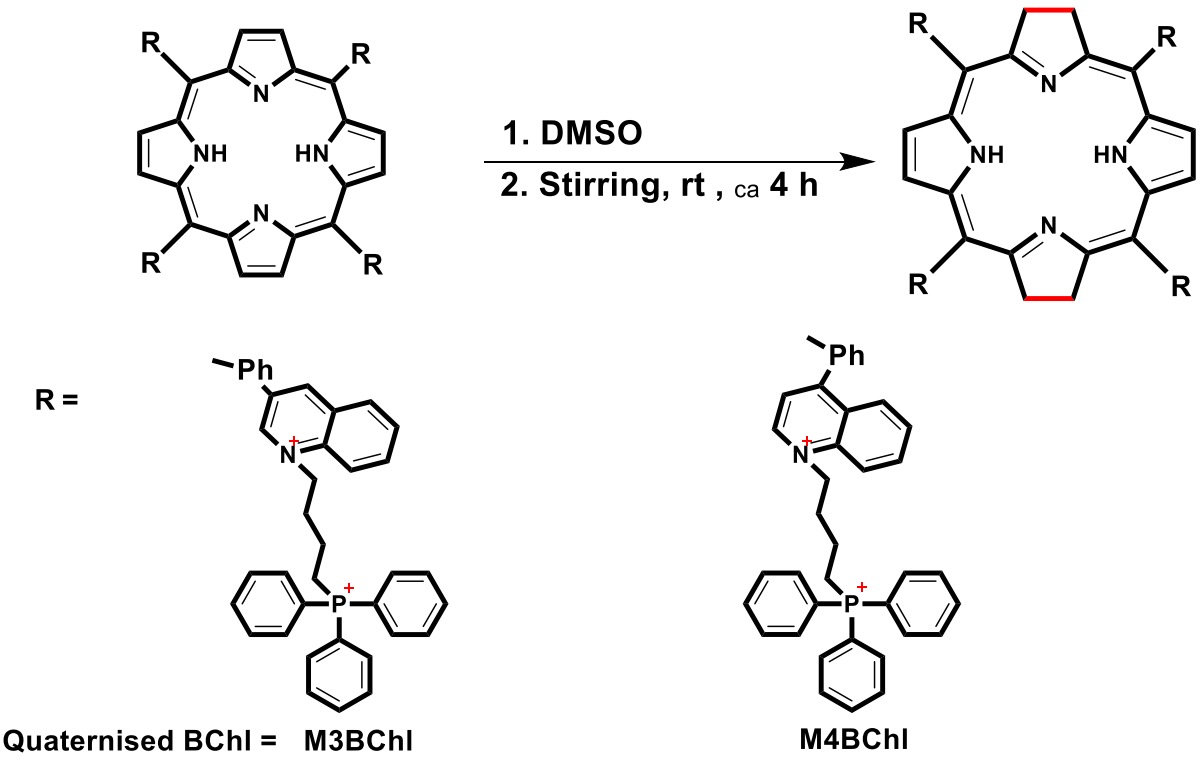

Scheme 12: The synthesis of quaternised BChls.

5,10,15,20-tetra(quinolin-3-yl)-7H,8H,17H,18H-porphyrin tetra(butyltriphenyl-phosphonium) (**M3QBChl**) – Brown crystals were obtained. ^{1}H NMR (80 MHz, D_2O) δ 7.63 (dd, J = 8.1, 3.9 Hz, 18H), 7.40 (s, 10H), 7.33 (s, 10H), 7.22 (s, 10H), 7.09 (s, 8H), 7.02 (s, 6H), 6.90 (s, 6H), 3.37 (s, 10H), 2.68 (s, 44H), −2.85 (s, 2H) ppm. (MALDI-TOF) = 2040.23 m/z $[M+H]^+$ obtained, 2038.87 m/z calculated.

5,10,15,20-tetra(quinolin-4-yl)-7H,8H,17H,18H-porphyrin tetra(butyltriphenyl-phosphonium) (**M4QBChl**) – Black crystals were obtained. ^{1}H NMR (80 MHz, D_2O) δ 7.63 (dd, J = 8.1, 3.9 Hz, 18H), 7.40 (s, 12H), 7.33 (s, 6H), 7.22 (s, 10H), 7.09 (s, 6H),

7.02 (s, 6H), 6.90 (s, 6H), 3.37 (s, 10H), 2.68 (s, 44H), −2.85 (s, 2H) ppm. (MALDI-TOF) = 2038.18 m/z obtained, 2038.87 m/z calculated.

Failed Syntheses

As has been indicated previously, the solvent method and metal insertion reactions of the quinoline-substituted BChls were unsuccessful. **Schemes 14** and **15** below illustrate the failed synthetic routes explored.

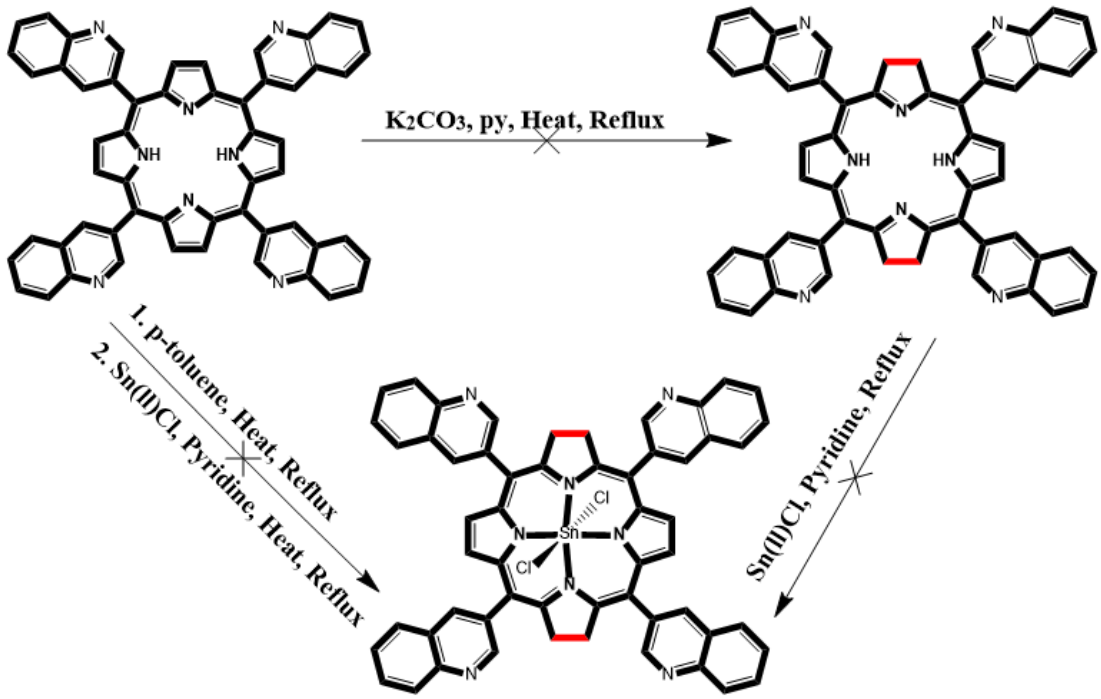

Scheme 13: Solvent method of **3BChl** synthesis as well as its metalation.

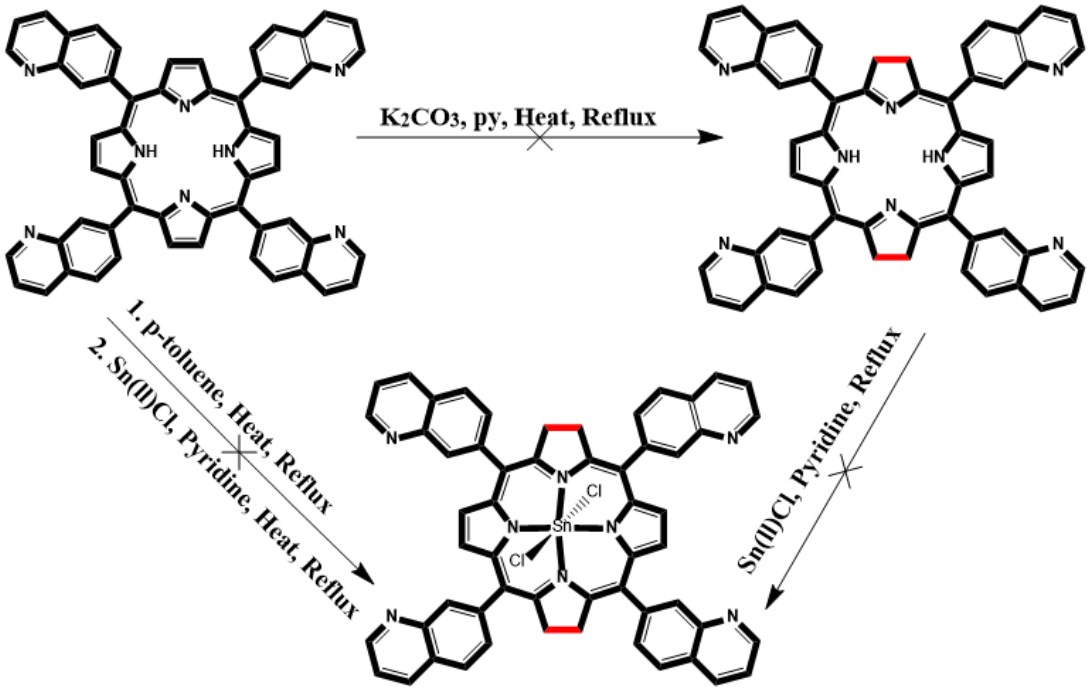

Scheme 14: Solvent method of **4BChl** synthesis as well as its metalation.

The synthesis of the carbon dots involved the refluxing of black carbon (5.00 g) collected from a generator exhaust, which was then dissolved in 200 mL 5 M Nitric acid and refluxed at 100 °C at varying temperatures for 12, 24 and 50 h. Their morphology and sizes were inconsistent, so they were not used in the study. **Figure 19** provides the SEM images of the NPs at the above-mentioned temperatures respectively.

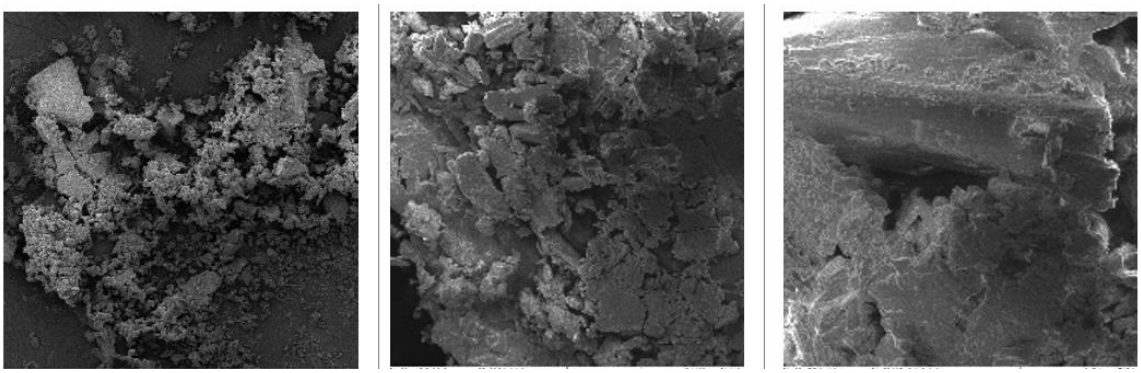

Figure 19: NPs obtained at 12, 24 and 50 hours of refluxing in 5 M Nitric acid.

2.3.1PHOTOPHYSICOCHEMICAL MEASUREMENTS

UV-VISIBLE ABSORPTION SPECTROSCOPY: To get the absorbance spectra of a substance in solution or as a solid, ultraviolet-visible (UV-vis) spectroscopy is used. The absorbance of electromagnetic radiation or light energy, which excites electrons from the compound or material's ground state to its first singlet excited state, is what is actually being detected spectroscopically. The wavelength range of the UV-visible portion of the electromagnetic spectrum is 800 to 200 nm, and Beer-Lambert's Law in Equation 1 depicts the principle of this spectroscopy:

$$A = \varepsilon bc \qquad [1]$$

A is the absorbance, ε is the molar extinction coefficient with the units ($M^{-1}cm^{-1}$), b is the path length of the sample holder or cuvette (1 cm), and c is the molar concentration of the sample solution.

MASS SPECTROMETRY: This a spectroscopic tool that is used to measure the mass-to-charge ratio (m/z) of molecules present in a sample. This is done by separating ionized particles like atoms, molecules or compounds by using the differences in the ratios of their charges with respect to their masses, and this is used to determine the molecular weight of the molecules.

^{1}H NMR SPECTROSCOPY: Proton nuclear magnetic resonance (^{1}H NMR) spectroscopy is used to study the radiofrequency interactions of molecules and electromagnetic interactions with the nuclei of the molecules analysed. This tool is used not only to provide information about the molecular structure of a sample but also to provide insights into how pure the sample is.

PHOTOSTABILITY STUDIES: The goal of stability testing is to define a time frame for repeat testing of a compound by demonstrating how its quality and reproducibility changes over time and in response to various environmental conditions, including temperature, humidity, and light. As with the UV-visible absorption spectra mentioned above, the principle governing stability studies is also Beer-Lambert's law, but in this case, the scrutiny is on the molar extinction coefficient instead of absorbance.

FLUORESCENCE QUANTUM YIELD (Φ_F): This is the ratio between the number of photons emitted and absorbed. The fluorescence quantum yield defined by Equation 2 below outlines the variables considered in the calculation of this parameter.

$$\Phi_F = \Phi_{F(std)} \frac{F \cdot A_{(std)} \cdot \eta^2}{F_{(std)} \cdot A \cdot \eta^2_{(std)}} \qquad [2]$$

F is the integrated fluorescence intensity of the sample, whereas the F_{std} is that of the standard. A and A_{std}, on the other hand, are the absorbance values of the sample and standard, respectively. Usually, the standard utilised for the calculation is zinc tetraphenylporphyrin (ZnTPP), which is reported to have a value of Φ_F = 0.039 in DMSO.[191]

FLUORESCENCE LIFETIME (T_F): This is the time the dye spends in the excited singlet state before returning to the ground state by fluorescence. In calculating the lifetimes, a time-correlated single photon counting technique (TCSPC) is used to measure the time-dependent fluorescence intensity profile. The light is emitted after the sample is excited by a pulsed laser. The time elapsed between excitation by laser pulse and the detection of a fluorescence photon is measured. Repeating this process establishes the distribution of the time differences. Fitting an exponential curve to this

distribution can be used to calculate the τ_F value, which is the time taken for the intensity to fall to the ratio of 1/e of the initial value.

SINGLET OXYGEN QUANTUM YIELD (Φ_Δ): It is pivotal to quantify the formation of $^1O_2$ because PDT and PACT heavily rely on their activity and the efficiency of the PS used. This particular quantum yield is defined by the ratio between the number of $^1O_2$ molecules generated for every particle of photon absorbed by a PS Equation 3 below.

$$\Phi_\Delta = \Phi_\Delta^{std} \cdot \frac{I_{abs}}{I_{abs}^{std}} \quad [3]$$

Where I_{abs} is the rate of light absorption by the sample whilst I_{abs}^{std} is the rate of light absorption by the standard. Φ_Δ is the known (standard) $^1O_2$ quantum yield. Zinc tetraphenylporphyrin (ZnTPP) is often used as the standard ($\Phi_\Delta = 0.53^{ref}$) in the context of the comparative method using the degradation of the quencher 9,10-dimethylanthracene (DMA).[192]

PDT ACTIVITY STUDIES

The cells used for the PDT activity studies were MCF-7 breast cancer cells. Since several of the compounds were not cationic and had limited solubility in aqueous solution, these preliminary proof of principle anticancer investigations were carried out using 1% and 5% DMSO for the free base, quaternised, and metalated compounds, respectively. This was necessary due to issues with solubilizing the dyes. Additionally, for dependability, validity, and repeatability, they were completed in triplicate.

A substance's ability to inhibit a particular biological or biochemical process is measured by its IC_{50} value, which also shows how much of a pharmacological agent is needed to reduce biological activity by half. In order to calculate this value, After the cells were treated with the compounds, either with or without light irradiation, the cell viability was assessed using the WST-1 assay. Toxicity under both light and dark conditions was also assessed to evaluate whether these compounds would be ideal photosensitisers, which are only active when exposed to radiation. Equation 4 below was then used to calculate percentage viability.

$$\% \text{ Cell viability} = \frac{OD_{\lambda}Treatment}{OD_{\lambda}Control} \times 100 \qquad [4]$$

The malignant cell lines were grown in separate T75 cm^2 cell culture flasks using DMEM, which contained 10% FBS and 0.01% antibiotics (penicillin and streptomycin-amphotericin B). The cells were grown to 100% growth confluence by incubating them at 37°C under a 5% CO_2 supply. After that, the cells were seeded in DMEM medium in 96-well plates, and were incubated for 24 h under a 5% CO_2 atmosphere in an incubator. Following this incubation, the cells were once more incubated in the dark for 24 h, this time in a fresh DMEM mixture with varying quantities of the compounds (0, 20, 40, 60, 80 and 100 μM).

A different set of 96-well plates served as controls; these plates were loaded with new DMEM devoid of the synthesised compounds. The media containing the chemicals was removed once the specified incubation period had passed, and fresh DMEM free of phenol red was introduced. The cells were then exposed to light for 30 min using a Thorlabs LED fitted onto the casing of a Modulight 7710-680 medical laser and having a wavelength suitable for the compounds under study. The LEDs used were an M595L3 (250 mW/cm^2) for free base porphyrins, an M625L3 (240 mW/cm^2) for metalated and quaternised porphyrins and an M730L4 (160 mW/cm^2) for the BChls. The cells were cultured for a further 24 h after the clear DMEM medium was discarded and replaced with fresh DMEM with 10% FBS. An extra batch of cells treated with the compounds was prepared; no irradiation was applied to conduct dark toxicity studies. Following a 24-hour incubation period, the media was removed, DMEM-10% FBS was added, and the cells were left to incubate for a further 24-hour period. Following a 24-hour incubation period for both cell sets, the media was properly disposed of, and each well was filled with 25 µL (5 mg/mL) MTT diluted in PBS (phosphate-buffered saline). The cells were then incubated for 3 h in the absence of light. After that, the medium was cautiously disposed of.

A Molecular Devices Spectra Max M5 plate reader was used to measure the formazan absorbance at 545 nm. The percentage ratio of treated cells' absorbance to that of untreated control yields provides the cytotoxicity measurement. Using GraphPad Prism, nonlinear regression analysis was used to derive the IC_{50} values.

PACT ACTIVITY STUDIES

For the antibacterial activity investigations, multidrug-resistant Gram-(+) *Staphylococcus aureus (S. aureus)* and Gram-(−) *Escherichia coli (E. coli)* were utilised. In a similar manner to the PDT assay above, these antimicrobial investigations were carried out using 1% and 5% DMSO for the free base compounds, on the one hand, and quaternised and metalated compounds, on the other. In a similar manner to the PDT activity studies, this was necessary due to issues with solubilizing the dyes. Additionally, for dependability, validity, and repeatability, they were completed in triplicate. Added to this, toxicity under both light and dark conditions was also assessed to evaluate whether these compounds would be ideal photosensitisers that are only active when exposed to radiation.

The cultured bacterial colonies were inoculated into the nutritional broth and allowed to agitate for 24 h at 37°C in a rotating shaker. Afterwards, the culture aliquots were transplanted to 5 mL of fresh broth and cultured until they reached a mid-logarithmic phase (OD 620 nm ≈ 0.8). To determine the log reduction values in $CFU.mL^{-1}$, the optical density (OD) of the bacterial culture was measured using a Ledetect 96 from Labxim Products. Using PBS, the bacterial broth was centrifuged for 10 min at 4000 rpm to wash it. The collected bacteria were resuspended with a dilution factor of 10^{-2} in 100 mL PBS, which served as the bacterial stock solution. Different concentrations of fresh stock containing bacteria-compound stock solutions were made, ranging from 0, 20, 40, 60, 80 and 100 μM.

Following a 30 min incubation period to allow the compounds to internalise, 3 mL of the bacteria-PS stock solution, which had a volume of 6 mL, was pipetted onto each of two distinct 24-well plates. A Modulight 7710-680 medical laser fitted with a Thorlabs LED of the appropriate wavelength was used to irradiate one of the 24-well plates for

60 min, while the other was left in the dark. The LEDs used were an M595L3 (250 mW/cm^2) for free base porphyrins, an M625L3 (240 mW/cm^2) for metalated and quaternised porphyrins and an M730L4 (160 mW/cm^2) for the BChls. Following this, 100 µL of each sample concentration was pipetted onto nutrient agar-coated Petri dishes. The plates were left in the dark for 24 h at 37°C. To calculate the CFU/mL numbers for the colonies that formed, a Scan 500 Automatic Colony Counter from Healthcare Technologies was utilised. For the purpose of choosing an appropriate compound concentration that demonstrated the best antimicrobial activity characteristics for later time-dependency investigations, a concentration-dependence analysis was carried out.

The bacteria-compound solution was prepared for the time-dependent investigations, and the solution was introduced to a 24-well plate using the same process described above. 100 µL of the sample was pipetted onto nutrient agar-coated Petri dishes after each 10 min of radiation. The samples were then incubated for 24 h, and CFU/mL counting was done using the protocol described above. Survival fractions were determined by contrasting the control (Petri dishes containing only bacteria) with those treated with the PS dye. The investigation was conducted in triplicate in order to calculate the standard deviation.

3. SYNTHESIS & CHARACTERISATION

^{1}H NMR SPECTOSCOPY & MALDI-TOF MS

All of the dyes synthesised were characterised by ^{1}H NMR spectroscopy and MALDI-TOF MS.

Free base porphyrins

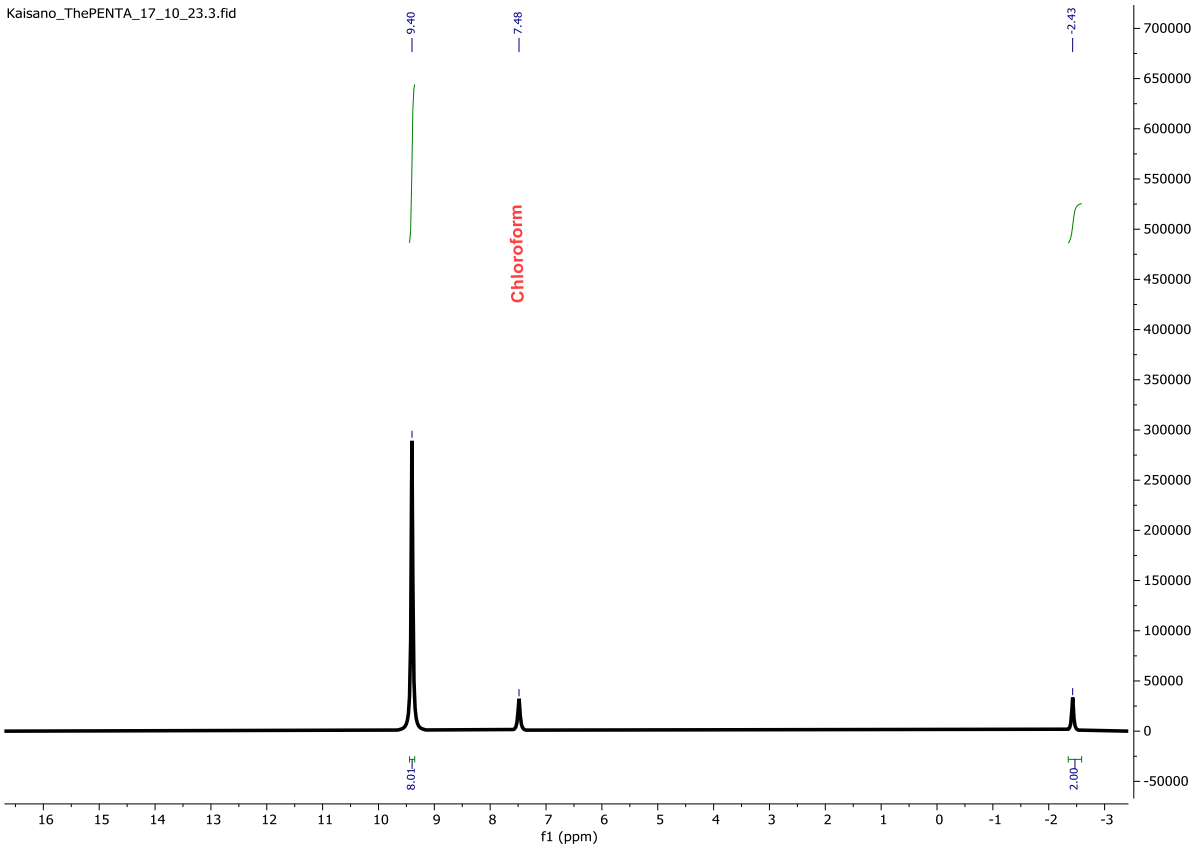

Figure 20: ^{1}H NMR spectrum of **PentaP** in $CDCl_3$.

The ^{1}H NMR spectrum for **PentaP** (**Figure 20**) exhibited the expected peak at −2.43 ppm for the two inner NH protons, the solvent peak at 7.26 ppm, and then, lastly, a peak in the aromatic region at 9.40 ppm, which arises from the eight protons on the outer ligand perimeter.

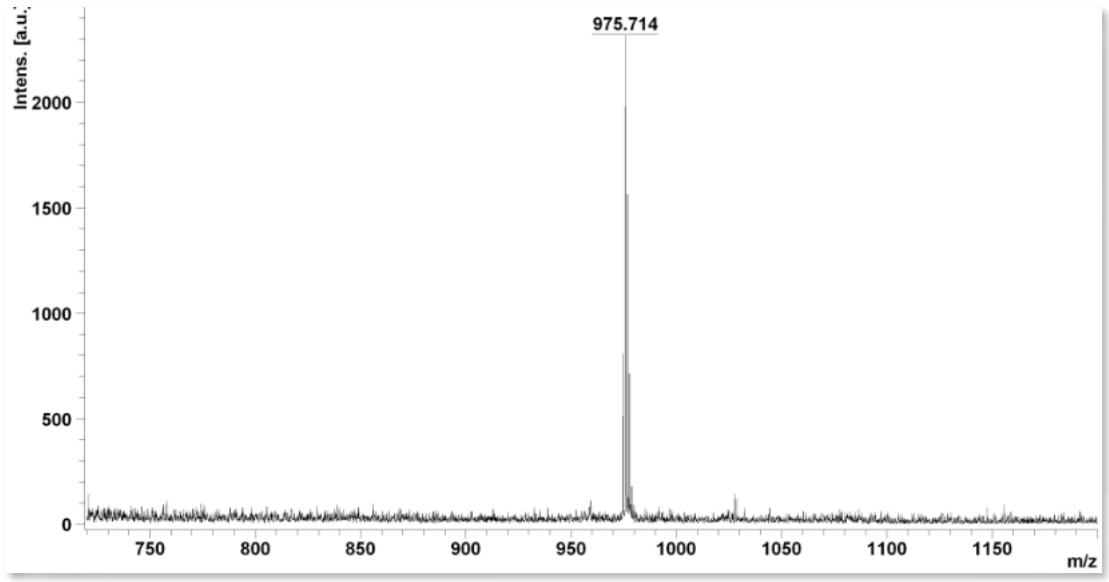

Figure 21: Mass spectral data for **PentaP**.

The obtained MALDI-TOF MS parent peak was 975.71 m/z (**Figure 21**), corresponding to an $[M+H]^+$ peak.

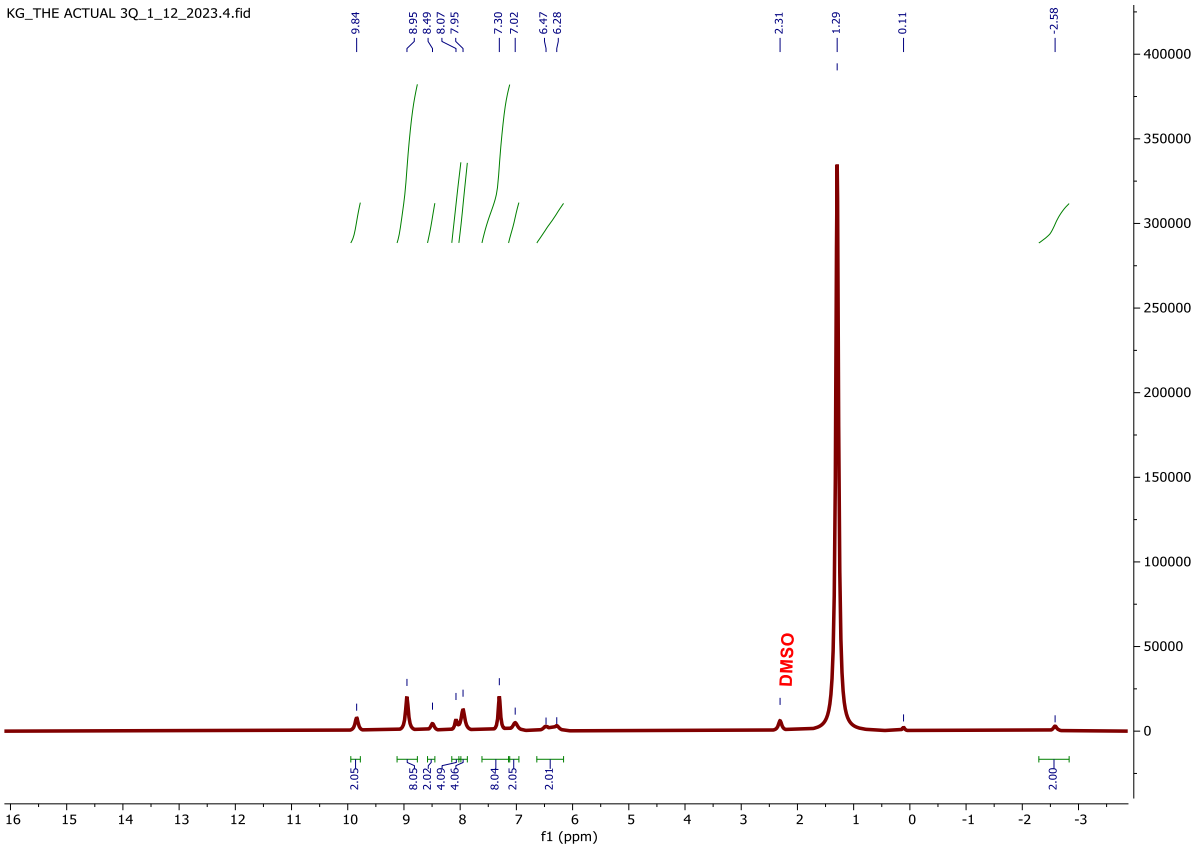

Figure 22: ^{1}H NMR spectrum of free base **3QP** porphyrin in DMSO-d_6.

3QP had the expected two proton peak at −2.58 ppm for the inner NH protons (**Figure 22**). Other peaks totalling to the anticipated thirty-two protons were observed in the aromatic region.

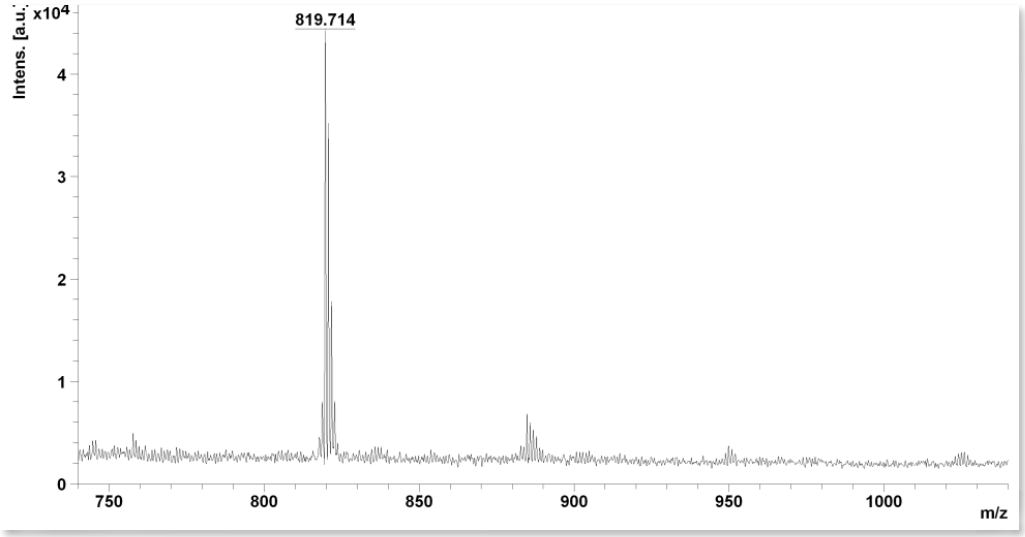

Figure 23: Mass spectral data for **3QP**.

The obtained MALDI-TOF MS parent peak was 819.71 m/z (**Figure 23**), corresponding to an $[M+H]^+$ peak. The characterisation data for **4QP** were broadly similar to those of **3QP**.

Sn(IV) porphyrins

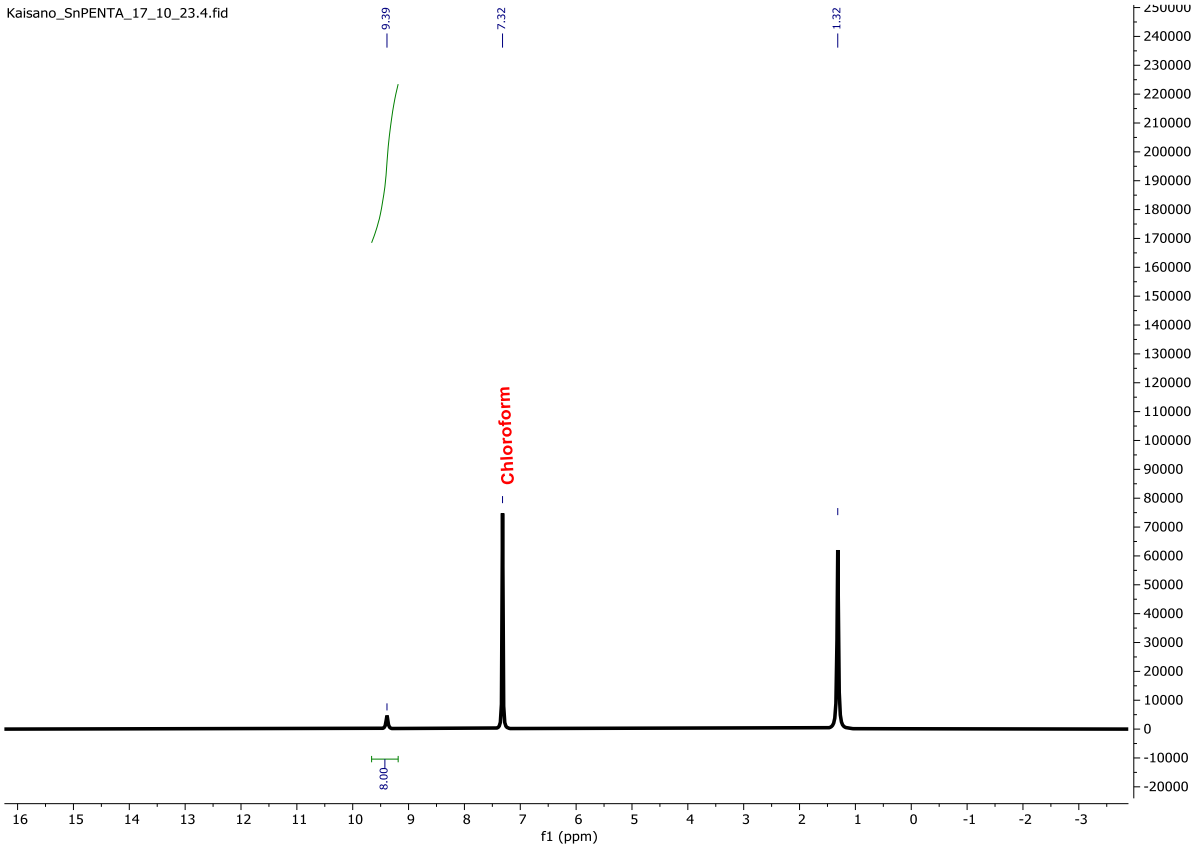

Figure 24: ^{1}H NMR spectrum of **SnPentaP** in $CDCl_3$.

The only significant difference between the ^{1}H NMR spectrum of a free base porphyrin and its metalated counterpart is the disappearance of the peak at *ca.* −2.5 ppm (**Figure 24**). This was the case for **SnPentaP**.

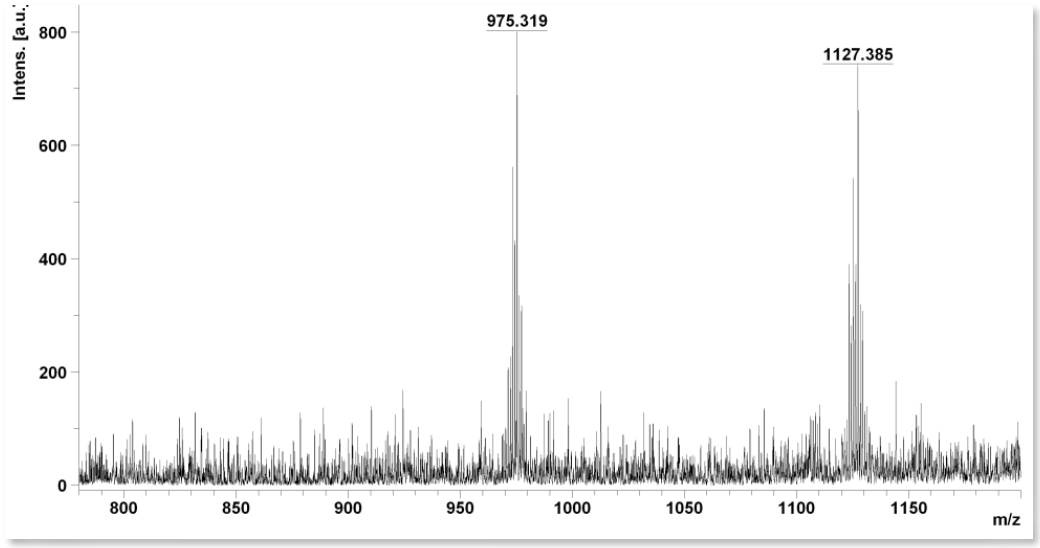

Figure 25: Mass spectral data for **SnPentaP**.

The MALDI-TOF MS peak at 1127.39 m/z corresponds to an $[M-Cl]^+$ peak (**Figure 25**).

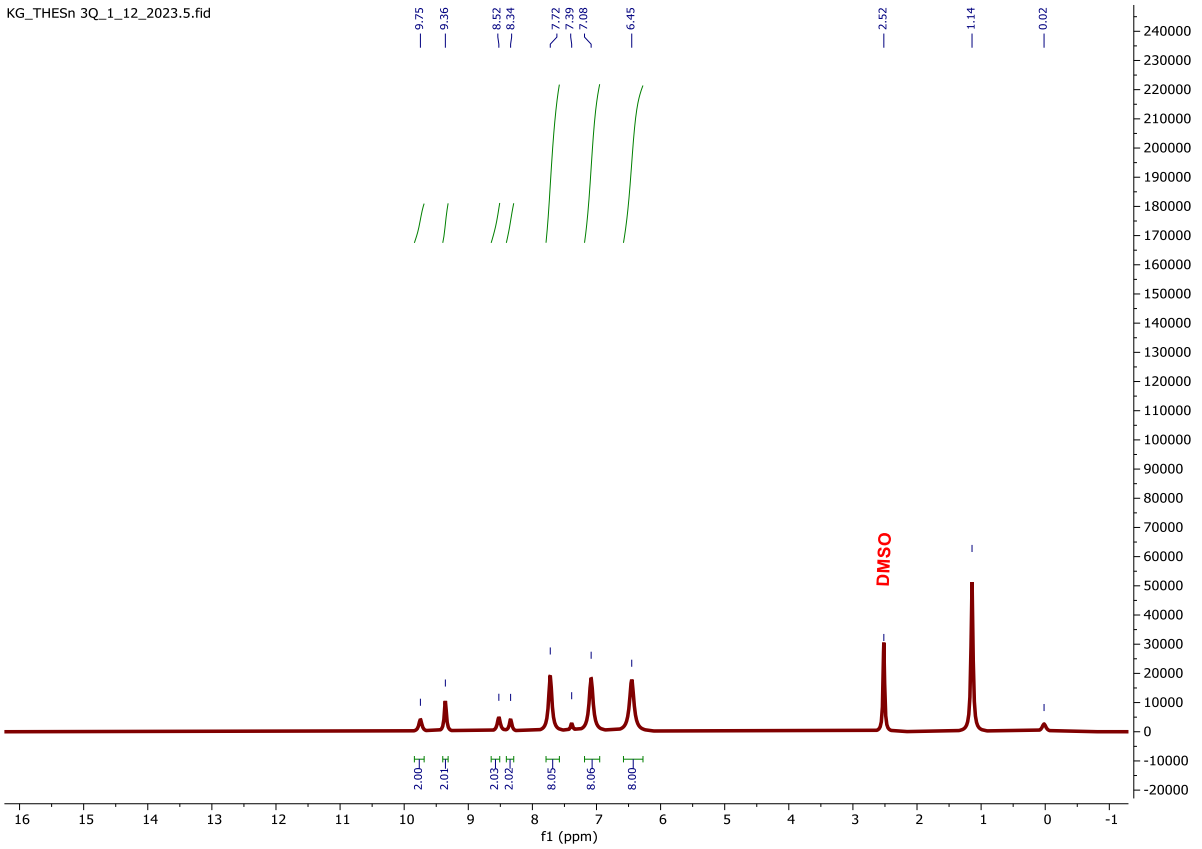

Figure 26: ^{1}H NMR spectrum of metalated **Sn3QP** in DMSO-d_6.

.

For **Sn3QP**, ^{1}H NMR peaks for the anticipated thirty-two protons are observed in the aromatic region (**Figure 26**).

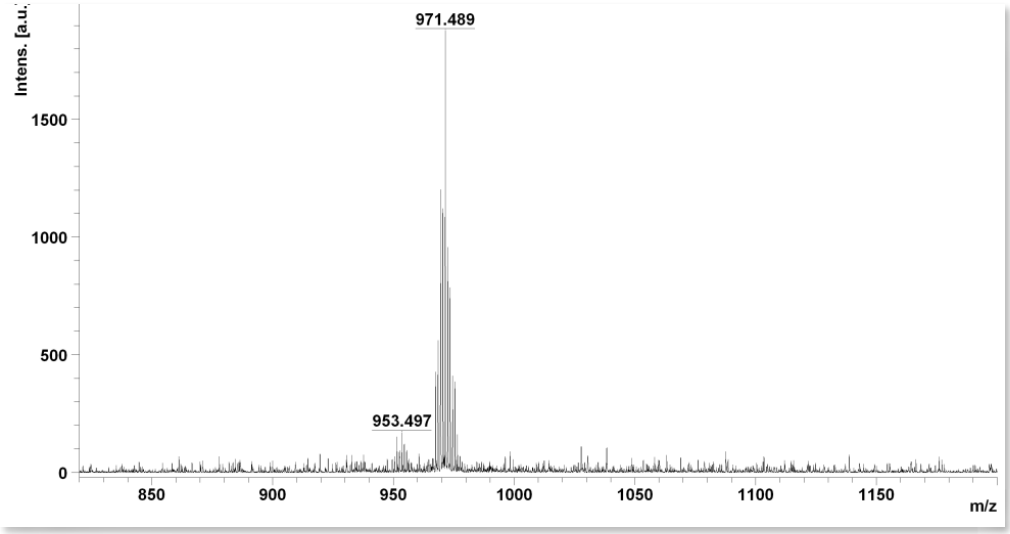

Figure 27: Mass spectral data for **Sn3QP**.

The MALDI-TOF MS peak obtained at 971.49 m/z (**Figure 27**) is consistent with an $[M-Cl]^{+}$ peak. The characterisation data for **Sn4QP** were broadly similar.

Quaternised porphyrins

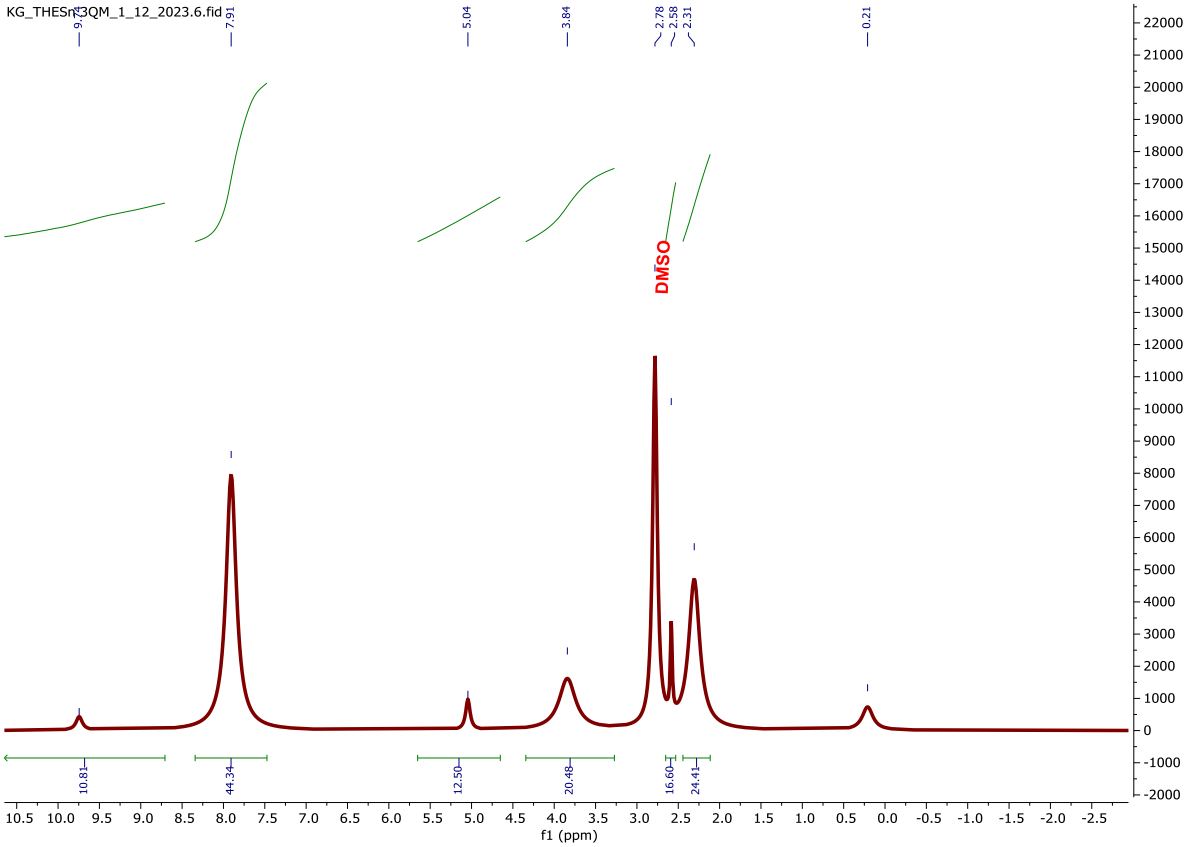

Figure 28: ^{1}H NMR spectrum of **Sn3M** in D_2O + DMSO-d_6.

The introduction of the TPP^{+} moiety induced aggregation because of the bulky attachment. Additional peaks corresponding to the TPP+ moiety were clearly observed in the ^{1}H NMR spectrum (**Figure 28**), providing direct spectroscopic evidence that quaternisation had occurred and that the effect of this quaternisation could be studied in proof of principle terms in the context of the PDT and PACT activity studies.

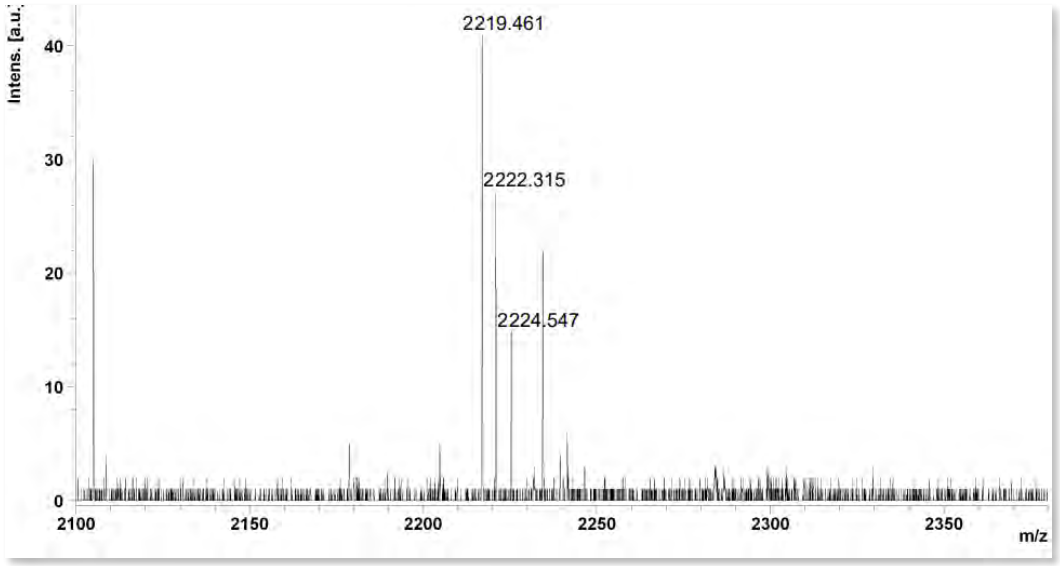

Figure 29: Mass spectral data for **Sn3M**.

The obtained MALDI-TOF MS parent peak was 2222.31 m/z (**Figure 29**), while the calculated molecular mass was 2222.66 amu. The analysis of the data for **Sn4M** was broadly similar.

Bacteriochlorins

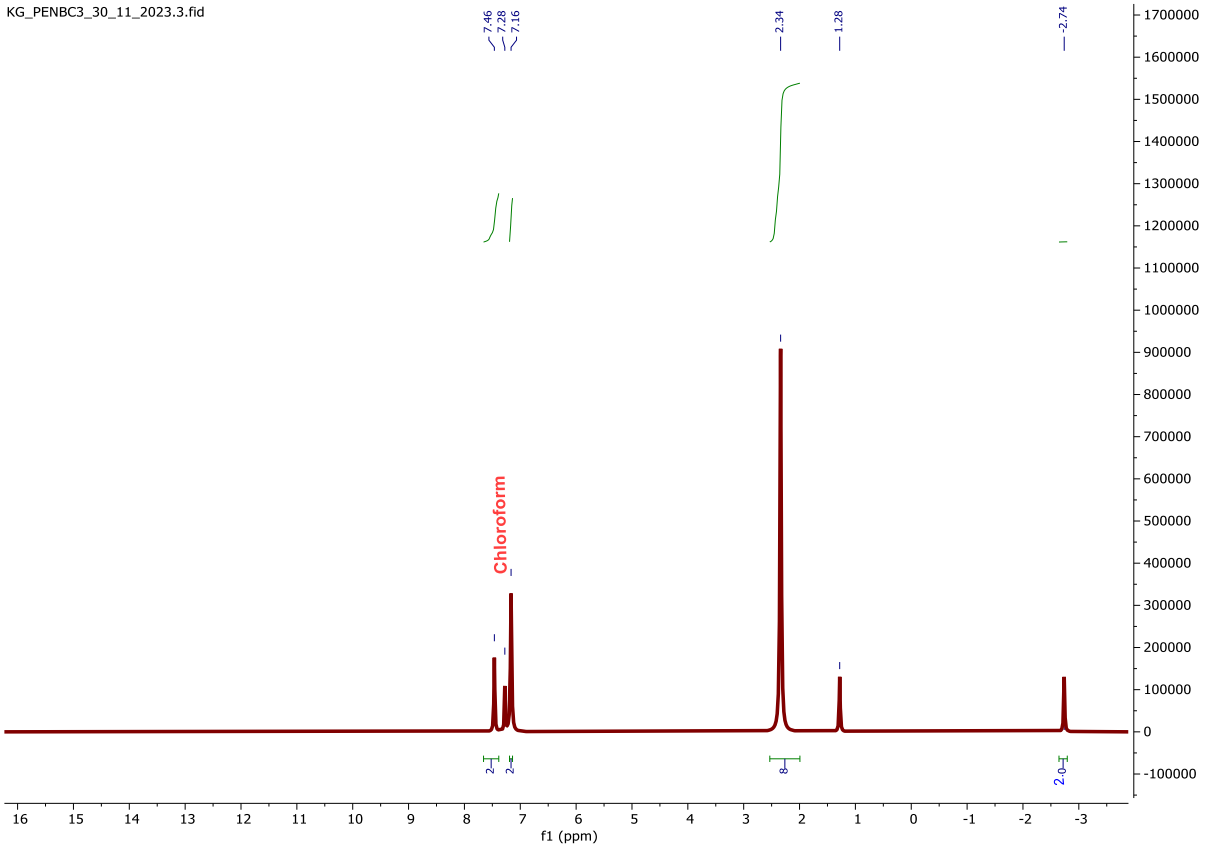

Figure 30: ^{1}H NMR spectrum of **PentaBChl** in $CDCl_3$.

PentaBChl exhibited the expected peak at −2.74 ppm for the two inner NH protons (**Figure 30**). Then, at *ca.* 2.34 ppm, the eight proton peak for the reduced pyrrolic bonds is observed, with peaks corresponding to four protons observed in the aromatic region along with the $CDCl_3$ solvent residual peak.

.

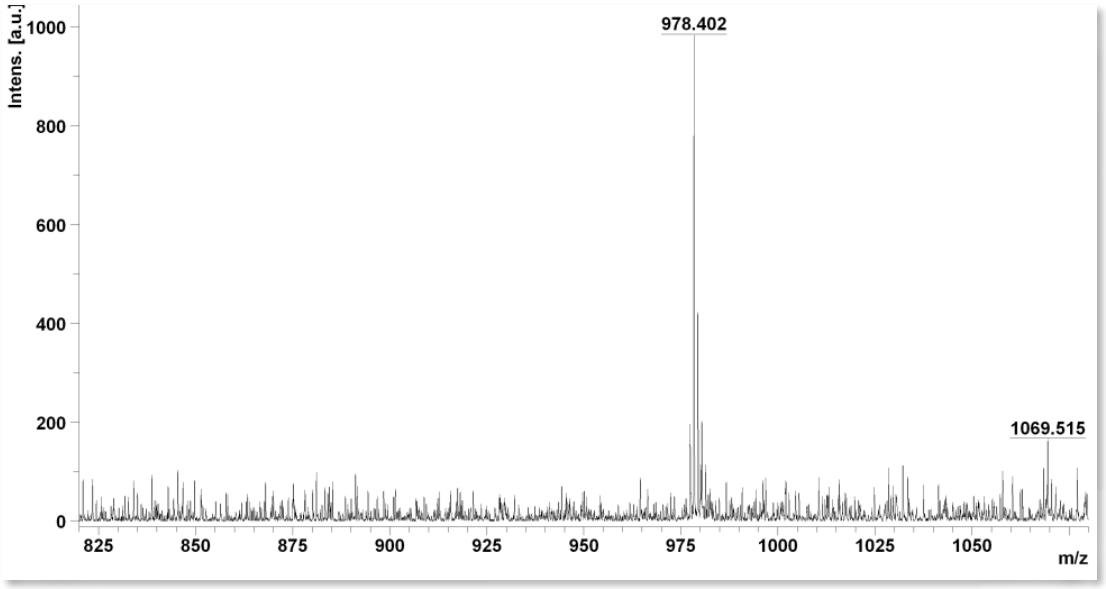

Figure 31: Mass spectral data for **PentaBChl**.

The calculated molecular mass was 978.09 amu, while the obtained MALDI-TOF MS parent peak was 978.40 m/z (**Figure 31**).

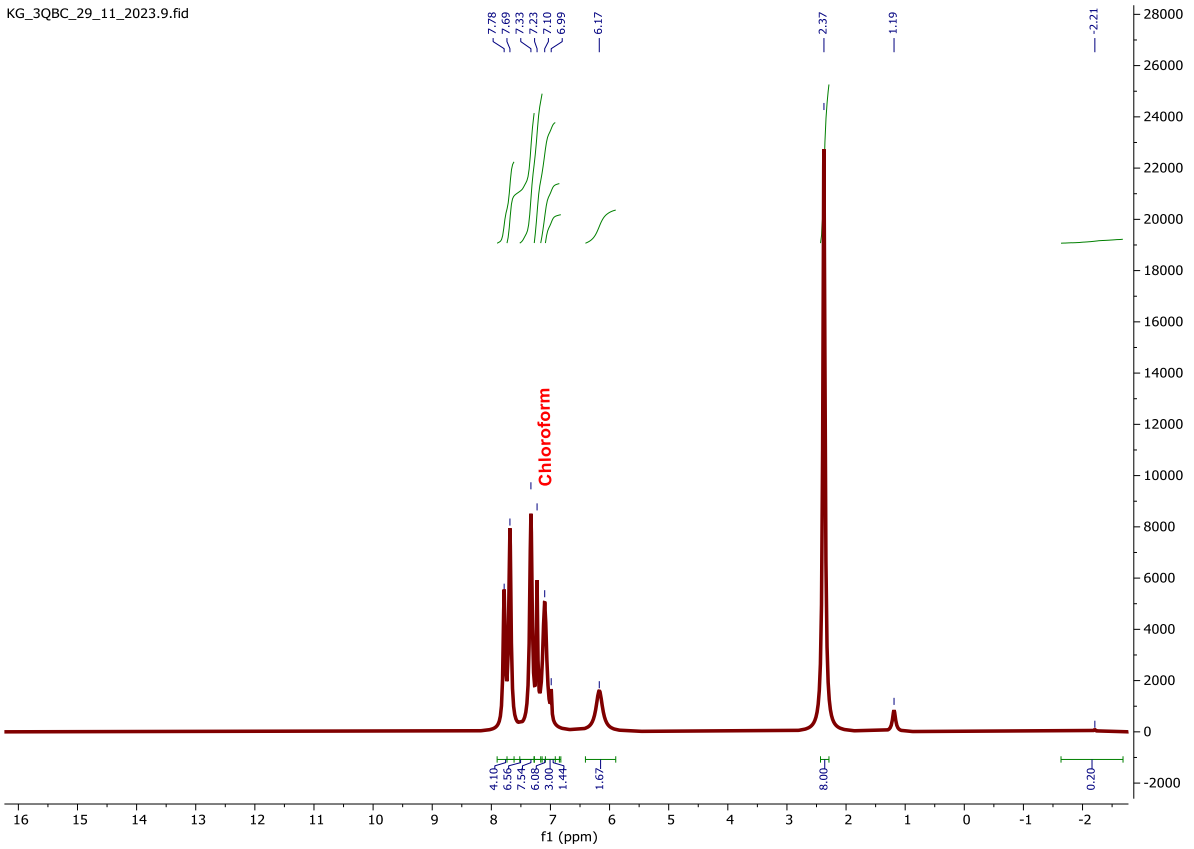

Figure 32: ^{1}H NMR spectrum of **3BChl** in $CDCl_3$.

The anticipated eight proton peak at *ca.* 2.50 ppm due to reduction of the porphyrin ligand was observed for **3BChl** (**Figure 32**), and the rest of the peaks provide the anticipated thirty-eight protons. It was difficult to integrate the inner NH peak possibly due to exchange with the $CDCl_3$ solvent.

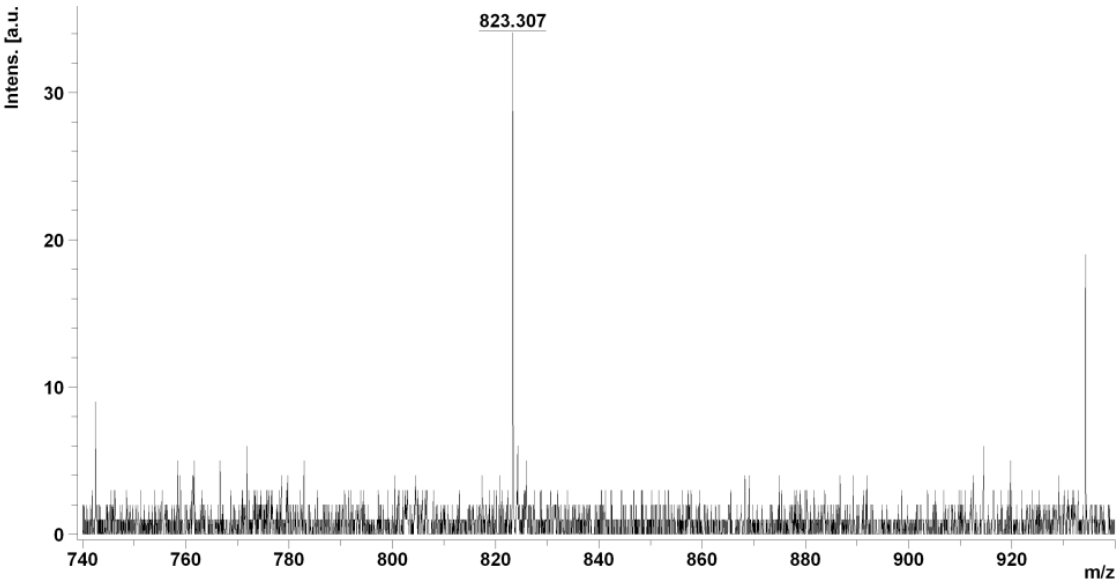

Figure 33: Mass spectral data for **3BChl**.

The calculated molecular mass was 822.32 amu, and the obtained obtained MALDI-TOF MS parent peak was 823.31 m/z, corresponding to a $[M+H]^+$ peak (**Figure 33**). The characterisation data for **4BChl** were broadly similar to those for **3BChl**.

Sn(IV) Bacheriochlorins

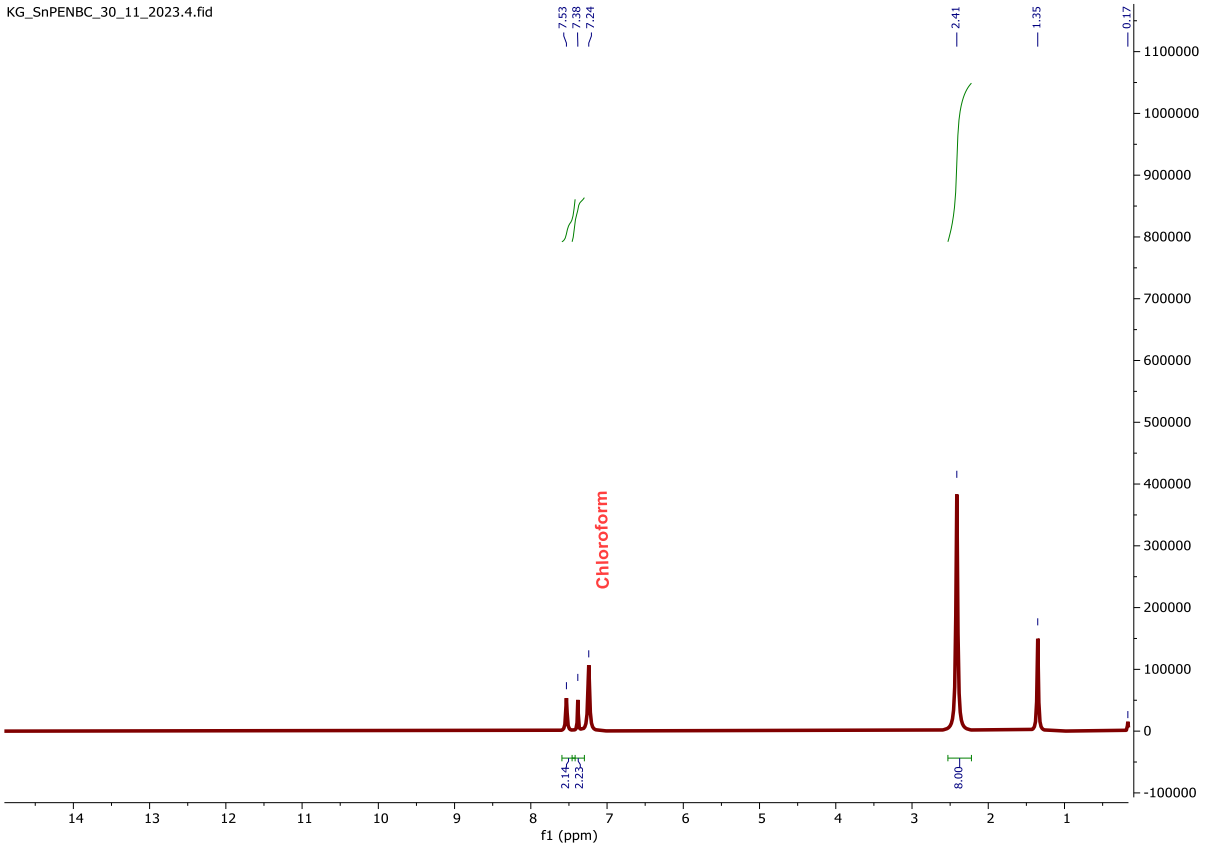

Figure 34: ^{1}H NMR spectrum of **SnPentaBChl** in $CDCl_3$.

The ^{1}H NMR spectrum of **SnPentaBChl** had no signal *ca.* -2.5 ppm. The peaks for the anticipated protons in the aromatic region were observed (**Figure 34**).

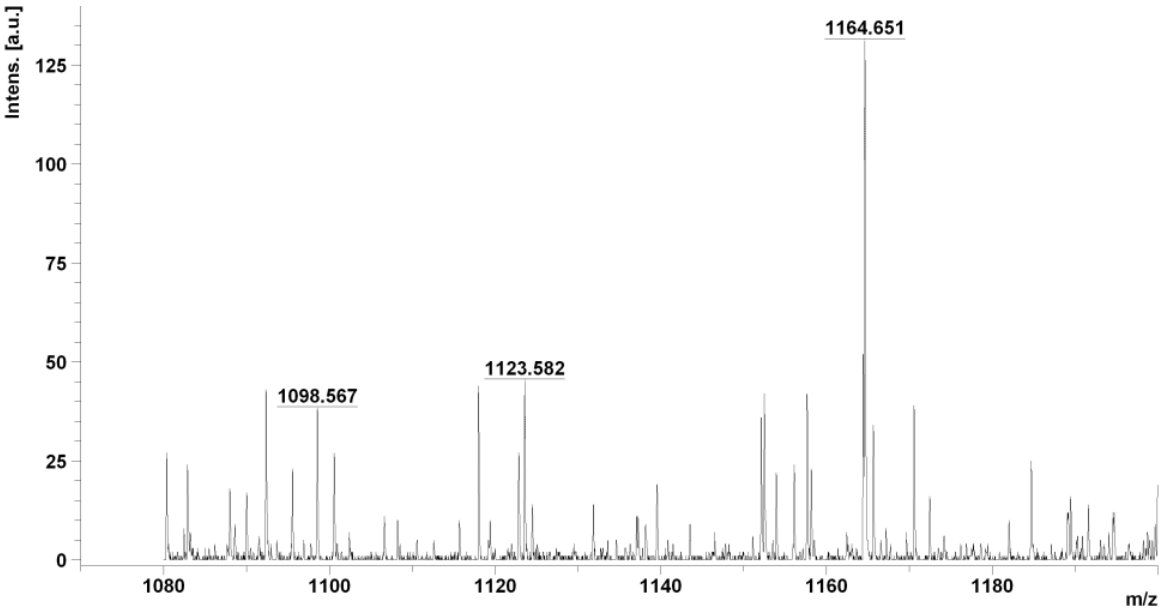

Figure 35: Mass spectral data for **SnPentaBChl**.

The calculated molecular mass was 1166.17 amu, while the obtained mass was 1164.65 m/z, corresponding to an $[M-H]^-$ peak.

Quaternised bacteriochlorins

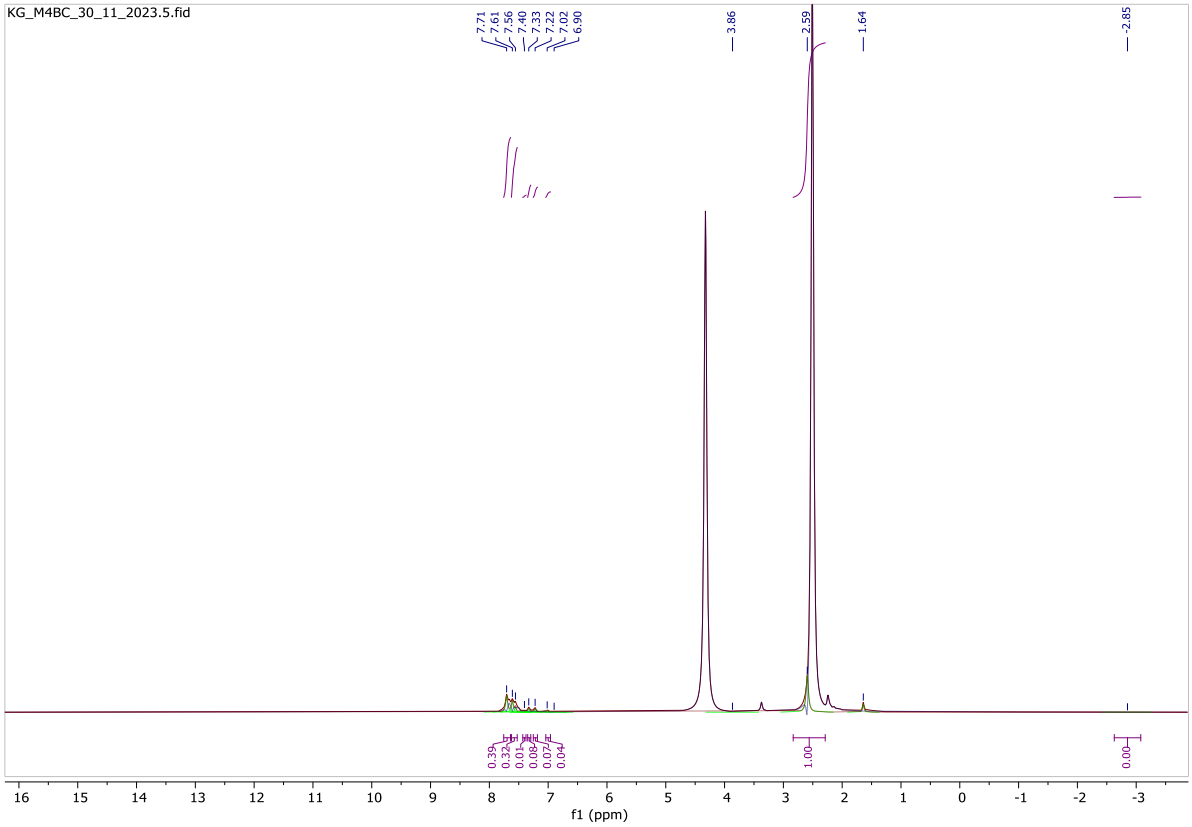

Figure 36: ^{1}H NMR spectrum of **M4BChl** in D_2O.

It was particularly difficult to obtain strong ^{1}H NMR peaks for the quaternised BChls due to solubility issues (**Figure 36**). However, additional peaks were clearly observed corresponding to the TPP^{+} moiety, providing direct spectroscopic evidence that quaternisation had occurred and that the effect of this quaternisation could be studied in proof of principle terms in the context of the PDT and PACT activity studies.

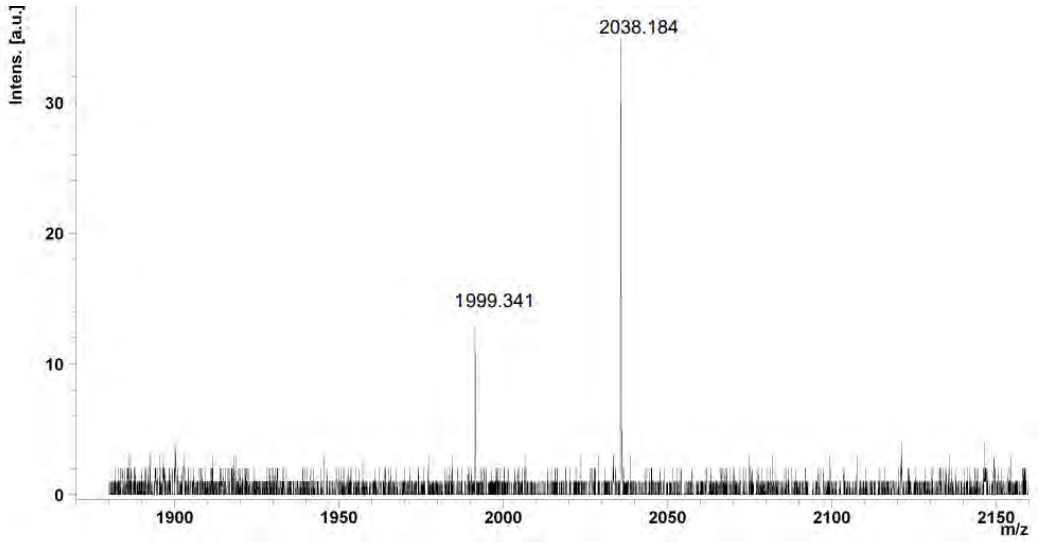

Figure 37: Mass spectral data for **M4BChl**.

The parent peak obtained by MALDI-TOF MS (**Figure 37**) was 2038.18 m/z relative to the calculated value of 2038.87 amu. Broadly similar characterisation data was obtained for **M4BChl**.

Photophysicochemical methods

3-Quinoline-substituted series

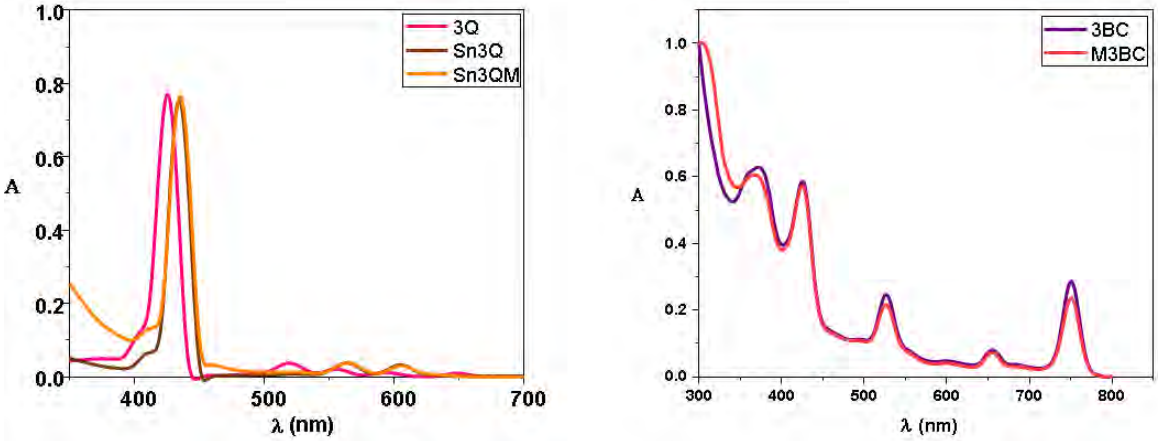

Figure 38: UV-visible absorption spectrum of 3-quinoline-substituted porphyrins (left) and BChls (right).

The photophysicochemical properties for the 3-quinoline substituted series of compounds are tabulated in **Table 1**. The anticipated Q and B bands were observed in the UV-visible absorption spectra (**Figure 38**).

Table 1: The photophysicochemical properties of **3QP**, **Sn3QP**, **Sn3M**, **3BChl** and **M3BChl** in DMSO.

	Abs (λ_{max})	**Emission (λ_{max})**	**Φ_F**	**Φ_Δ**	**τ_T (μs)**	**Photostability**
3QP	426, 518, 556, 594, 615	654,725	0.09	0.31	14	98%
Sn3QP	436, 564, 607	665	0.03	0.33	18	73%
Sn3QM	435, 564, 608	672	0.06	0.32	16	87%
3QBChl	428, 529, 658, 753	--	--	0.35	68	97%
M3QBChl	428, 529, 658, 753	--	--	0.02	59	98%

4-Quinoline-substituted series

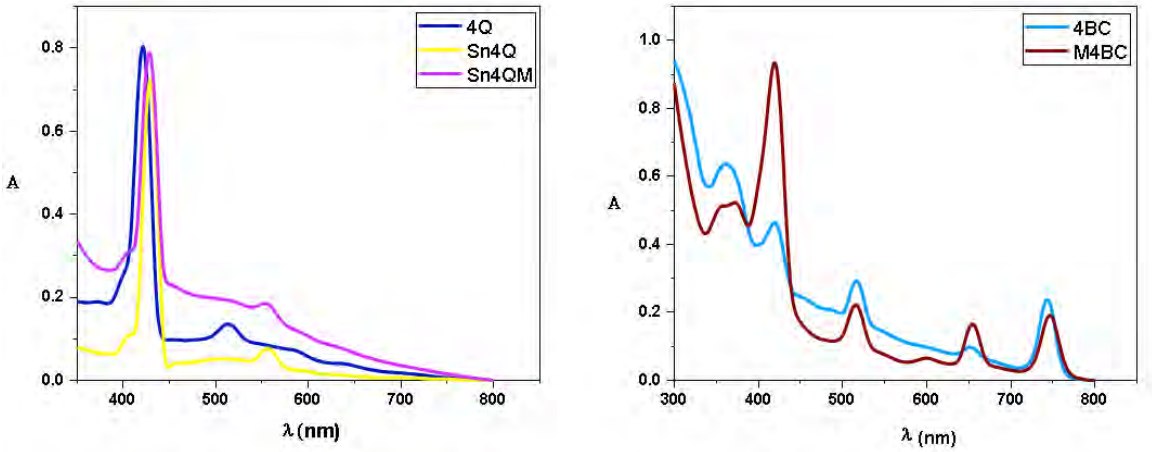

Figure 39: UV-visible absorption spectra of the 4-quinoline-substituted porphyrins (left) and BChls (right).

The photophysicochemical properties of the 4-quinoline substituted series of compounds are tabulated in **Table 2**. The anticipated Q and B bands were observed in the UV-visible absorption spectra (**Figure 39**). A typical data set for the Φ_Δ determinations is provided in **Figure 40**.

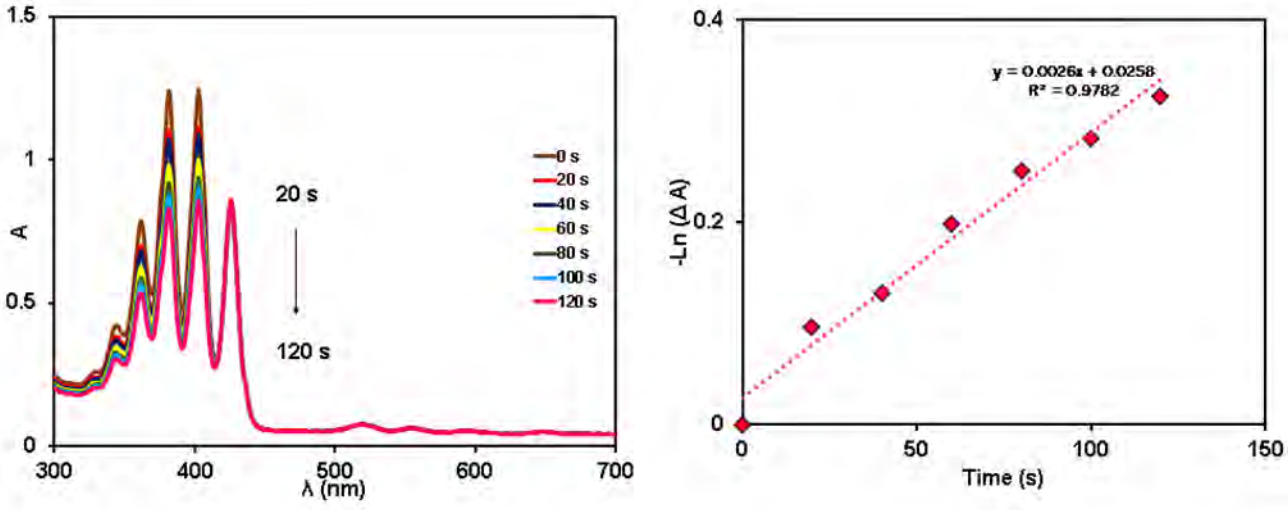

Figure 40: The comparative method for the Φ_Δ calculation of **3QP** providing spectra for the degradation of the DMA quencher DMA at 20 s time intervals (LEFT) and the associated linear best-fit plot (RIGHT).

Table 2: The photophysicochemical properties of **4QP**, **Sn4QP**, **Sn4M**, **4BChl** and **M4BChl** in DMSO.

	Abs (λ_{max})	Emission (λ_{max})	Φ_F	Φ_Δ	τ_T (μs)	Photostability
4QP	419, 515, 586	712	0.04	0.01	123	97%
Sn4QP	432, 558, 626	655	0.03	0.30	30	92%
Sn4QM	431, 556	--	0.01	0.17	62	97%
4QBChl	422, 521, 656, 747	--	--	0.53	207	85%
M4QBChl	419, 515, 600, 656, 748	--	--	0.80	131	99%

Pentafluorophenyl-substituted series

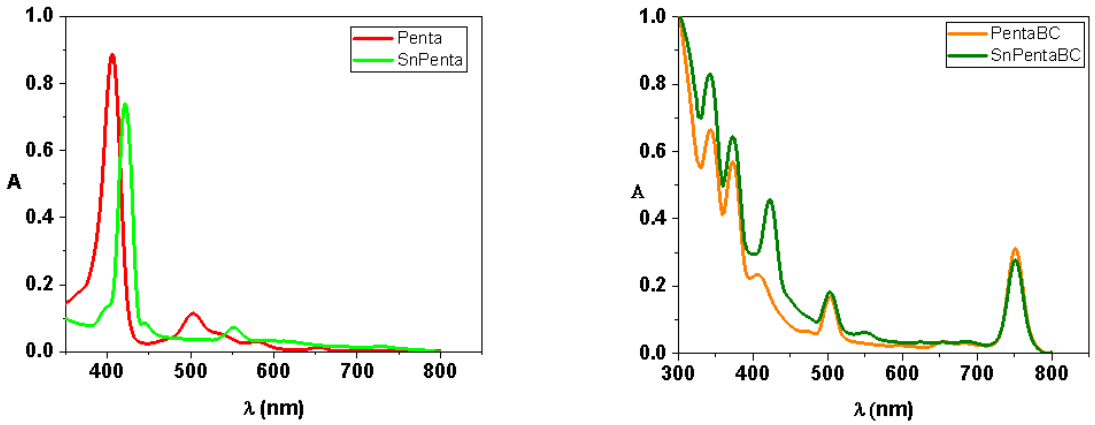

Figure 41: UV-visible absorption spectra of the free base pentafluorophenyl porphyrins (left) and the analogous BChls (right).

The photophysicochemical properties of the 4-quinoline substituted series of compounds are tabulated in **Table 3**. The anticipated Q and B bands were observed in the UV-visible absorption spectra (**Figure 41**). A typical data set for the τ_T analyses is provided in **Figure 42**.

Table 3: The photophysicochemical properties of **PentaP**, **SnPentaP**, **PentaBChl** and **SnPentaBChl** in DMSO.

	Abs (λ_{max})	**Emission (λ_{max})**	**Φ_F**	**Φ_Δ**	**τ_T (µs)**	**Photostability**
PentaP	406, 503, 584, 654	703	0.06	0.37	39	98%
SnPentaP	422, 553	666	< 0.01	0.79	26	99%
PentaBChl	345, 375, 410, 508, 657, 687, 753	--	--	0.21	74	98%
SnPentaBChl	341, 374, 424, 503, 553, 687, 749	--	--	0.61	25	98%

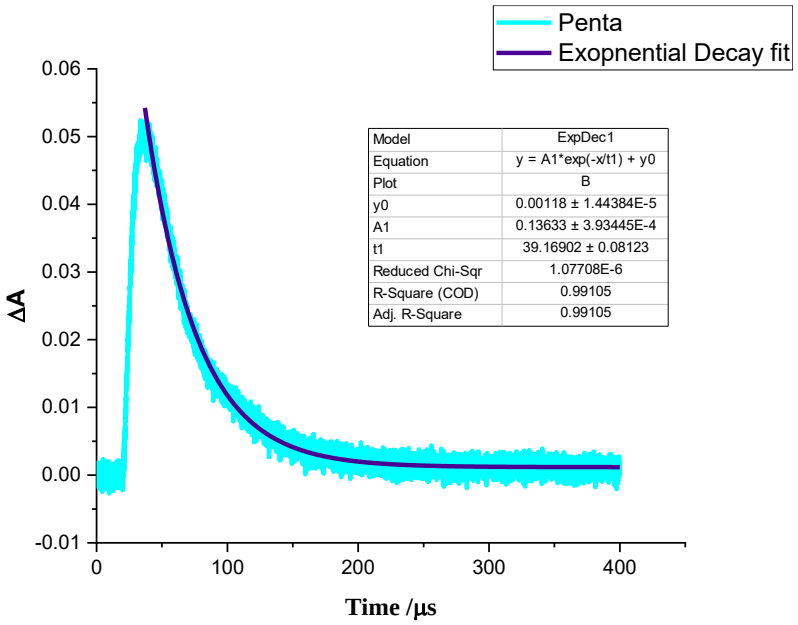

Figure 42: Triplet exponential decay of pentafluorophenyl porphyrin in DMSO under an N_2 atmosphere.

Log ε summary.

When molar extinction coefficients were calculated (**Figure 43** and **Table 4**) it became clear that there was a significant intensification of the Q bands of the BChls. The reasons for this will be explored in the Molecular Modelling chapter.

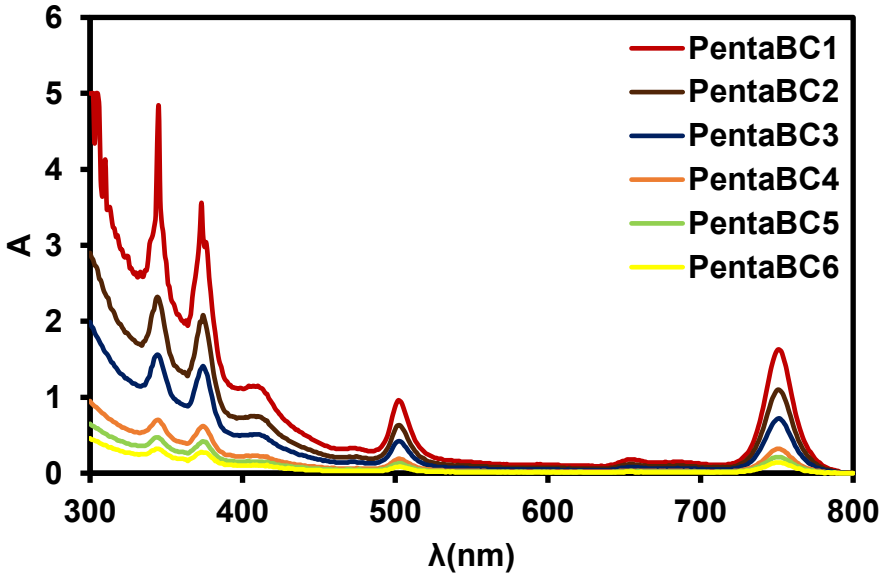

Figure 43: PentaBChl log ε serial dilutions in DMSO.

Table 4: Log ε values of the porphyrinoids at the various band maxima.

Compound	λ, nm(Log ε)
3QP	426(**5.01**) 518(**3.62**) 556(**3.40**) 594(**2.98**) 607(**2.98**)
Sn3QP	436(**5.12**) 564(**3.73**) 607(**3.64**)
Sn3M	435(**5.46**) 564(**4.11**) 608(**4.03**)
3QBChl	428(**5.018**) 529(**462**) 658(**4.17**) 753(**4.66**)
M3QBChl	428(**5.41**) 529(**4.99**) 658(**4.55**) 753(**5.00**)
4QP	419(**5.03**) 515(**4.17**) 586(**3.88**)
Sn4QP	432(**5.16**) 558(**4.08**) 626(**3.60**)
Sn4M	431(**5.52**) 556(**4.80**)
4QBChl	422(**4.91**) 521(**4.73**) 656(**4.27**) 747(**4.64**)
M4QBChl	341(**5.36**) 374(**4.73**) 424(**4.21**) 503(**4.65**) 553(**4.64**) 687(**4.66**) 749(**4.64**)
PentaP	406(**5.15**) 503(**4.27**) 584(**3.85**) 654(**3.33**)
SnPentaP	422(**5.22**) 553(**4.10**)
PentaBChl	345(**5.16**) 375(**5.08**) 410(**4.61**) 508(**4.53**) 657(**3.76**) 753(**4.77**)
SnPentaBChl	341(**5.31**) 374(**5.23**) 424(**5.08**) 503(**4.69**) 553(**4.19**) 687(**3.87**) 749(**4.84**)

Conclusions

The photophysicochemical studies demonstrate that dyes studied are potentially suitable for singlet oxygen biomedical applications, since they have moderate to high

singlet oxygen quantum yields. With the exception of **Sn3Q**, the other compounds exhibited high photostability under the conditions used for the PDT and PACT activity studies. Generally, the BChls have higher triplet state lifetimes than the porphyrins **4QP**, an outlier with a lifetime of 123 μs, while in contrast, the lifetime of **3QP** is 14 μs. Lifetimes on the microsecond timescale are crucial for effective photodynamic activity, since it results in more generation of singlet oxygen leading to more cell death.

4.PDT ACTIVITY STUDIES

4.1 PHOTODYNAMIC THERAPY

The following sigmoid graphs (**Figure 44**) depict the relationship/trend represented by the IC_{50} values (**Table 5**) that were observed when the MCF-7 cells were treated with the synthesised compounds over the 0 to 100 µM concentration range under unexcited (dark) and excited (light) photodynamic conditions.

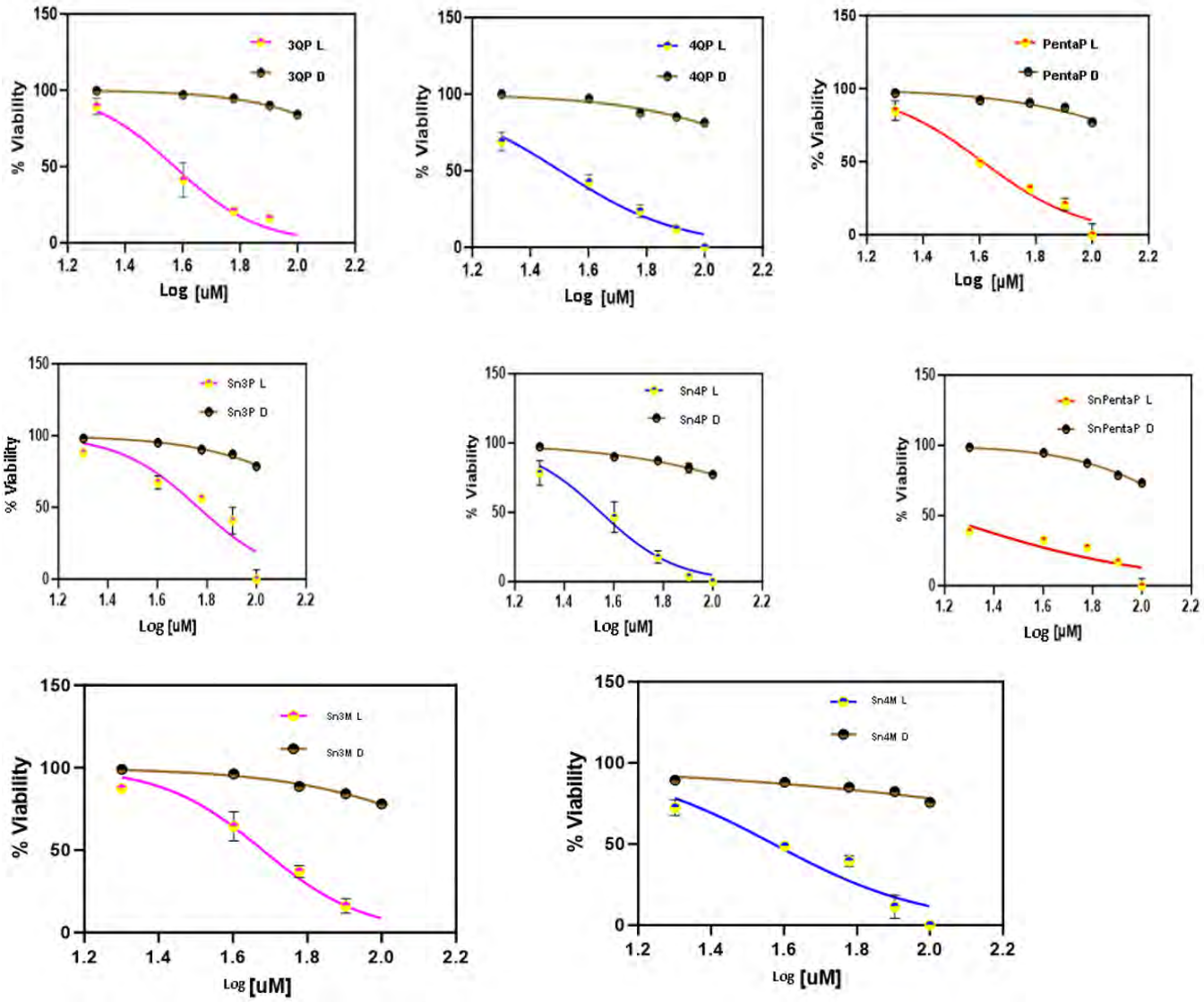

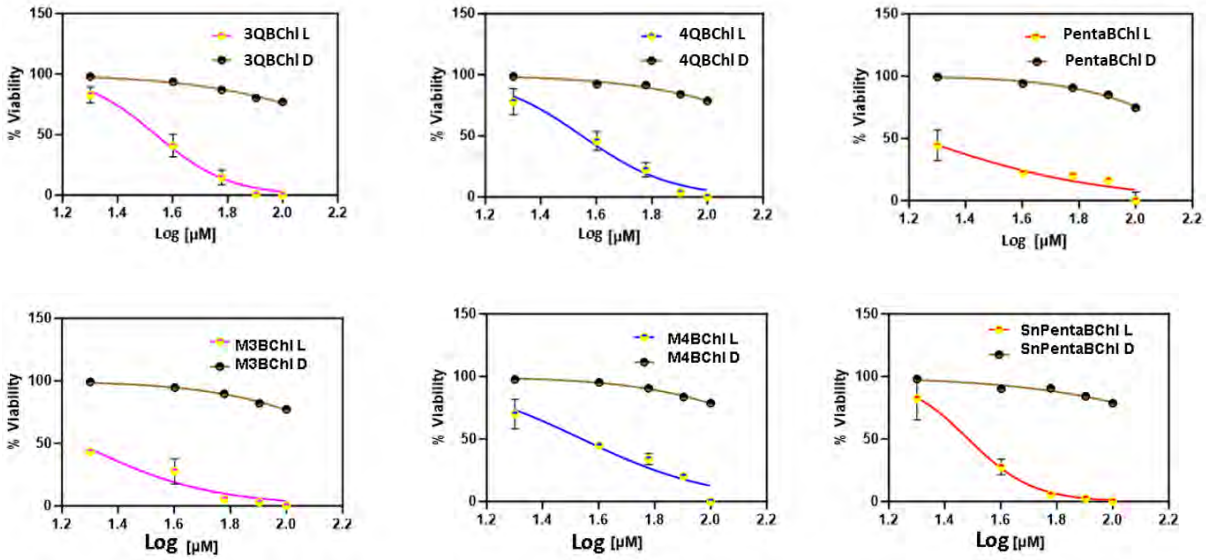

Figure 44: Sigmoid curves for the respective compounds showing the relative IC_{50} values in units of log [μM] during the dark toxicity (DARK) studies and when under illumination (LIGHT) with a Thorlabs LED.

The curves indicate that none of the dyes exhibit significant dark toxicity, **Table 5**. The lowest IC_{50} value for the PDT activity studies was **PentaBChl** with 7.59 μM followed by **SnPentaBChl** with 8.12 μM and **SnPentaP** with 11.2 μM. In the context of quinoline-substituted dyes, **3QBChl** had the lowest IC_{50} value of 12.3 μM, while **Sn4QP** had a value of 13.5 μM. It is evident from this that the pentafluorophenyl-substituted porphyrinoids were the most effective against MCF-7 cells and merit further in-depth follow-up studies. Interestingly, significant improvements were not observed in the IC_{50} values for **Sn3QM**, **Sn4QM**, **M3QBChl** and **M4QBChl** with mitochondria-targeting functionalisation relative to the corresponding **Sn3QP**, **Sn4QP**, **3QBChl** and **4QBChl** non-quaternised dyes. This suggests that this structural modification strategy needs to be carefully reassessed.

Table 5: IC_{50} values of the compounds against MCF-7 cells with and without light.

Compound	IC_{50} (μM) LIGHT	DARK	PI[a]
3QP	32.4	> 100	> 3.1
Sn3QP	58.9	> 100	> 1.7
Sn3M	22.9	> 100	> 4.4
3QBChl	12.3	> 100	> 8.1
M3QBChl	12.6	> 100	> 7.9
4QP	31.6	> 100	> 3.2
Sn4QP	13.5	> 100	> 7.4
Sn4M	38.0	> 100	> 2.6
4BChl	14.1	> 100	> 7.1
M4QBChl	18.6	> 100	> 5.4
PentaP	20.9	> 100	> 4.8
SnPentaP	11.2	> 100	> 8.9
PentaBChl	7.6	> 100	> 13.2
SnPentaBChl	8.1	> 100	> 12.4

a Phototoxicity ratio is a ratio of the IC50 values obtained during the light and dark studies.

Figures 45-48 illustrate the comparative differences in trends between the respective compounds and their varying concentrations against MCF-7 cells.

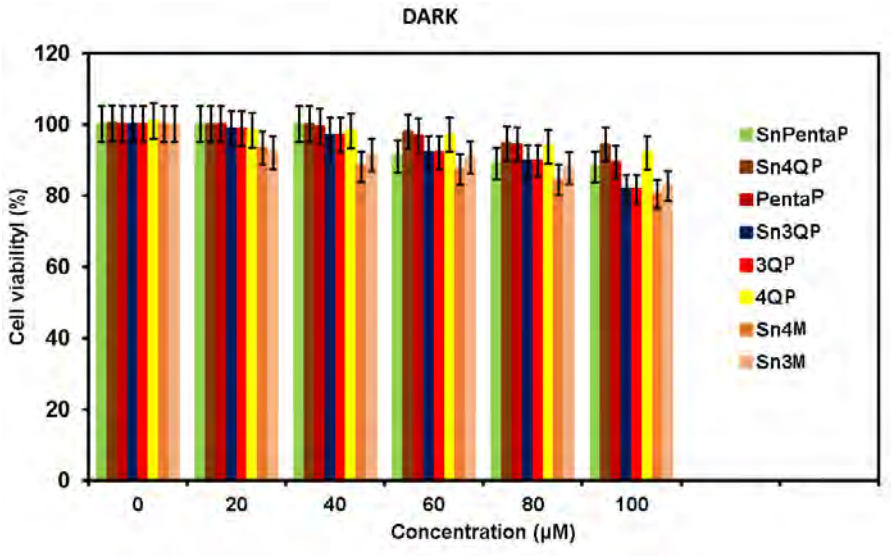

Figure 45: Free base, metalated and quaternised porphyrins against MCF-7 cells during dark toxicity studies.

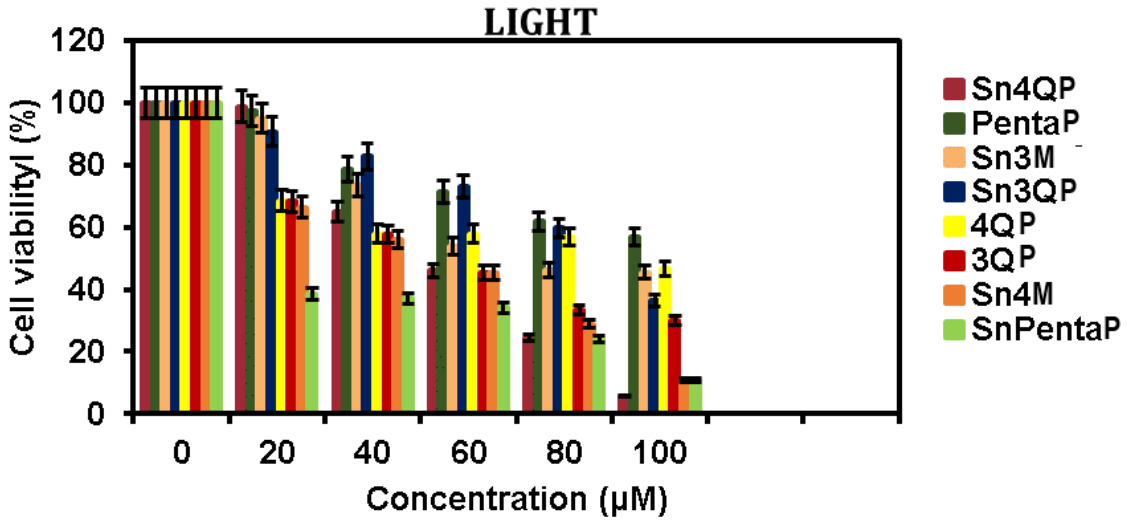

Figure 46: Free base, metalated and quaternised porphyrins against MCF-7 cells during PDT activity studies.

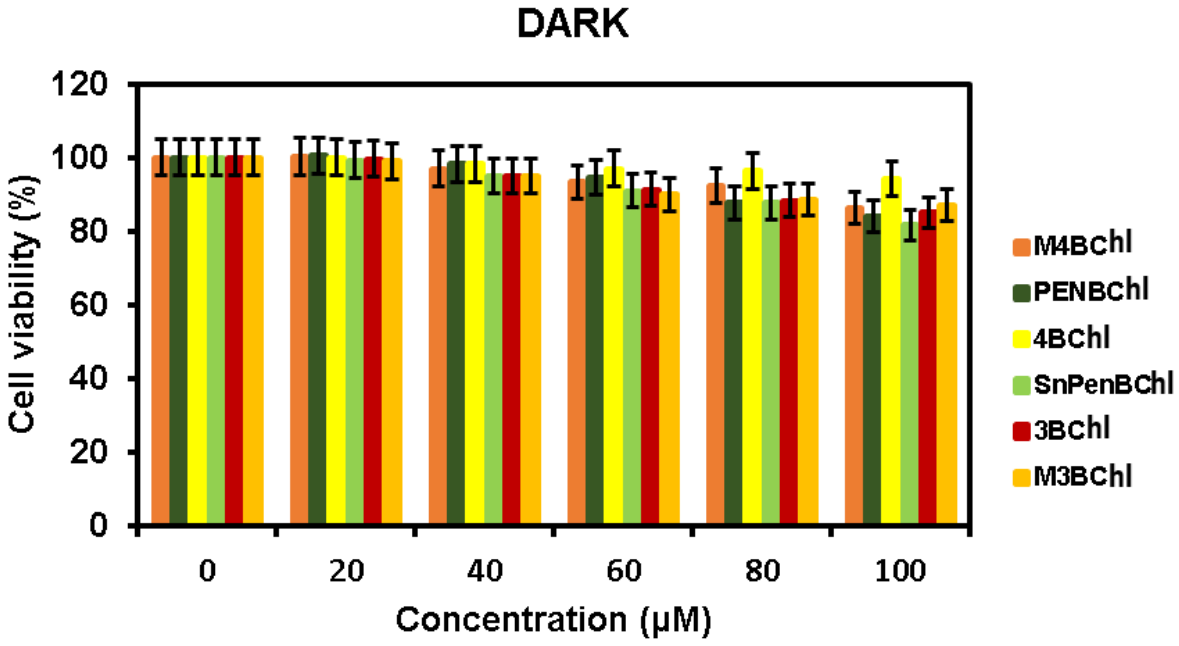

Figure 47: Free base, metalated and quaternised BChls against MCF-7 cells during dark toxicity studies.

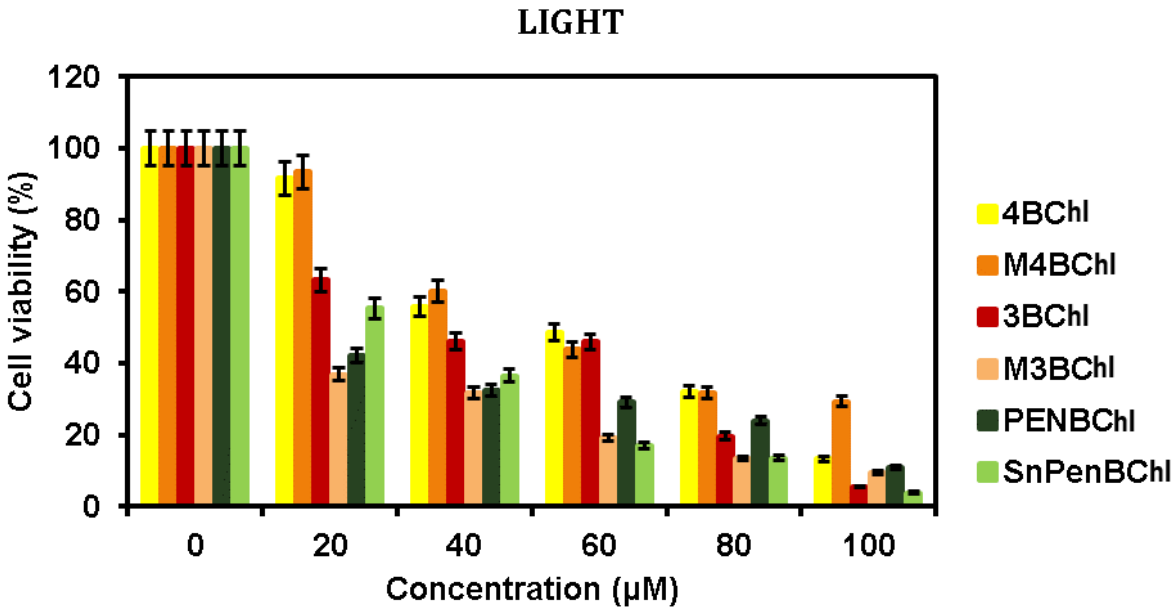

Figure 48: Free base, metalated and quaternised BChls against MCF-7 cells during PDT activity studies.

The IC_{50} values in **Table 5** provide the half-maximal inhibitory concentrations. Lower IC_{50} values demonstrate that the dye is more effective from a PDT activity standpoint. The general trend observed is a steady decrease in the IC_{50} value as the porphyrins are metalated and reduced to form BChls, with the lowest value being 7.59 μM of the **PentaBChl** and the highest being 58.9 μM for the **Sn3QP** porphyrin. **Figures 45-48** show the detailed cell death response against the different compound concentrations used, with the greatest cell death observed at the highest concentration of 100 μM. The most effective porphyrin was **SnPentaP**, with an IC_{50} value of 11.2 μM, followed by **Sn4QP**, with a value of 13.5 μM. All the other porphyrins studied had values > 20 μM. As for the BChls, **PentaBChl** and **SnPentaBChl** were found to be the most effective, with values of 7.6 and 8.1 μM, while **M3QBChl** and **M4QBChl** had higher IC_{50} values than **M3QBChl** and **M4QBChl**. **Figure 49** provides microscopy images of the cells before and after light treatment.

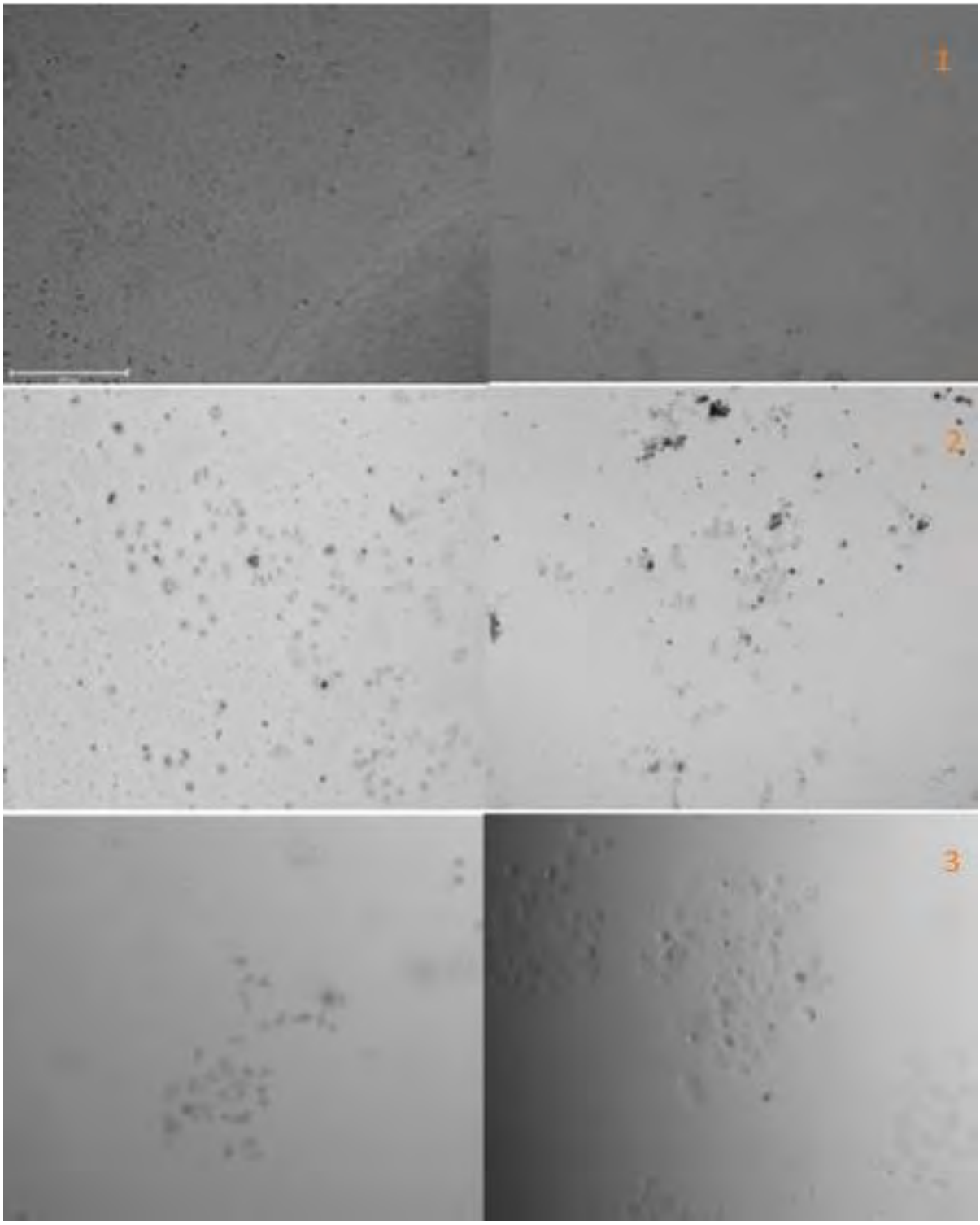

Figure 49: Microscope images of MCF-7 cells before and after their treatment. From left to right, 1: depicts the confluent and control cells, respectively; 2: depicts the light studies **3QP** and **PentaP** treatment cells; 3: depicts the **SnPentaBChl** and **M3QBChl** light treatments.

Concluding remarks

The IC_{50} values demonstrate that the compounds were significantly more active under light conditions than during the dark toxicity studies, with the BChls performing better than the corresponding porphyrins. The activities of the quaternised porphyrins and BChl's activities were inconsistent. Due to time constraints, uptake studies could not be performed. This will be done in future and will provide additional insights about the suitability of the dyes for PDT.

5.PACT ACTIVITY STUDIES

PACT studies against *S. aureus*

The first type of bacteria to be studied was *S. aureus* (**Figures 50-59**). A concentration of 80 μM was selected for study, based on concentration studies. The Log_{10} CFU/mL values are tabulated in **Table 6**. In the context of the free base porphyrins, **PentaP** has the highest Log_{10} CFU/mL value of 2.22 (**Figure 51**) followed by **3QP** and **4QP** with values of 1.38 and 0.92. Typically, a value > 3 is necessary for a dye to be regarded as an effective antibacterial agent. In a similar manner, **SnPentaP** with a Log_{10} reduction of 2.05 is more effective than **Sn3QP** and **Sn4QP** (**Figure 53**). A slightly higher Log_{10} reduction of 2.07 was induced by **Sn4M** relative to the value of 1.87 for **Sn3M** (**Figure 55**). In a similar manner to what was observed for the free base porphyrins, **PentaBChl** has a higher Log_{10} reduction value of 3.49 than the values of 2.89 and 2.28 for **3BChl** and **4QBChl** (**Figure 57**). The quaternised and Sn(IV) BChls were highly active with Log_{10} reduction values of 6.39 (**Figure 59**) and hence have the most potential as PS dyes in this context. Typical images from the bacterial colony counting process are provided in **Figure 60**.

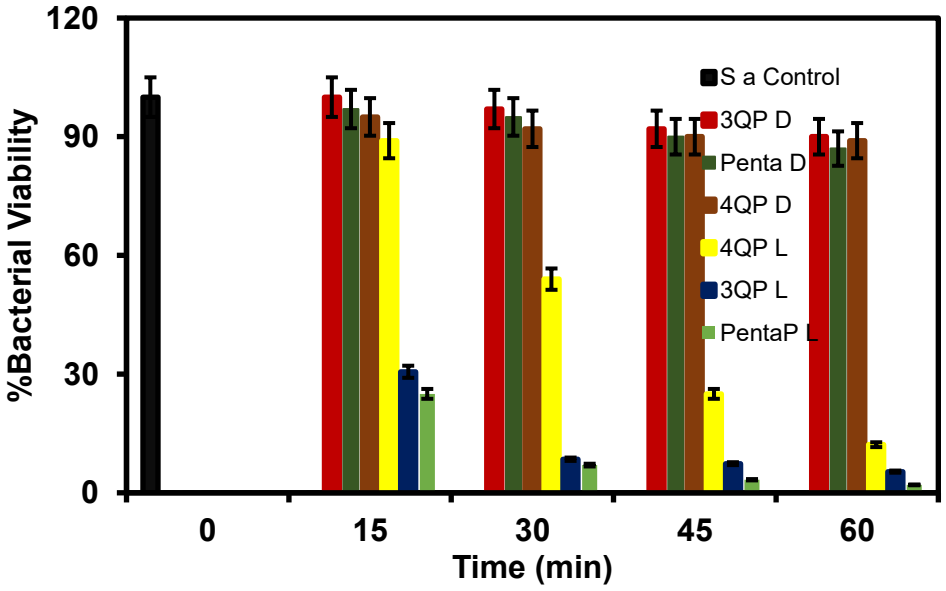

Figure 50: Bacterial viability data for free base porphyrins against *S. aureus*. D and L refer to the dark and light studies, respectively.

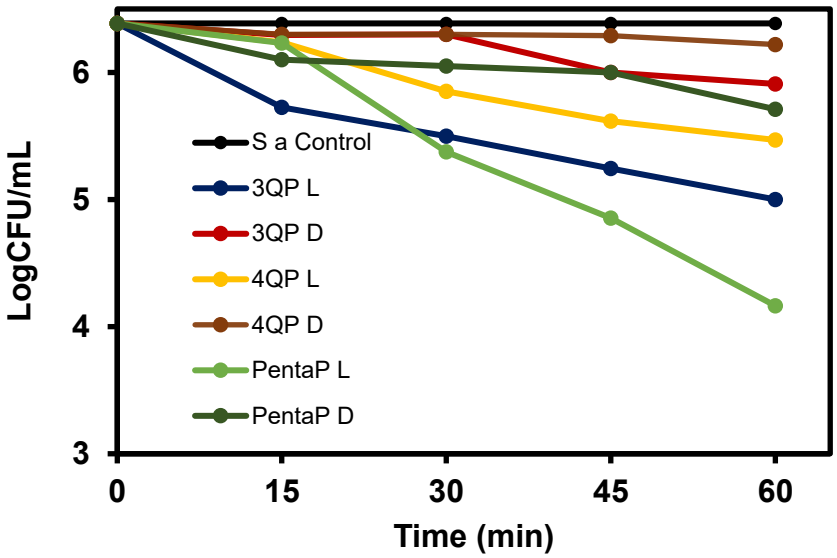

Figure 51: Log_{10} CFU/mL values for free base porphyrins against *S. aureus*. D and L refer to the dark and light studies, respectively.

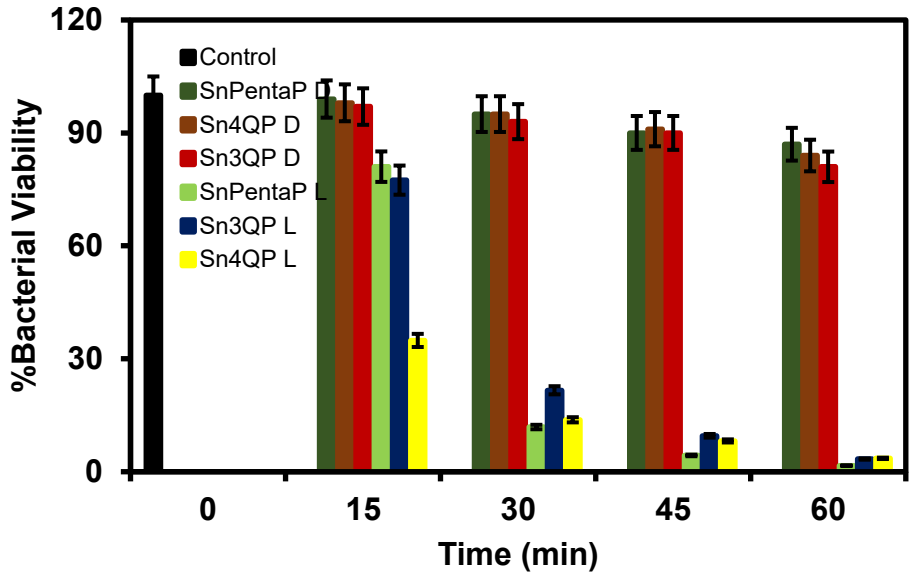

Figure 52: Bacterial viability data for metal porphyrins against *S. aureus*. D and L refer to the dark and light studies, respectively.

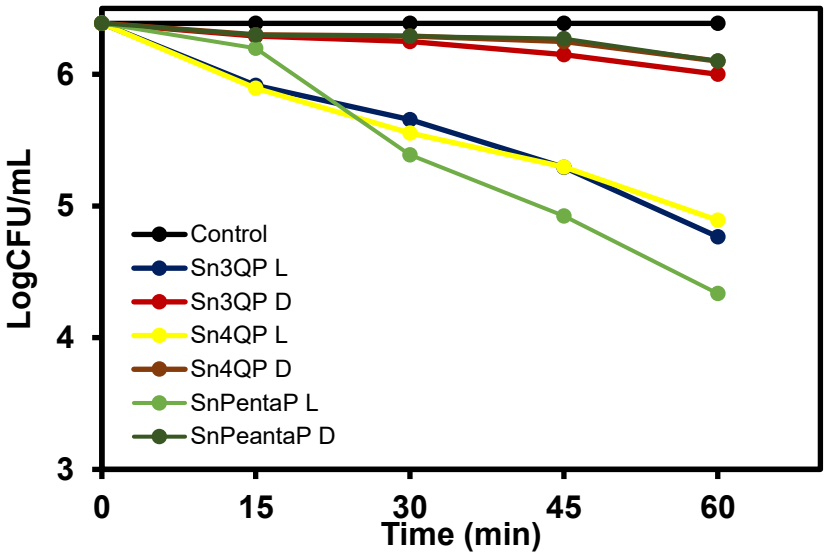

Figure 53: Log_{10} CFU/mL values for Sn(IV) porphyrins against *S. aureus*. D and L refer to the dark and light studies, respectively.

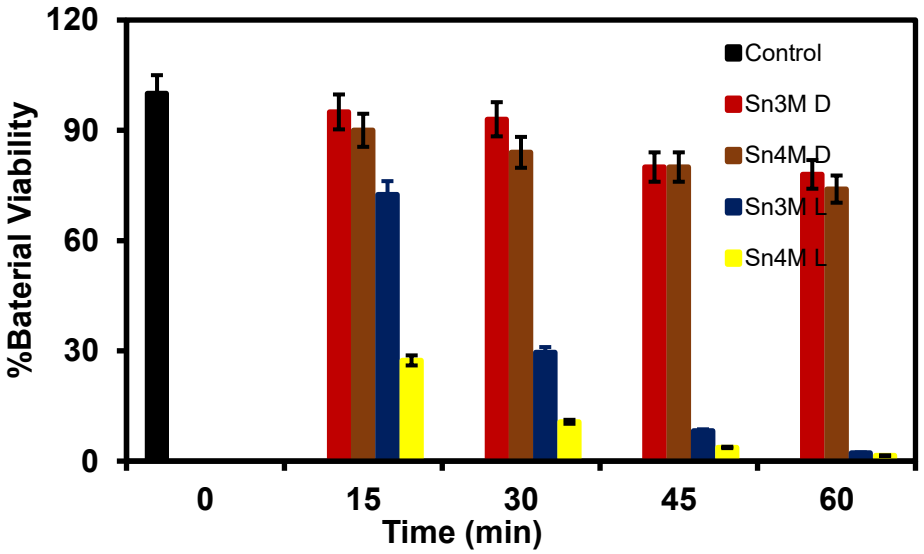

Figure 54: Bacterial viability data for quaternised porphyrins against *S. aureus*. D and L refer to the dark and light studies, respectively.

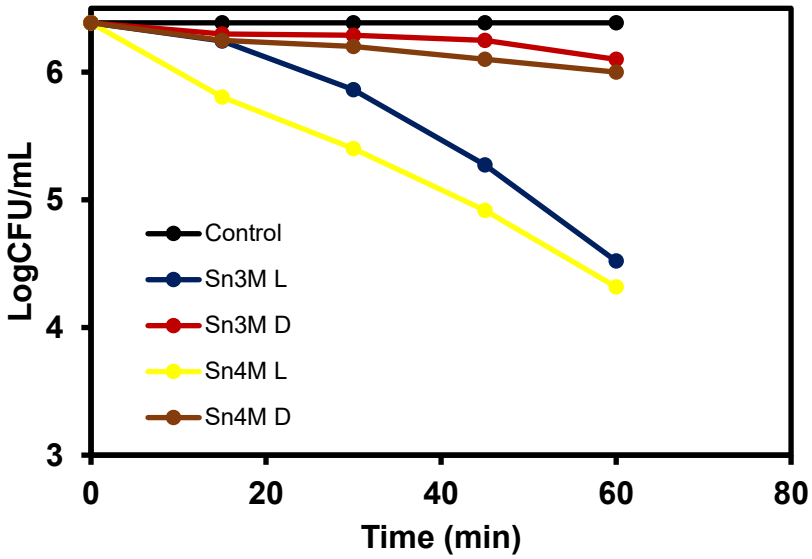

Figure 55: Log_{10} CFU/mL values for quaternised porphyrins against *S. aureus*. D and L refer to the dark and light studies, respectively.

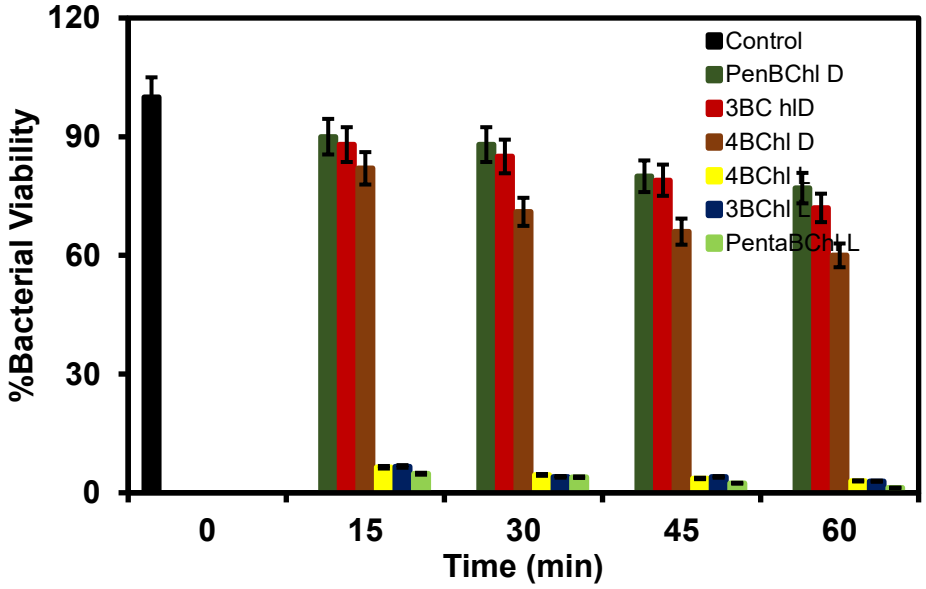

Figure 56: Bacterial viability data for free base BChls against *S. aureus*. D and L refer to the dark and light studies, respectively.

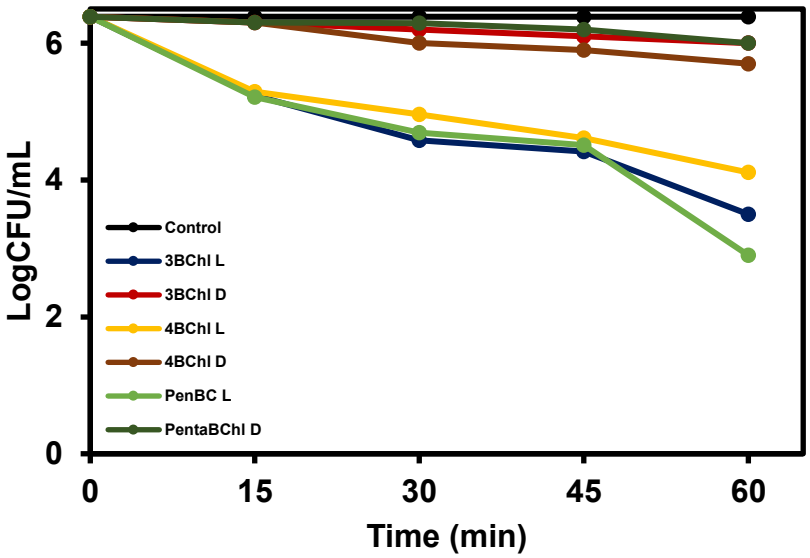

Figure 57: Log_{10} CFU/mL values for free base BChls against *S. aureus*. D and L refer to the dark and light studies, respectively.

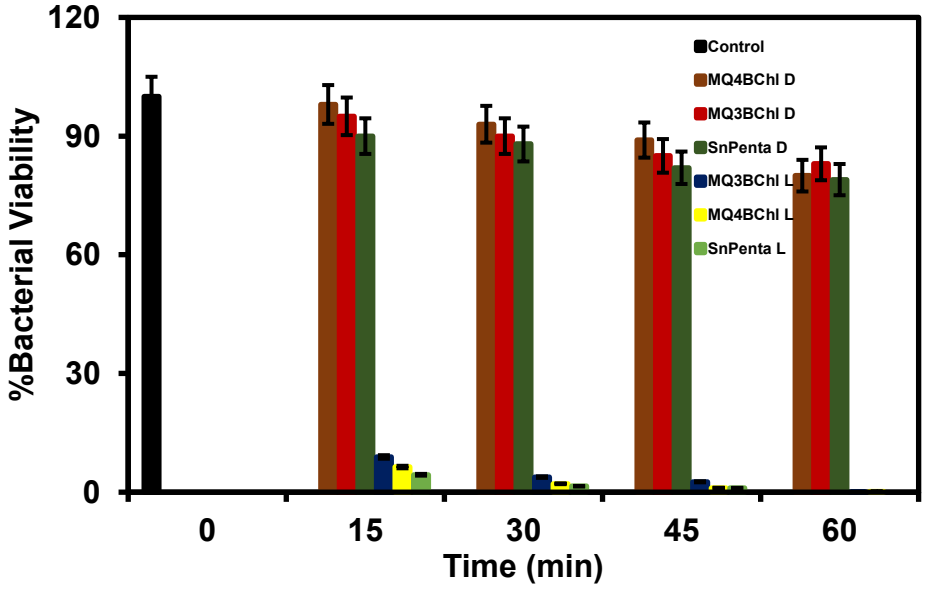

Figure 58: Bacterial viability data for Sn(IV) and quaternised BChls against *S. aureus*. D and L refer to the dark and light studies, respectively.

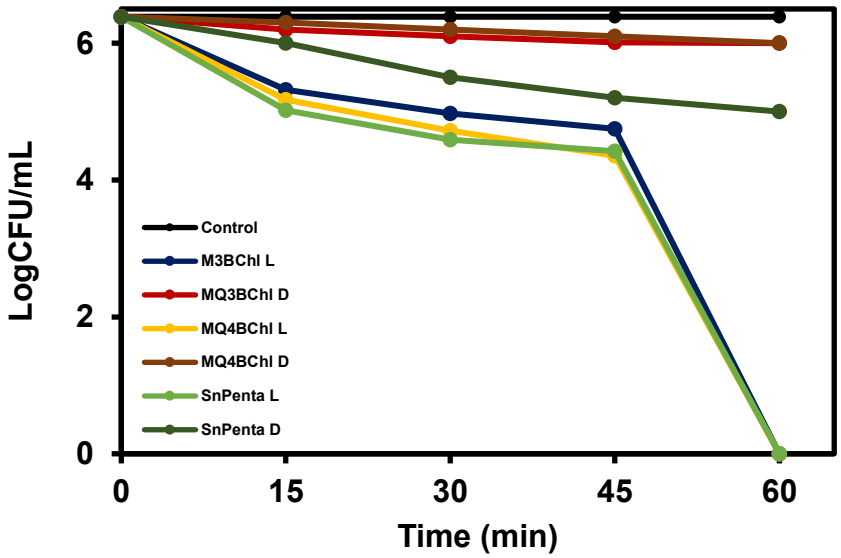

Figure 59: Log_{10} CFU/mL values for Sn(IV) and quaternised BChls against *S. aureus*. D and L refer to the dark and light studies, respectively.

Table 6: A summary of the log reduction values against *S. aureus.*

	S. aureus	
PS	**LIGHT**	**DARK**
3QP	1.38	0.47
Sn3QP	1.62	0.39
Sn3M	1.87	0.29
3QBChl	2.89	0.39
M3BChl	6.39 (@ 60 min)	0.39
4QP	0.92	0.17
Sn4QP	1.49	0.29
Sn4M	2.07	0.39
4QBChl	2.28	0.69
M4BChl	6.39 (@ 60 min)	0.39
PentaP	2.22	0.68
SnPentaP	2.05	0.29
PentaBChl	3.49	0.69
SnPentaBChl	6.39 (@ 60 min)	1.39

[a] The irradiation time at which full eradication of the bacteria is achieved is provided in parentheses where relevant.

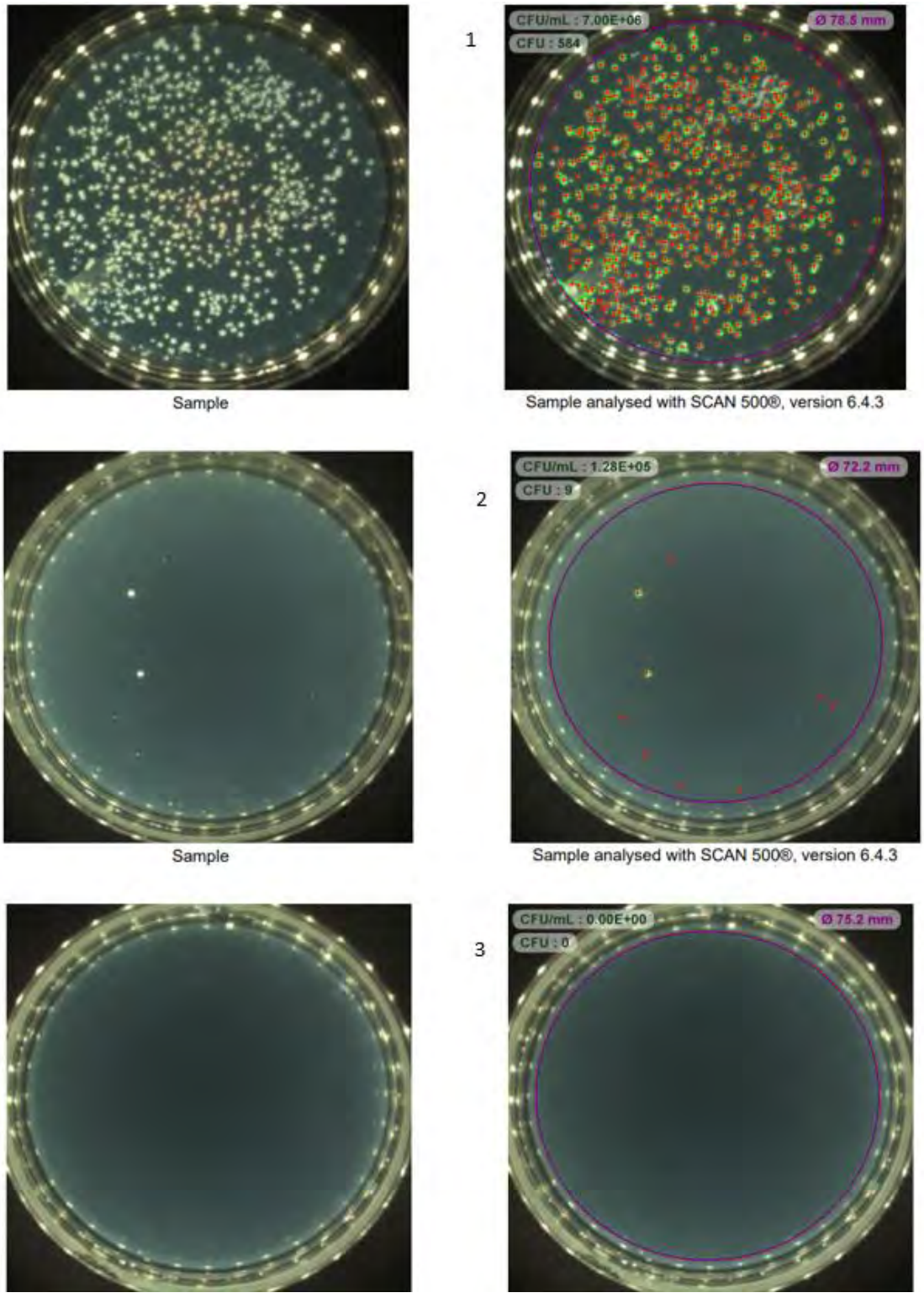

Figure 60: Images of the *S. aureus* and *E. coli* plates before and after their treatment. From left to right, 1 provides the *S. aureus* and *E. coli* controls, respectively, 2 provides the light treatments of **SnPentaBChl** and **M4BChl** at 45 min, and 3 provides the light treatments of **SnPentaBChl** and **M4BChl** at 60 min.

PACT studies against *E. coli*

The second bacteria to be studied was *E. coli* (**Figures 61-70**). A concentration of 80 μM was selected for study, based on concentration studies. The Log_{10} CFU/mL values are tabulated in **Table 7**. In the context of the free base porphyrins, **PentaP** has the highest Log_{10} CFU/mL value of 6.39 (**Figure 62**) followed by **4QP** and **3QP** with values of 1.75 and 1.39. In contrast, the Log_{10} reduction value of **SnPentaP** of 2.05 is comparable to the 1.94 and 2.06 values of **Sn3QP** and **Sn4QP** (**Figure 64**). A higher Log_{10} reduction of 6.39 was induced by **Sn4M** relative to the value of 1.97 for **Sn3M** (**Figure 66**). The free base, Sn(IV) and quaternised BChls all have Log_{10} reduction values of 6.39 (**Figures 68** and **70**) and hence merit further in-depth study in this context.

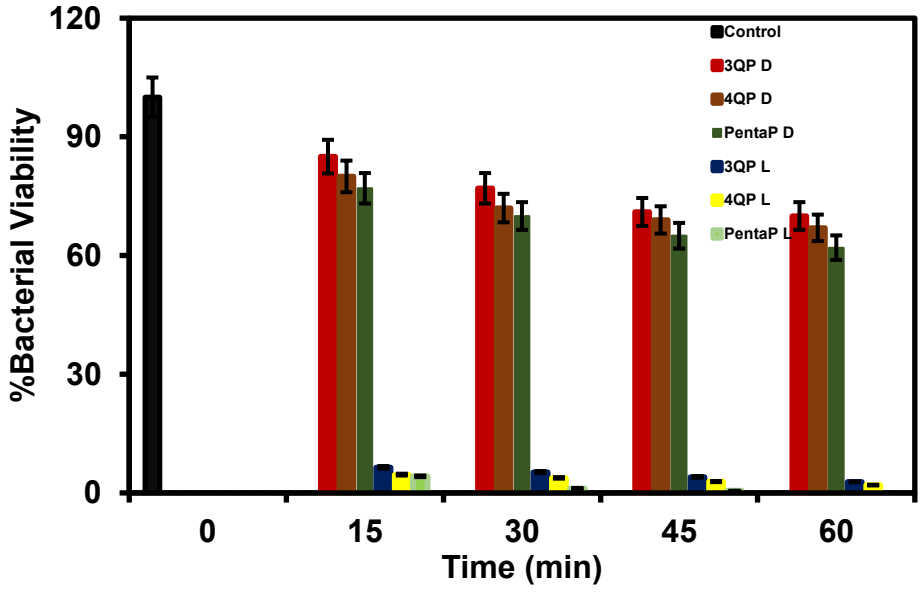

Figure 61: Bacterial viability data for free base porphyrins against *E. coli*. D and L refer to the dark and light studies, respectively.

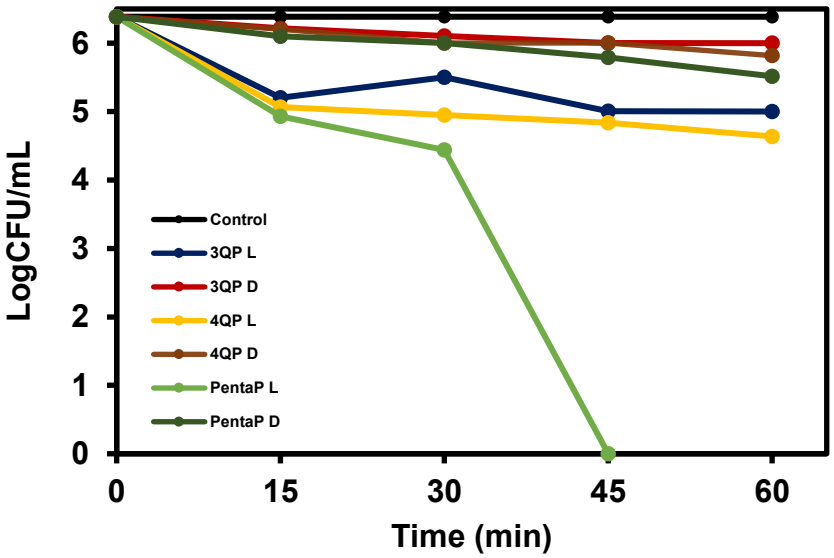

Figure 62: Log_{10} CFU/mL values for free base porphyrins against *E. coli*. D and L refer to the dark and light studies, respectively.

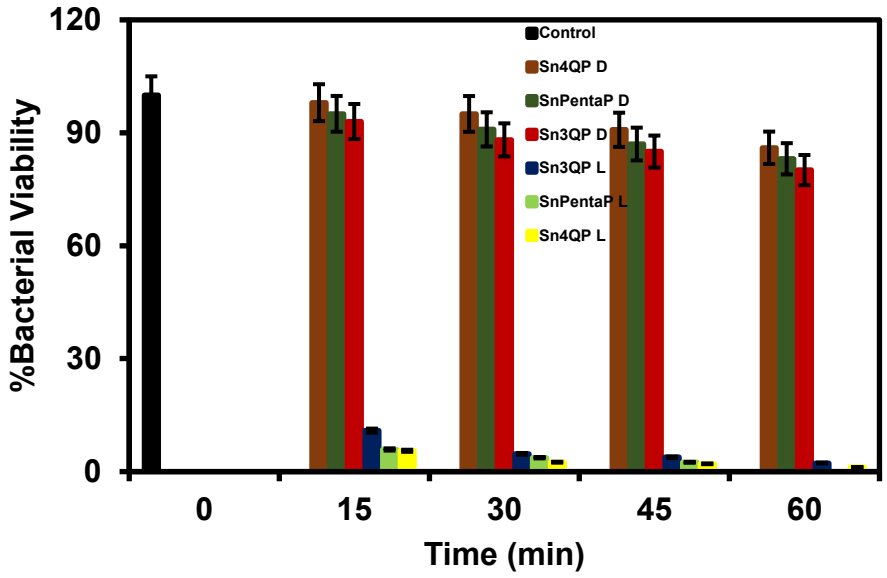

Figure 63: Bacterial viability data for Sn(IV) porphyrins against *E. coli*. D and L refer to the dark and light studies, respectively.

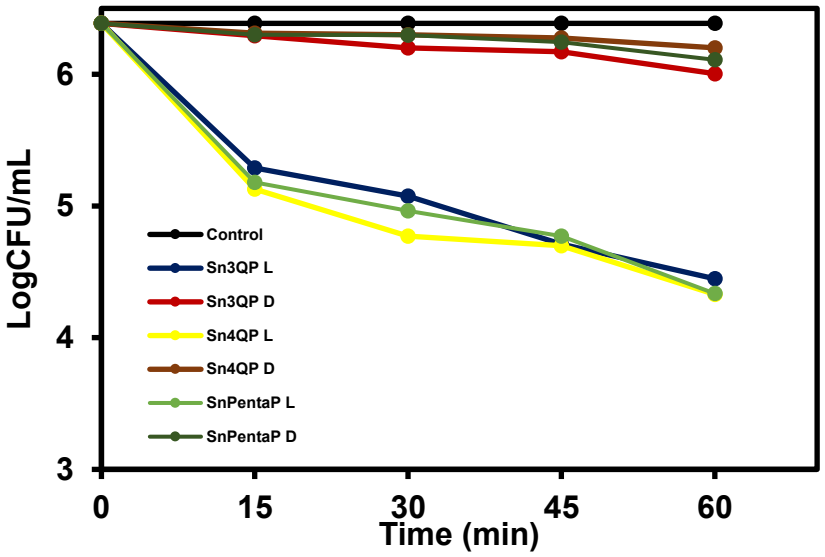

Figure 64: Log_{10} CFU/mL values for Sn(IV) porphyrins against *E. coli*. D and L refer to the dark and light studies, respectively.

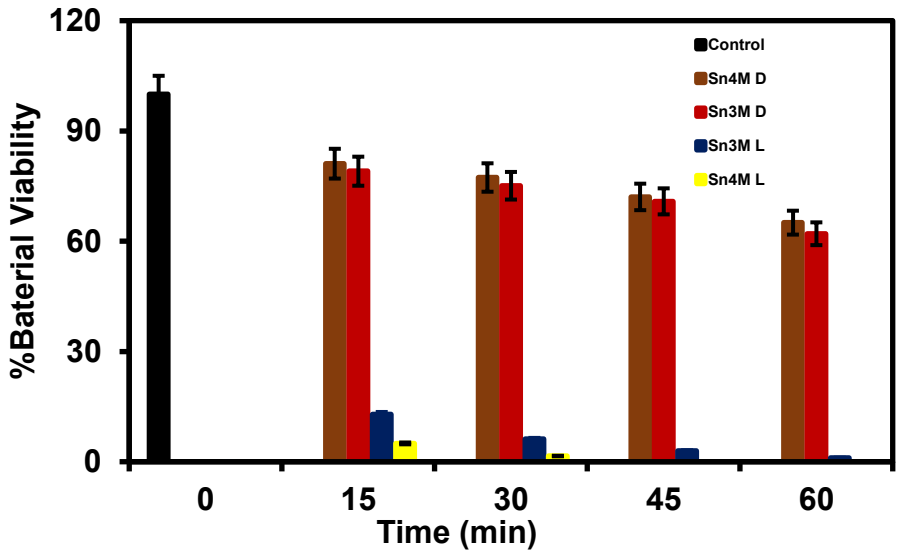

Figure 65: Bacterial viability data for quaternised porphyrins against *E. coli*. D and L refer to the dark and light studies, respectively.

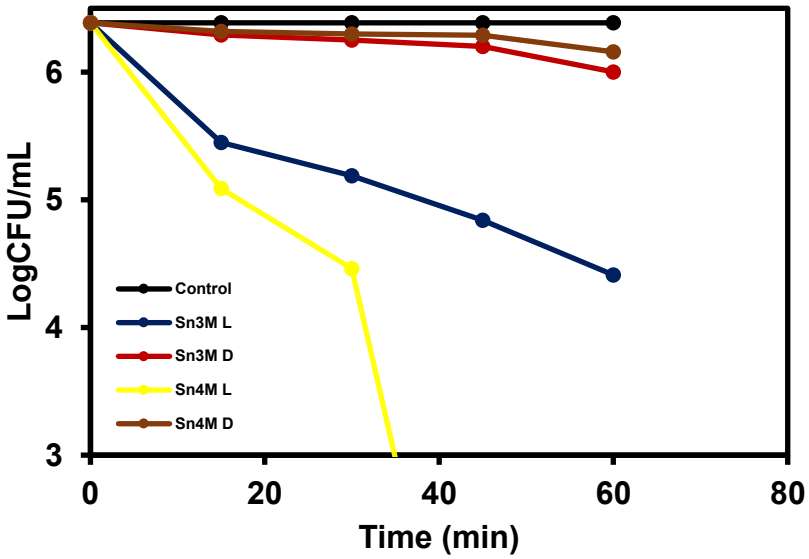

Figure 66: Log_{10} CFU/mL values for quaternised porphyrins against *E. coli*. D and L refer to the dark and light studies, respectively.

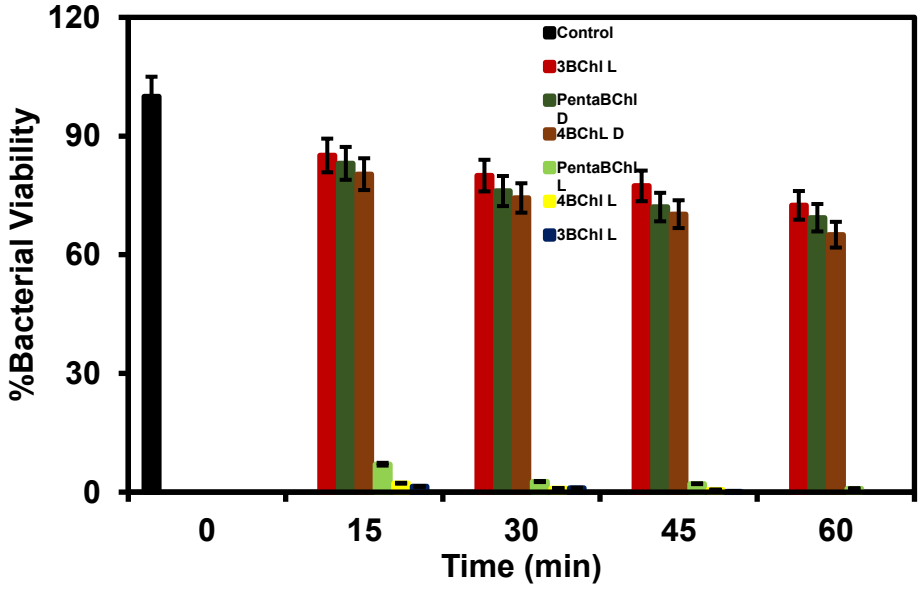

Figure 67: Bacterial viability data for free base BChls against *E. coli*. D and L refer to the dark and light studies, respectively.

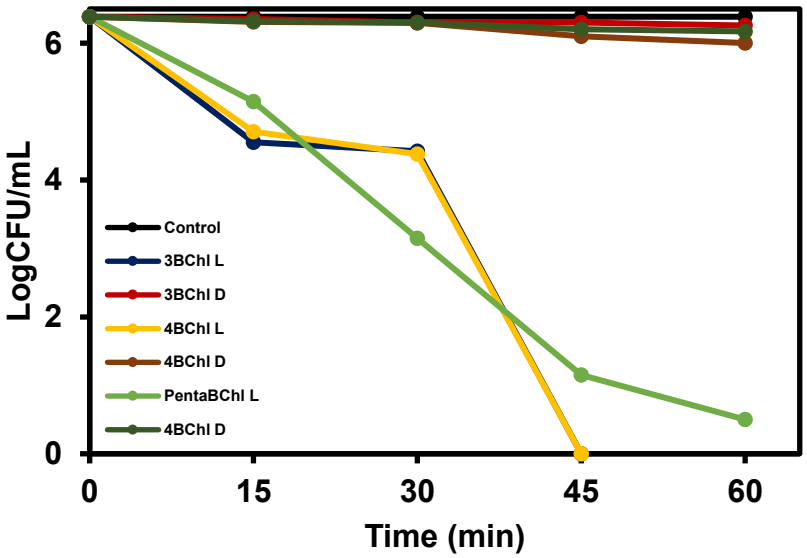

Figure 68: Log_{10} CFU/mL values for free base BChls against *E. coli*. D and L refer to the dark and light studies, respectively.

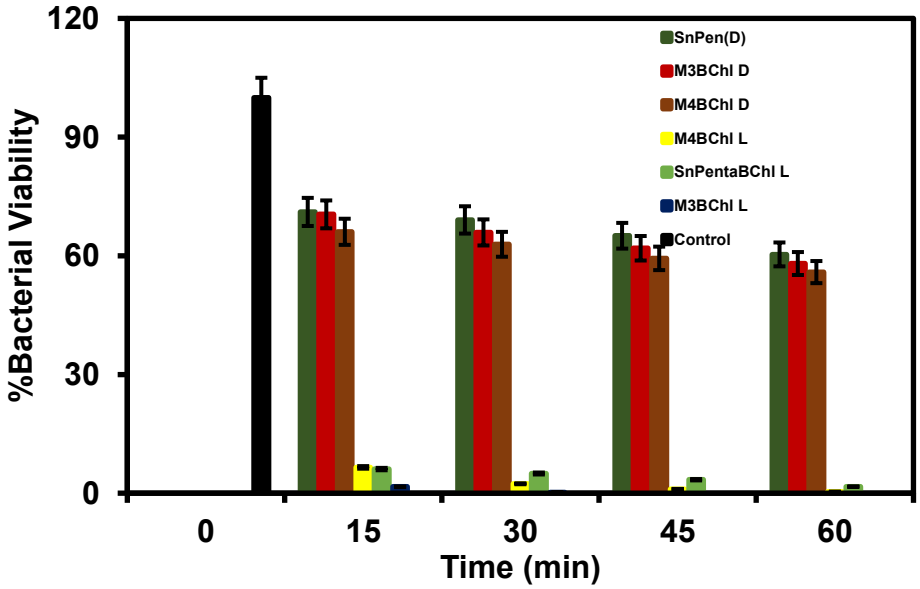

Figure 69: Bacterial viability data for Sn(IV) and quaternised BChls against *E. coli*. D and L refer to the dark and light studies, respectively.

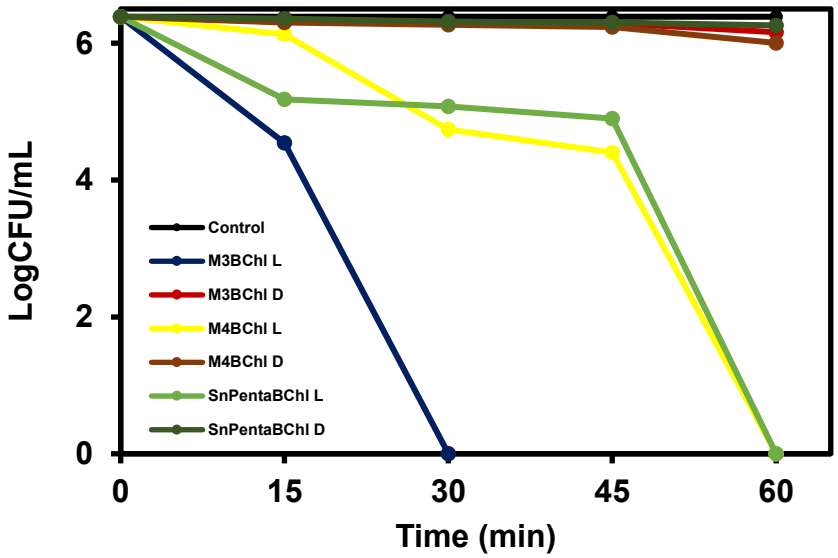

Figure 70: Log_{10} CFU/mL values for Sn(IV) and quaternised BChls against *E. coli*. D and L refer to the dark and light studies, respectively.

Table 7: A summary of the log reduction values against *E. coli.*

	E. coli	
PS	**LIGHT**[a]	**DARK**
3QP	1.39	0.39
Sn3QP	1.94	0.38
Sn3M	1.97	0.38
3QBChl	6.39 (@ 45 min)	0.13
M3BChl	6.39 (@ 30 min)	0.23
4QP	1.75	0.57
Sn4QP	2.06	0.19
Sn4M	6.39 (@ 45 min)	0.23
4QBChl	6.39 (@ 45 min)	0.39
M4BChl	6.39 (@ 60 min)	0.38
PentaP	6.39 (@ 45 min)	0.87
SnPentaP	2.05	0.28
PentaBChl	5.89	0.21
SnPentaBChl	6.39 (@ 60 min)	0.13

[a] The irradiation time at which full eradication of the bacteria is achieved is provided in parentheses where relevant.

Concluding remarks

From the trends observed in the PACT activity data, it can be concluded that the compounds were generally most effective against the Gram-(−) *E. coli* bacteria, with complete eradication being observed with **3QBChl**, **M3BChl**, **Sn4M**, **4QBChl**, **M4BChl**, **PentaP** and **SnPentaBChl**. It is noteworthy that this was observed even in the absence of the introduction of positively charged moieties in the context of **3QBChl**, **4QBChl** and **SnPentaBChl**. This is unusual in the context of Gram-(−) bacteria. Similar data have been reported for chlorins in recent years by Mack and coworkers.[31] During treatments of Gram-(+) *S. aureus* bacteria, only the Sn(IV) and quaternised BChls resulted in complete eradication. These studies demonstrate that the PACT activity properties of synthetic tetraarylbacteriochlorins merit further in-depth study.

6. MOLECULAR MODELLING

Geometry optimisations were carried out for **3QP**, **4QP**, **PentaP**, **SnPentaP**, **PentaBChl** and **SnPentaBChl** at the B3LYP/SDD level of theory by using the Gaussian 09 software package[193] on the Lengau cluster of the Centre for High Performance Computing in Cape Town. The default SDD basis sets were selected so that the results for the free base ligands can be readily compared to those of the Sn(IV) complexes. Time-dependent density functional theory (TD-DFT) calculations were carried out at the CAM-B3LYP/SDD level of theory to further analyse the molecular implications of the structural modifications of the porphyrinoids selected for this study. The CAM-B3LYP functional was selected since it contains a long-range correction.[194] One of the aims of this study was to assess whether the position of the quinoline nitrogen atoms has an effect on the molecular properties. For this reason, the Free base **3QP** and **4QP** dyes were modelled to determine the effect of the *meso*-aryl rings on the frontier MO energies and the calculated Q and B band regions (**Figure 71**). The entire pentafluorophenyl-substituted series was studied to determine the effect of the reduction of the ligand along the *y*-axis to form BChls.

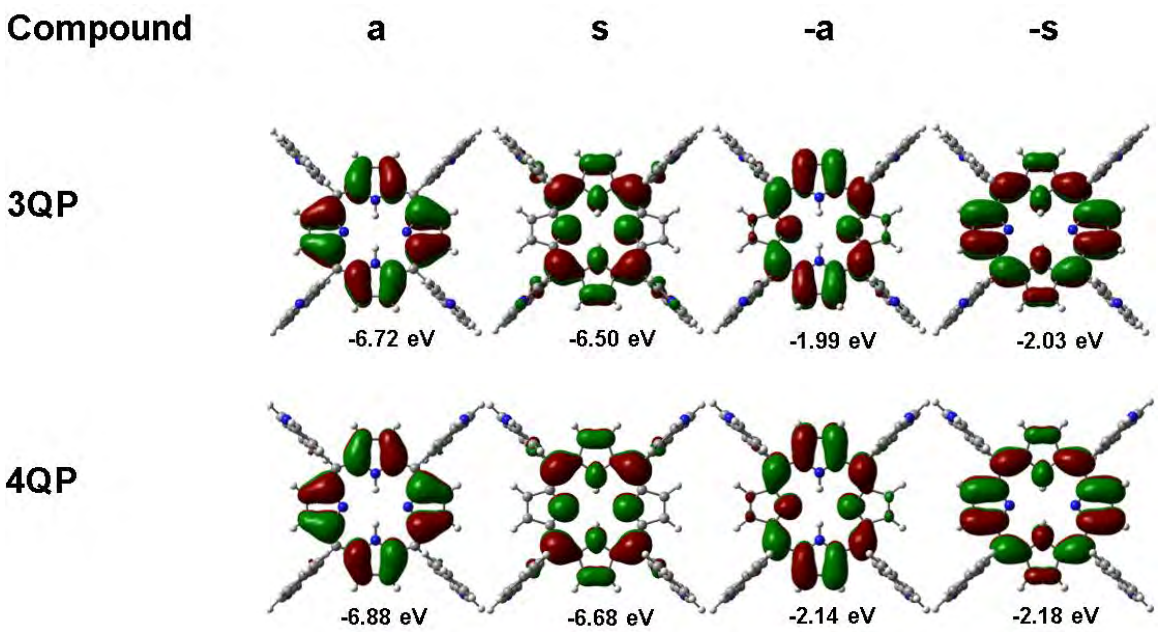

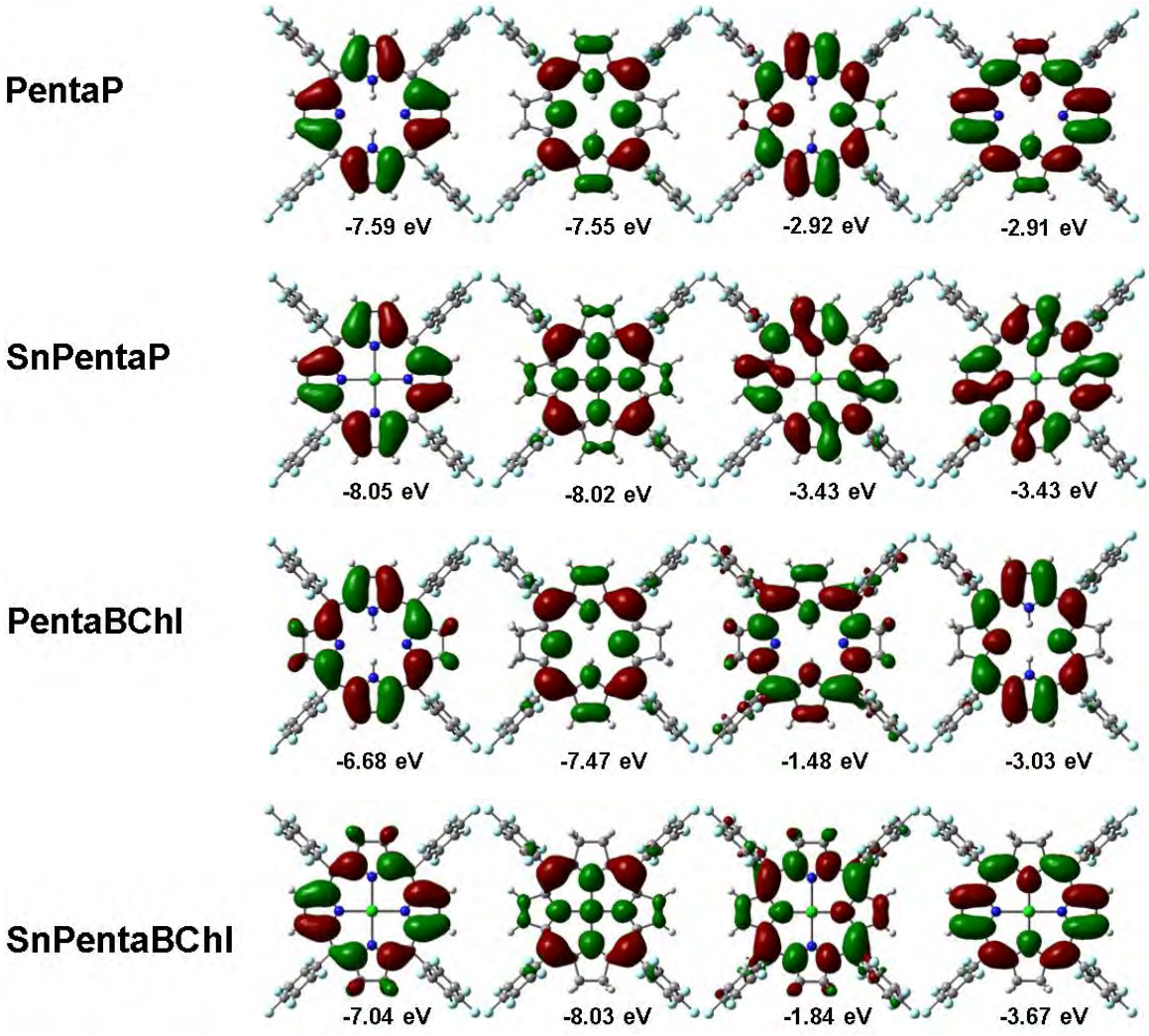

Figure 71: The four frontiers π-MOs derived from the HOMO and LUMO of a $C_{16}H_{16}^{2-}$ parent perimeter are referred to as the **a**, **s**, **-a**, and **-s** MOs in the context of Michl's perimeter model.[196] The MO plots are provided at an isosurface of 0.02 a.u. The *y*-axis is aligned vertical to the page for all dyes except **PentaBChl**.

Conceptual frameworks such as Gouterman's 4-orbital model[195] and Michl's perimeter model[196] can be used to identify trends in the energies of the four frontier orbital MOs that are derived from the HOMO and LUMO of a parent $C_{16}H_{16}^{2-}$ parent perimeter. For these studies, the energy splitting of the **a** and **s** MOs is described as a change in the ΔHOMO value in the context of Michl's perimeter model,[196] while the energy splitting of the **-a** and **-s** MOs is described by the change in the ΔLUMO value.

Changes in the electronic absorption bands across a range of porphyrinoids with varying molecular symmetries can be explained on the basis of modifications to the relative energy of the four frontier orbitals and the ΔHOMO and ΔLUMO values. There is a slight stabilisation of the frontier MOs of **4QP** relative to those of **3QP**, since the electronegative nitrogen atom lies further from the *meso*-carbon atom. **PentaP** with twenty electronegative fluorine atoms on the *meso*-rings has lower **a**, **s**, **-a** and **-s** MO energy values than **3QP** and **4QP**. This implies that reduction will be favoured, which was observed during the **PentaBChl** synthesis. Upon metalation of **PentaP** and **PentaBChl**, there is a further stabilisation of the frontier MOs due to the tetravalent central metal ion.

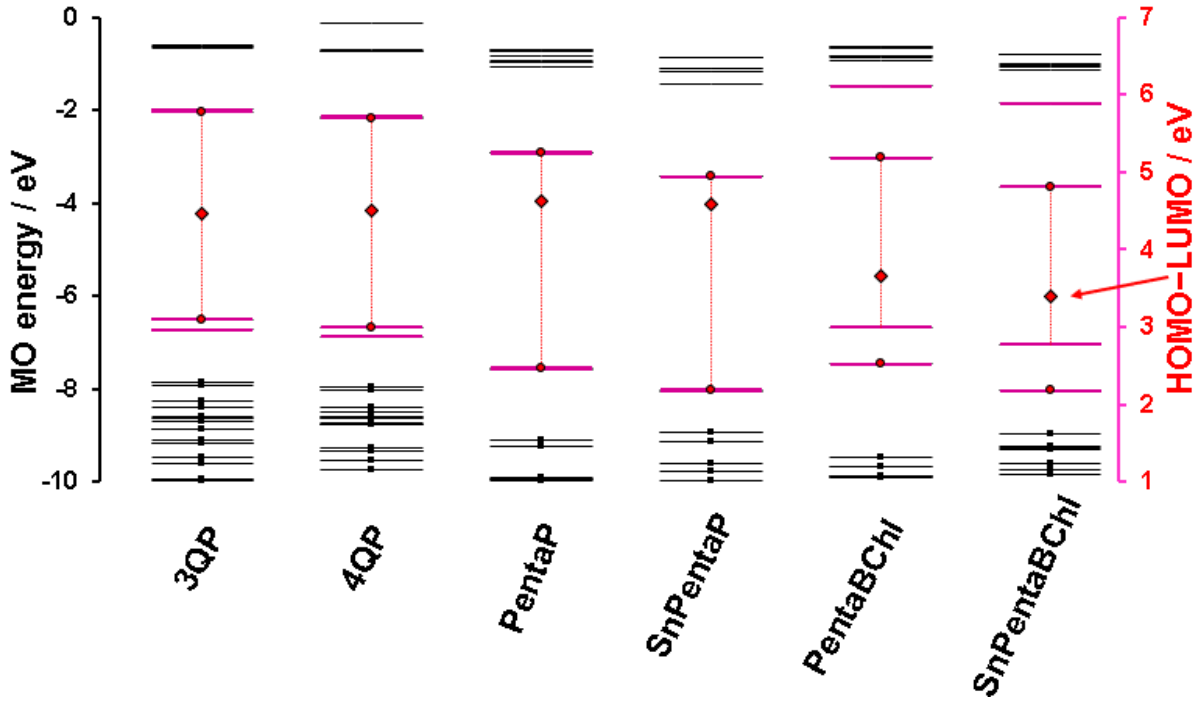

Figure 72: MO energies of **3QP**, **4QP**, **PentaP**, **SnPentaP**, **PentaBChl** and **SnPentaBChl**. The HOMO–LUMO gaps are plotted against a secondary axis and are denoted by red diamonds. Red circles highlight the **s** and **-s** MOs, while small black squares denote lower-lying occupied MOs.

As depicted in **Figure 75**, the frontier MOs of **3QP** are slightly destabilised relative to those of **4QP**, with little difference in the HOMO−LUMO gaps of these compounds. An analysis of the pentafluorophenyl-substituted series illustrates that there is a marked

narrowing of the HOMO−LUMO gaps of **PentaBChl** and **SnPenBChl** due to the large relative destabilisation of the **a** MO, which has large MO coefficients on the ligand periphery where reduction takes place (**Figure 72**).

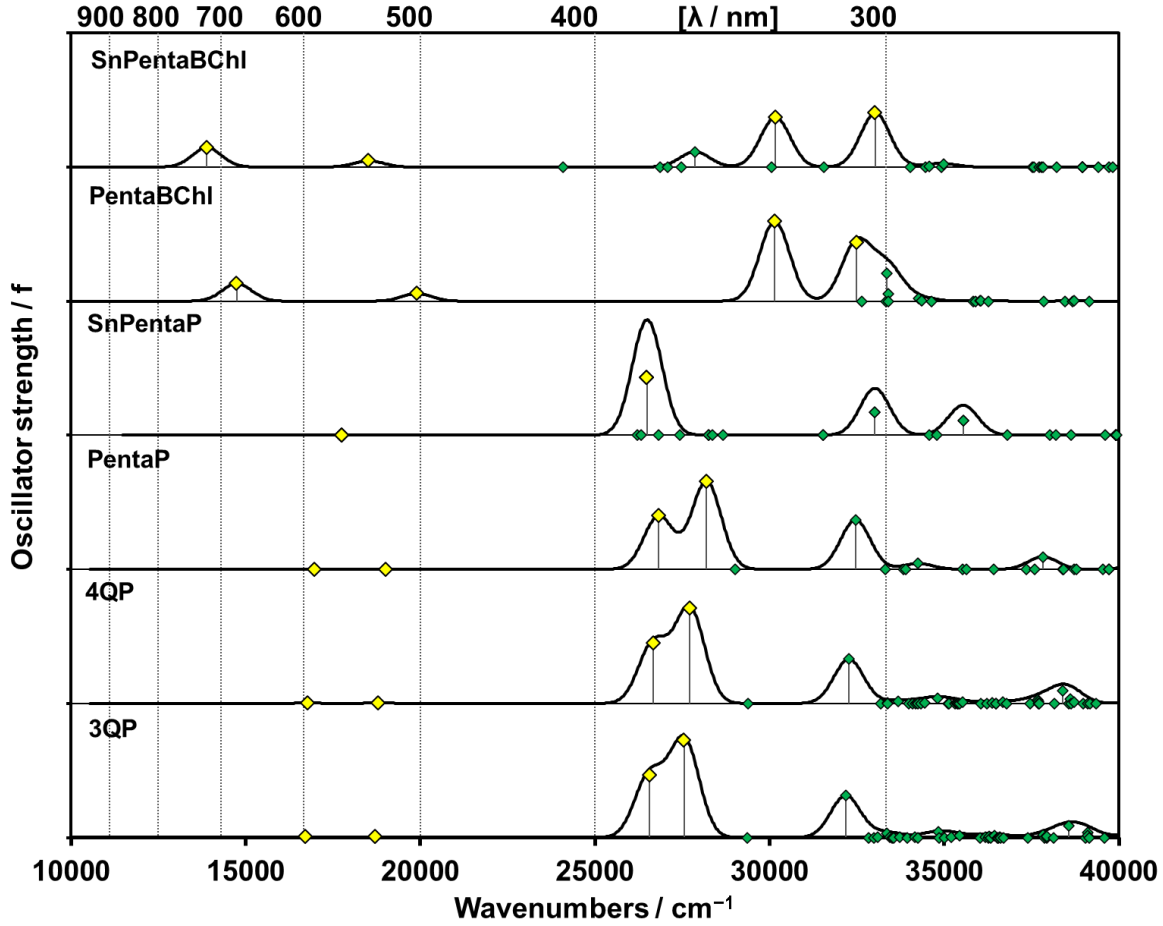

Figure 73: The calculated TD–DFT spectra of optimised geometries of **3QP**, **4QP**, **PentaP**, **SnPentaP**, **PentaBChl** and **SnPentaBChl** at the CAM–B3LYP/SDD level of theory. The Q and B bands are highlighted with yellow diamonds. Details of the calculations are provided in **Table 8**.

The calculated spectroscopic difference between **3QP** and **4QP** is negligible. The Q and B bands lie in the same range, corroborating the experimental data. For **PentaP**, upon metalation, the Q and B bands are blue-shifted relative to those of **3QP** and **4QP** (**Figure 74** and **Table 8**). In contrast, the Q bands of BChls are red-shifted, while the B bands are blue-shifted. This is related to the lifting of the orbital degeneracies of both the **a** and **s** MOs and **-a** and **-s** MOs (**Figure 73**), since the reduction of the ligand

along the *y*-axis markedly destabilises the **a** and **-a** MOs, which have large MO coefficients on the ligand periphery along this axis (**Figure 72**).

Table 8: Calculated and experimental electronic excitation wavelengths of **3QP**, **4QP**, **PentaP**, **SnPentaP**, **PentaBChl**, and **SnPentaBChl**, and their respective calculated wavenumbers and wavefunctions were calculated at the CAM-B3LY/SDD level of theory.

#[a]	Band[b]	v.10^3 (cm^{-1})[c]	λ_{calc}(nm)[d]	λ_{exp}(nm)[e]	f[f]	Wavefunction =[e]
			3QP			
1	Q	16.7	599	594	0.01	**61% s** → **-s; 38% a** → **-a;** …
2	Q	18.7	534	556	0.01	**55% s** → **-a; 44% a** → **-s;** …
3	B	26.6	376	426	1.17	**56% a** → **-a; 29% s** → **-s;** …
4	B	27.6	363		1.82	**55% a** → **-s; 42% s** → **-a;** …
			4QP			
1	Q	16.7	596	586	0.00	**61% s** → **-s; 39% a** → **-a;** …
2	Q	18.8	532	515	0.01	**54% s** → **-a; 54% s** → **-a;** …
3	B	26.7	375	419	1.13	**55% a** → **-a; 29% s** → **-a;** …
4	B	27.7	361		1.77	**55% a** → **-s; 42% -s** → **a;** …
			PentaP			
1	Q	17.0	589	584	0.00	**55% s** → **-s; 45% a** → **-a;** …
2	Q	19.0	526	503	0.00	**51% s** → **-a; 49% a** → **-s;** …
3	B	26.8	373	406	1.00	**48% a** → **-a; 31% s** → **-s;** …
4	B	28.2	355		1.64	**51% a** → **-s; 47% s** → **-a;** …
			SnPentaP			
1	Q	17.8	563	553	0.00	**54% s** → **-a; 46% a** → **-s;** …
2	Q	17.8	563		0.00	**54% s** → **-s; 46% a** → **-a;** …
5	B	26.2	377	422	1.08	**51% a** → **-s; 39% s** → **-a;** …
6	B	26.3	377		1.08	**51% a** → **-a; 40% s** → **-s;** …
			PentaBChl			
1	Q	14.8	678	687	0.33	**90% a** → **-s;** …
2	Q	19.9	502	508	0.14	**74% s** → **-s; 25% a** → **-a;** …
3	B	30.2	332	375	1.49	**76% a** → **-a;** 27% s → L+3**;** …
4	B	32.5	308	345	1.09	**63% s** → **-a; 27% a** → **-s;** …
			SnPentaBChl			
1	Q	13.9	720	749	0.36	**95% a** → **-s;** …
2	Q	18.5	540	553	0.12	**80% s** → **-s; 18% a** → **-a;** …
9	B	24.1	332	374	0.93	**47% s** → **-s; 37% a** → **-a;** …
11	B	26.9	303	341	1.01	**91% s** → **-a;** …

a Excited state number of TD-DFT calculations. **b** Porphyrin band assignments. **c** Wavenumbers obtained from TD-DFT calculations. **d** Calculated wavelengths in nanometers. **e** Experimental wavelengths in nanometers. **f** Calculated oscillator strengths. **e** Using eigenvectors predicted by TD-DFT, the wavefunctions define the MOs participating in the transition are described. Only 10% contributions or greater are included.

The last focal point of the modelling was to calculate the energies of the Q and B-bands of Gouterman's 4-orbital model[195] using TD-DFT studies (**Table 8**). According

to the Gouterman four-orbital model,[195] the four frontier molecular orbitals that determine the UV-visible spectra of porphyrins under D_{4h} symmetry are a doubly degenerate LUMO (**a** and **s**) and a pair of accidentally degenerate HOMO and HOMO−1 (**-a** and **-s**) that are derived from the HOMO of the parent $C_{16}H_{16}^{2-}$ parent hydrocarbon perimeter. The calculated wavefunctions of the compounds illustrate that the Free base and metalated porphyrins follow this model. The percentage contributions of the one-electron transitions between the **a**, **s**, **-a** and **-s** MOs for the Q and B bands are *ca.* 50% (**Table 8**). The electron dipole transition moments cancel in the case of the Q transitions,[195] resulting in nearly fully forbidden bands, while they add together in the case of the B transitions, resulting in fully allowed spectral bands. When the porphyrins are reduced to BChls, the one-electron transition percentages increase (**Table 8**) due to the large splittings of the **-a** and **-s** MOs (i.e. the ΔLUMO value) when the ligand periphery is reduced along the *y*-axis. This results in an intensification of the lowest energy Q band since the electron dipole transition moments no longer cancel.

Concluding remarks

The molecular modelling data depict the same general trends observed experimentally but provide more insights. The only difference between the MO energies for **3QP** and **4QP** that might explain the spectral and molecular differences that are observed experimentally is the destabilisation of the frontier MOs of **3QP**, since the electronegative nitrogen atom lies closer to the *meso*-carbon atom. The pentafluorophenyl-substituted series illustrated that when the porphyrin is reduced to form a BChl, the HOMO−LUMO gap narrows significantly due to a relative destabilisation of the **a** MO that has large MO coefficients at the ligand periphery. As

a result, a red shift of the B and Q bands is observed. The lifting of the degeneracies of the MOs derived from the HOMO (i.e. **a** and **s**) and the LUMO (i.e. **-a** and **-s**) of the parent $C_{16}H_{16}^{2-}$ hydrocarbon perimeter results in an intensification of the lowest energy Q band, which further enhances the suitability of the dyes for use in PDT.

7. CONCLUSIONS

The aim of the project was to first study whether the position of the quinoline induces any significant changes in properties by comparing 3- and 4-quinoline-substituted porphyrins. Then, the other evaluation was to compare the quinoline EDGs and EWG of the pentafluorophenyl to synthesise novel BChls for PDT and PACT. Significantly lower IC_{50} values were obtained for BChls relative to porphyrins, with the highest PDT activity being observed against MCF-7 breast cancer cells for **PentaBChl** and **SnPentaBChl**.

- ✓ It was observed that the position of the quinoline nitrogen atom does induce significantly different photophysicochemical properties.
- ✓ The comparison of the EDG and EWG groups illustrated that the EWG played a large role in stabilising the BChls. Therefore, it was easier to synthesise pentafluorophenyl BChls compared to the quinoline BChls. This was also observed in the insertion of the metal to the core of the BChls with the quinoline-substituted dyes degrading, while the pentafluorophenyl-substituted dye did not.
- ✓ Since the carbon nanodot nanoparticle synthesis did not succeed, incorporating the TPP^+ moiety was scrutinised to evaluate whether cell permeability would be enhanced. This was only true for the cases where this moiety was conjugated to BChls. In future, lipophilicity studies should be carried out to further evaluate the potential utility of this approach and determine whether mono-substitution with a TPP^+ moiety would address significant solubility issues that were encountered that led to the need to use 5% DMSO to solubilise the dyes in PBS.

It was concluded that the position of the quinoline nitrogen atom does have a significant impact on the PDT and PACT activities of porphyrinoids. BChls with

EWGs are more stable and are mostly likely to perform well in photosensitiser studies. It was particularly noteworthy that high Log_{10} reduction values were obtained against Gram-(−) *E. coli* bacteria with free base and Sn(IV) BChls even in the absence of positively charged moieties in a similar manner to what has been observed recently by Mack and coworkers for chlorins.[41]

The PDT and PACT activity studies demonstrated that tetraarylBChls and their Sn(IV) complexes merit further in-depth study as photosensitiser dyes for PDT and PACT. In future, what would be interesting to ascertain is the photoactivity of BChls with different EWGs at the *meso* positions. Another interesting endeavour would be to introduce polar moieties to the BChls to make them more water-soluble. Surprisingly, the introduction of TPP^+ moieties to porphyrin and BChl ligands did not achieve this and did not enhance the PDT activity properties of the dyes. Lastly, instead of using metals for nanomaterials, the use of BChls as protein coronas can be explored for compound delivery to increase permeability and provide stable targeting materials that are small enough to keep their structural integrity to the targeted cells.

8. REFERENCES

1. Tsoucalas, G., & Sgantzos, M. (2016). Hippocrates (ca 460-370 BC) on nasal cancer. *Journal of the Balkan Union of Oncology*, *21*(4), 1031–1034. https://jbuon.com/archive/21-4-1031.pdf
2. Ekmektzoglou , K. A., Theodoros , T., Vasilios , V., & Zografos, G. C. (2009). Breast cancer: From the earliest times through to the end of the 20th century. *European Journal of Obstetrics & Gynecology and Reproductive Biology*, *145*(1), 3–8. https://doi.org/10.1016/j.ejogrb.2009.03.017
3. What is cancer? National Cancer Institute, National Institutes of Health, Bethesda, Maryland, USA. https://www.cancer.gov/about-cancer/understanding/what-is-cancer {Accessed: 28 Dec 2023}
4. Curigliano, G., Burstein, H. J., Winer, E. P., Gnant, M., Dubsky, P., Loibl, S., Colleoni, M., Regan, M. M., Piccart-Gebhart, M., Senn, H. J., Thürlimann, B., St. Gallen International Expert Consensus on the Primary Therapy of Early Breast Cancer 2017, André, F., Baselga, J., Bergh, J., Bonnefoi, H., Brucker, S. Y., Cardoso, F., Carey, L., Ciruelos, E., Cuzick, J., Denkert, C., Di Leo, A., Ejlertsen, B., Francis, P., Galimberti, V., Garber, J., Gulluoglu, B., Goodwin, P., Harbeck, N., Hayes, D. F., Huang, C.-S., Huober, J., Hussein, K., Jassem, J., Jiang, Z., Karlsson, P., Morrow, M., Orecchia, R., Osborne, K. C., Pagani, O., Partridge, A. H., Pritchard, K., Ro, J., Rutgers, E. J. T., Sedlmayer, F., Semiglazov, V., Shao, Z., Smith, I., Toi, M., Tutt, A., Viale, G., Watanabe, T., Whelan, T. J., & Xu, B. (2017). De-escalating and escalating treatments for early-stage breast cancer: the St. Gallen International Expert Consensus Conference on the Primary Therapy of Early Breast Cancer 2017. *Annals of Oncology*, *28*(8), 1700–1712. https://doi.org/10.1093/annonc/mdx308

5. A to Z List of Cancer Types. National Cancer Institute, National Institutes of Health, Bethesda, Maryland, USA. https://www.cancer.gov/types {Accessed: 28 Dec 2023}
6. Surgery for Cancer. National Cancer Institute, National Institutes of Health, Bethesda, Maryland, USA. https://www.cancer.gov/about-cancer/treatment/types/surgery {Accessed: 28 Dec 2023}
7. Ceresoli, M., Braga, M., Zanini, N., Abu-Zidan, F. M., Parini, D., Langer, T., Sartelli, M., Damaskos, D., Biffl, W. L., Amico, F., Ansaloni, L., Balogh, Z. J., Bonavina, L., Civil, I., Cicuttin, E., Chirica, M., Cui, Y., De Simone, B., Di Carlo, I., Fette, A., Foti, G., Fogliata, M., Fraga, G. P., Fugazzola, P., Galante, J. M., Beka, S. G., Hecker, A., Jeekel, J., Kirkpatrick, A. W., Koike, K., Leppäniemi, A., Marzi, I., Moore, E. E., Picetti, E., Pikoulis, E., Pisano, M., Podda, M., Sakakushev, B. E., Shelat, V. G., Tan, E., Tebala, G. D., Velmahos, G., Weber, D. G., Agnoletti, V., Kluger, Y., Baiocchi, G., Catena, F., & Coccolini, F. (2023). Enhanced perioperative care in emergency general surgery: the WSES position paper. *World Journal of Emergency Surgery*, *18*(1), 47. https://doi.org/10.1186/s13017-023-00519-2
8. Anesthesia. National Institute of General Medical Sciences (NIGMS), Bethesda, Maryland, United States. https://www.nigms.nih.gov/education/fact-sheets/Pages/anesthesia.aspx {Accessed: Dec 28 2023}
9. Leukemia Treatments. Johns Hopkins Medicine, Baltimore, Maryland, USA. https://www.hopkinsmedicine.org/kimmel-cancer-center/cancers-we-treat/leukemia-program/current-treatments {Accessed: Dec 28 2023}
10. Abraham, J., & Staffurth, J. (2016, January 1). Hormonal therapy for cancer. *Medicine*, *44*(1), 30–33. https://doi.org/10.1016/j.mpmed.2015.10.014
11. Lam, J. S., Leppert, J. T., Vemulapalli, S. N., Shvarts, O., & Belldegrun, A. S. (2006, January 1). Secondary Hormonal Therapy for Advanced Prostate Cancer. *The Journal of Urology*, *175*(1), 27–34. https://doi.org/10.1016/s0022-5347(05)00034-0
12. Zheng, S., Li, L., Chen, M., Yang, B., Chen, J., Li, G., Shao, Z., & Wu, J. (2022, June 1). Benefits of neoadjuvant therapy compared with adjuvant chemotherapy for the

survival of patients with HER2-positive breast cancer: A retrospective cohort study at FUSCC. *The Breast*, *63*, 177–186. https://doi.org/10.1016/j.breast.2022.03.015

13. Fleming, L., Agnew, S., Peddie, N., Crawford, M. R., Dixon, D., & Macpherson, I. (2022, August 1). The impact of medication side effects on adherence and persistence to hormone therapy in breast cancer survivors: A quantitative systematic review. *The Breast*, *64*, 63–84. https://doi.org/10.1016/j.breast.2022.04.010

14. Mustafa, M. I., & Mohammed, A. (2023, August 1). Nanobodies: A Game-Changer in Cell-Mediated Immunotherapy for Cancer. *SLAS Discovery*, *8*, 358–364. https://doi.org/10.1016/j.slasd.2023.08.008

15. Pathania, A. S., Prathipati, P., Murakonda, S. P., Murakonda, A. B., Srivastava, A., Avadhesh, A., Byrareddy, S. N., Coulter, D. W., Gupta, S. C., & Challagundla, K. B. (2022, November 1). Immune checkpoint molecules in neuroblastoma: A clinical perspective. *Seminars in Cancer Biology*, *86, Part 2*, 247–258. https://doi.org/10.1016/j.semcancer.2022.06.013

16. Yeung, H., Supapannachart, K. J., Francois, S., Adler, C., Kudchadkar, R. R., Lawson, D. H., Yushak, M., Shariff, A., & Chen, S. (2023, November 1). Cutaneous and Non-Cutaneous Adverse Effects in Patients with Advanced Melanoma Receiving Immunotherapy. *JID Innovations*, *3*, 100232. https://doi.org/10.1016/j.xjidi.2023.100232

17. Chang, Y., & Zhao, X. (2021, October 28). Haploidentical Stem Cell Transplantation for Acute Myeloid Leukemia: Current Therapies, Challenges and Future Prospective. *Frontiers in Oncology*, *11*, 758512. https://doi.org/10.3389/fonc.2021.758512

18. Stem Cell and Bone Marrow Transplants for Cancer. National Cancer Institute, National Institutes of Health, Bethesda, Maryland, USA. https://www.cancer.gov/about-cancer/treatment/types/stem-cell-transplant {Accessed: 28 Dec 2023}

19. Clinical trial researches drug therapy for chronic graft-versus-host disease. Center for Cancer Research, National Cancer Institute, National Institutes of Health, Bethesda,

Maryland, USA.. https://ccr.cancer.gov/news/article/clinical-trial-researches-drug-therapy-for-chronic-graft-versus-host-disease {Accessed: 28 Dec 2023}

20. Liebl, C. M., Kutschan, S., Dörfler, J., Käsmann, L., & Hübner, J. (2022). Systematic review about complementary medical hyperthermia in oncology. *Clinical and Experimental Medicine*, *22*(4), 519–565. https://doi.org/10.1007/s10238-022-00846-9

21. Hyperthermie: Wärme gegen Krebs. Krebsinformationsdienst, Deutsches Krebsforschungszentrum, Heidelberg, Germany. https://www.krebsinformationsdienst.de/behandlung/hyperthermie.php#inhalt17 {Accessed: 28 Dec 2023}

22. Bienia, A., Wiecheć-Cudak, O., Murzyn, A. A., & Krzykawska-Serda, M. (2021). Photodynamic Therapy and Hyperthermia in Combination Treatment-Neglected Forces in the Fight against Cancer. *Pharmaceutics*, *13*(8), 1147. https://doi.org/10.3390/pharmaceutics13081147

23. Baskar, R., Lee, K. A., Yeo, R., & Yeoh, K. W. (2012). Cancer and radiation therapy: current advances and future directions. *International Journal of Medical Sciences*, *9*(3), 193–199. https://doi.org/10.7150/ijms.3635

24. Dietrich, A., Koi, L., Zöphel, K., Sihver, W., Kotzerke, J., Baumann, M., & Krause, M. (2015). Improving external beam radiotherapy by combination with internal irradiation. *The British Journal of Radiology*, *88*(1051), 20150042.

25. Radiation therapy. Mayo Clinic, Rochester, Minnesota, United States. https://www.mayoclinic.org/tests-procedures/radiation-therapy/about/pac-20385162 {Accessed: 28 Dec 2023}

26. Zhong, L., Li, Y., Xiong, L., Wang, W., Wu, M., Yuan, T., Yang, W., Tian, C., Miao, Z., Wang, T., & Yang, S. (2021). Small molecules in targeted cancer therapy: advances, challenges, and future perspectives. *Signal Transduction and Targeted Therapy*, *6*(1), 201. https://doi.org/10.1038/s41392-021-00572-w

27. Papac, R. J. (2001). Origins of cancer therapy. *The Yale Journal of Biology and Medicine*, *74*(6), 391.

28. DeVita, V. T., & Chu, E. (2008, October 30). A History of Cancer Chemotherapy. *Cancer Research*, *68*(21), 8643–8653. https://doi.org/10.1158/0008-5472.can-07-6611

29. Mosca, L., Ilari, A., Fazi, F., Assaraf, Y. G., & Colotti, G. (2021). Taxanes in cancer treatment: Activity, chemoresistance and its overcoming. *Drug Resistance Updates*, *54*, 100742. https://doi.org/10.1016/j.drup.2020.100742

30. What is Chemotherapy? Cancer.Net, American Society of Clinical Oncology, Alexandria, Virginia, United States. https://www.cancer.net/navigating-cancer-care/how-cancer-treated/chemotherapy/what-chemotherapy {Accessed: 28 Dec 2023}

31. Hong, W. K., Bromer, R. H., Amato, D. A., Shapshay, S., Vincent, M., Vaughan, C., Willett, B., Katz, A., Welch, J., Fofonoff, S., & Strong, M. S. (1985). Patterns of relapse in locally advanced head and neck cancer patients who achieved complete remission after combined modality therapy. *Cancer*, *56*(6), 1242–1245. https://doi.org/10.1002/1097-0142(19850915)56:6<1242::AID-CNCR2820560603>3.0.CO;2-Z

32. Chemotherapy. Mayo Clinic, Rochester, Minnesota, United States. https://www.mayoclinic.org/tests-procedures/chemotherapy/about/pac-20385033 {Accessed: 28 Dec 2023}

33. Kaur, S., Mayanglambam, P., Bajwan, D., & Thakur, N. (2022). Chemotherapy and its adverse effects-A systematic review. *International Journal of Nursing Education and Research*, *10*(4), 399–402. https://doi.org/10.52711/2454-2660.2022.00090

34. Dougherty, T. J., Gomer, C. J., Henderson, B. W., Jori, G., Kessel, D., Korbelik, M., Moan, J. E., & Peng, Q. (1998, June 17). Photodynamic Therapy. *Journal of the National Cancer Institute*, *90*, 889–905. https://doi.org/10.1093/jnci/90.12.889

35. Zhang, Q., He, J., Wang, Y., Yan-Chun, L., Liu, Z., Zhou, B. N., & Liu, Y. (2020, January 1). A promising anticancer drug: a photosensitizer based on the porphyrin skeleton. *RSC Medicinal Chemistry*, *11*, 427–437. https://doi.org/10.1039/c9md00558g

36. Tabrizi, P. F., Wennige, S., Berneburg, M., & Maisch, T. (2018, March 1). Susceptibility of sodA- and sodB-deficient *Escherichia coli* mutant towards antimicrobial photodynamic inactivation via the type I-mechanism of action. *Photochemical & Photobiological Sciences*, *17*, 352–362. https://doi.org/10.1039/c7pp00370f

37. Feng, G., Zhang, G., & Ding, D. (2020, January 1). Design of superior phototheranostic agents guided by Jablonski diagrams. *Chemical Society Reviews*, *49*, 8179–8234. https://doi.org/10.1039/d0cs00671h

38. Xiao, J., Cong, H., Wang, S., Yu, B., & Shen, Y. (2021, January 1). Recent research progress in the construction of active free radical nanoreactors and their applications in photodynamic therapy. *Biomaterials Science*, *9*(7), 2384–2412. https://doi.org/10.1039/d0bm02013c

39. Maisch, T. (2015, August 1). Resistance in antimicrobial photodynamic inactivation of bacteria. *Photochemical and Photobiological Sciences, 14*, 1518–1526. https://doi.org/10.1039/c5pp00037h

40. Senge, M. O., Sergeeva, N. N., & Hale, K. J. (2021, January 1). Classic highlights in porphyrin and porphyrinoid total synthesis and biosynthesis. *Chemical Society Reviews, 50*(7), 4730–4789. https://doi.org/10.1039/c7cs00719a

41. Babu, B., Mack, J., & Nyokong, T. (2023, January 1). Sn(iv)-porphyrinoids for photodynamic anticancer and antimicrobial chemotherapy. *Dalton Transactions, 52*(16), 5000–5018. https://doi.org/10.1039/d3dt00603d

42. Majumdar, P., Raju, N., & Zhao, J. (2014, January 1). Activatable triplet photosensitizers: magic bullets for targeted photodynamic therapy. *Journal of Materials Chemistry C*, *2*, 5982–5997. https://doi.org/10.1039/c4tc00659c

43. Ethirajan, M., Chen, Y., Joshi, P., & Pandey, R. K. (2011, January 1). The role of porphyrin chemistry in tumor imaging and photodynamic therapy. *Chemical Society Reviews*, *40*, 340–362. https://doi.org/10.1039/b915149b

44. Aslanoglu, B., Yakavets, I., Zorin, V., Lassalle, H. P., Ingrosso, F., Monari, A., & Çatak, A. (2020, January 1). Optical properties of photodynamic therapy drugs in different

environments: the paradigmatic case of temoporfin. *Physical Chemistry Chemical Physics*, *22*, 16956–16964. https://doi.org/10.1039/d0cp02055a

45. Glaß, S., Rüdiger, T., Griebel, J., Abel, B., & Schulze, A. (2018, January 1). Uptake and release of photosensitizers in a hydrogel for applications in photodynamic therapy: the impact of structural parameters on intrapolymer transport dynamics. *RSC Advances*, *8*, 41624–41632. https://doi.org/10.1039/c8ra08093c

46. Pucelik, B., Sułek, A., Drozd, A., Stochel, G., Pereira, M. M., Pinto, S. M. A., Arnaut, L. G., & Dąbrowski, J. M. (2020). Enhanced Cellular Uptake and Photodynamic Effect with Amphiphilic Fluorinated Porphyrins: The Role of Sulfoester Groups and the Nature of Reactive Oxygen Species. *International Journal of Molecular Sciences*, *21*(8), 2786. https://doi.org/10.3390/ijms21082786

47. Li, D., Liu, P., Tan, Y., Zhang, Z., Kang, M., Wang, D., & Tang, B. Z. (2022). Type I Photosensitizers Based on Aggregation-Induced Emission: A Rising Star in Photodynamic Therapy. *Biosensors*, *12*(9), 722. https://doi.org/10.3390/bios12090722

48. Quina, F. H., & Silva, G. T. M. (2021, September 1). The photophysics of photosensitization: A brief overview. *Journal of Photochemistry and Photobiology*, *7*, 100042. https://doi.org/10.1016/j.jpap.2021.100042

49. Abrahamse, H., & Hamblin, M. R. (2016). New photosensitizers for photodynamic therapy. *The Biochemical Journal*, *473*(4), 347–364. https://doi.org/10.1042/BJ20150942

50. Aveline, B. M. (2001, January 1). Chapter 2 Primary processes in photosensitization mechanisms. *Comprehensive Series in Photosciences*, *2*, 17–37. https://doi.org/10.1016/s1568-461x(01)80106-x

51. Escudero, A., Carrillo-Carrión, C., Castillejos, M. C., Romero-Ben, E., Rosales-Barrios, C., & Khiar, N. (2021, January 1). Photodynamic therapy: photosensitizers and nanostructures. *Materials Chemistry Frontiers*, *5*, 3788–3812. https://doi.org/10.1039/d0qm00922a

52. Lin, L., Song, X., Dong, X. & Li, B. (2021) Nano-photosensitizers for enhanced photodynamic therapy. *Photodiagnosis and Photodynamic*, *36*, 102597. https://doi.org/10.1016/j.pdpdt.2021.102597

53. Zhu, Y., & Silverman, R. B. (2007). Electronic effects of peripheral substituents at porphyrin *meso* positions. *The Journal of Organic Chemistry*, *72*(1), 233–239. https://doi.org/10.1021/jo061951j

54. Hiroto, S., Miyake, Y. & Shinokubo, H. (2017) Synthesis and Functionalization of Porphyrins through Organometallic Methodologies. *Chemical Reviews*, *117(4)*, 2910–3043. https://doi.org/10.1021/acs.chemrev.6b00427

55. Babu, B., Soy, R. C., Mack, J., & Nyokong, T. (2020). Non-aggregated lipophilic water-soluble tin porphyrins as photosensitizers for photodynamic therapy and photodynamic antimicrobial chemotherapy. *New Journal of Chemistry*, *44*(26), 11006–11012. https://doi.org/10.1039/d0nj01564d

56. Barclay, T. G., Day, C. M., Petrovsky, N., & Garg, S. (2019). Review of polysaccharide particle-based functional drug delivery. *Carbohydrate Polymers*, *221*, 94–112. https://doi.org/10.1016/j.carbpol.2019.05.067

57. Zhao, X., Sun, C., Xiong, F., Wang, T., Li, S., Huo, F., & Yao, X. (2023). Polymerization-Induced Self-Assembly for Efficient Fabrication of Biomedical Nanoplatforms. *Research*, *6*, 0113. https://doi.org/10.34133/research.0113

58. Wang, C., Wang, Z., & Zhang, X. (2011). Superamphiphiles as building blocks for supramolecular engineering: towards functional materials and surfaces. *Small*, *7*(10), 1379–1383. https://doi.org/10.1002/smll.201002365

59. Han, P., Ma, N., Ren, H., Xu, H., Li, Z., Wang, Z., & Zhang, X. (2010, August 19). Oxidation-Responsive Micelles Based on a Selenium-Containing Polymeric Superamphiphile. *Langmuir*, *26*(18), 14414–14418. https://doi.org/10.1021/la102837a

60. Quiñones, J. P., Peniche, H., & Peniche, C. (2018). Chitosan Based Self-Assembled Nanoparticles in Drug Delivery. *Polymers*, *10*(3), 235. https://doi.org/10.3390/polym10030235

61. Shovsky, A., Varga, I., Makuška, R., & Claesson, P. M. (2009, April 16). Formation and Stability of Water-Soluble, Molecular Polyelectrolyte Complexes: Effects of Charge Density, Mixing Ratio, and Polyelectrolyte Concentration. *Langmuir*, *25*(11), 6113–6121. https://doi.org/10.1021/la804189w

62. Khan, N., & Brettmann, B. (2018, December 31). Intermolecular Interactions in Polyelectrolyte and Surfactant Complexes in Solution. *Polymers*, *11*(1), 51. https://doi.org/10.3390/polym11010051

63. Zhuang, W. R., Wang, Y., Cui, P. F., Xing, L., Lee, J., Kim, D., Jiang, H. L., & Oh, Y. K. (2019, January). Applications of π-π stacking interactions in the design of drug-delivery systems. *Journal of Controlled Release*, *294*, 311–326. https://doi.org/10.1016/j.jconrel.2018.12.014

64. Jia, H., Bai, X., Shi, L., Lu, F., & Zheng, L. (2012). The effects of the π–π stacking interactions on the patterns of gold nanoparticles formed at the air–water interface. *Nanoscale*, *4*(10), 3162. https://doi.org/10.1039/c2nr30286a

65. Liu, Z., Jiao, Y., Wang, Y., Zhou, C., & Zhang, Z. (2008, December). Polysaccharides-based nanoparticles as drug delivery systems. *Advanced Drug Delivery Reviews*, *60*(15), 1650–1662. https://doi.org/10.1016/j.addr.2008.09.001

66. Bose, A., Roy Burman, D., Sikdar, B., & Patra, P. (2021). Nanomicelles: Types, properties and applications in drug delivery. *IET Nanobiotechnology*, *15*(1), 19–27. https://doi.org/10.1049/nbt2.12018

67. Webber, G. B., Wanless, E. J., Armes, S. P., & Biggs, S. (2005). Tunable diblock copolymer micelles–adapting behaviour via subtle chemical modifications. *Faraday Discussions*, *128*, 193–209. https://doi.org/10.1039/b403180f

68. Wang, H., Li, C., Wu, Q., Wen, H., Sun, T., & Xie, Z. (2022). A cationic BODIPY photosensitizer decorated with quaternary ammonium for high-efficiency photodynamic inhibition of bacterial growth. *Journal of Materials Chemistry B*, *10*(26), 4967–4973. https://doi.org/10.1039/d2tb00778a

69. Babu, B., Mack, J., & Nyokong, T. (2022). A Sn(iv) porphyrin with mitochondria targeting properties for enhanced photodynamic activity against MCF-7 cells. *New Journal of Chemistry*, *46*(11), 5288–5295. https://doi.org/10.1039/d2nj00350c

70. D'Ambrosio, M., Santos, A. C., Alejo-Armijo, A., Parola, A. J., & Costa, P. M. (2020, June 6). Light-Mediated Toxicity of Porphyrin-Like Pigments from a Marine Polychaeta. *Marine Drugs*, *18*(6), 302. https://doi.org/10.3390/md18060302

71. Ahmed, S., Davoust, E., Savoie, H., Boa, A. N., & Boyle, R. W. (2004, July 1). Thioglycosylated cationic porphyrins—convenient synthesis and photodynamic activity *in vitro*. *Tetrahedron Letters*, *45*(31), 6045–6047. https://doi.org/10.1016/j.tetlet.2004.06.021

72. Al-Omari S. (2013). Toward a molecular understanding of the photosensitizer-copper interaction for tumor destruction. *Biophysical Reviews*, *5*(4), 305–311. https://doi.org/10.1007/s12551-013-0112-4

73. Wieder, M. E., Hone, D. C., Cook, M. J., Handsley, M. M., Gavrilovic, J., & Russell, D. A. (2006). Intracellular photodynamic therapy with photosensitizer-nanoparticle conjugates: cancer therapy using a 'Trojan horse'. *Photochemical and Photobiological Sciences*, *5*(8), 727–734. https://doi.org/10.1039/b602830f

74. Sajjad, F., Han, Y., Bao, L., Yan, Y., O shea, D., Wang, L., & Chen, Z. (2021, December 30). The improvement of biocompatibility by incorporating porphyrins into carbon dots with photodynamic effects and pH sensitivities. *Journal of Biomaterials Applications*, *36*(8), 1378–1389. https://doi.org/10.1177/08853282211050449

75. Lelièvre, P., Sancey, L., Coll, J. L., Deniaud, A., & Busser, B. (2020). The Multifaceted Roles of Copper in Cancer: A Trace Metal Element with Dysregulated Metabolism, but Also a Target or a Bullet for Therapy. *Cancers*, *12*(12), 3594. https://doi.org/10.3390/cancers12123594

76. Gu, Q. S., Li, T., Liu, T., Yu, G., Mao, G. J., Xu, F., & Li, C. Y. (2023, July 24). Recent Advances in Design Strategies and Imaging Applications of Fluorescent Probes for ATP. *Chemosensors*, *11*(7), 417. https://doi.org/10.3390/chemosensors11070417

77. Lee, H., Hong, K. I., & Jang, W. D. (2018, January). Design and applications of molecular probes containing porphyrin derivatives. *Coordination Chemistry Reviews*, *354*, 46–73. https://doi.org/10.1016/j.ccr.2017.06.008

78. Szintay, G., & Horváth, A. (2001, November). Five-coordinate complex formation and luminescence quenching study of copper(II) porphyrins. *Inorganica Chimica Acta*, *324*(1–2), 278–285. https://doi.org/10.1016/s0020-1693(01)00620-x

79. Al-Omari, S., & Ali, A. (2009). Photodynamic activity of pyropheophorbide methyl ester and pyropheophorbide a in dimethylformamide solution. *General Physiology and Biophysics*, *28*(1), 70–77. https://doi.org/10.4149/gpb_2009_01_70

80. Nyman, E. S., & Hynninen, P. H. (2004, January). Research advances in the use of tetrapyrrolic photosensitizers for photodynamic therapy. *Journal of Photochemistry and Photobiology B: Biology*, *73*(1–2), 1–28. https://doi.org/10.1016/j.jphotobiol.2003.10.002

81. Foglar, M., Aumiller, M., Bochmann, K., Buchner, A., El Fahim, M., Quach, S., Sroka, R., Stepp, H., Thon, N., Forbrig, R., & Rühm, A. (2023). Interstitial Photodynamic Therapy of Glioblastomas: A Long-Term Follow-up Analysis of Survival and Volumetric MRI Data. *Cancers*, *15*(9), 2603. https://doi.org/10.3390/cancers15092603

82. Sibaud V. (2022). Anticancer treatments and photosensitivity. *Journal of the European Academy of Dermatology and Venereology*, *36*(Suppl 6), 51–58. https://doi.org/10.1111/jdv.18200

83. Castano, A. P., Demidova, T. N., & Hamblin, M. R. (2005). Mechanisms in photodynamic therapy: Part three-Photosensitizer pharmacokinetics, biodistribution, tumor localization and modes of tumor destruction. *Photodiagnosis and Photodynamic Therapy*, *2*(2), 91–106. https://doi.org/10.1016/S1572-1000(05)00060-8

84. *Photodynamic Therapy to Treat Cancer*. (2021, June 21). National Cancer Institute. https://www.cancer.gov/about-cancer/treatment/types/photodynamic-therapy

85. Kim, M. M., & Darafsheh, A. (2020, March). Light Sources and Dosimetry Techniques for Photodynamic Therapy. *Photochemistry and Photobiology*, *96*(2), 280–294. https://doi.org/10.1111/php.13219

86. Algorri, J. F., López-Higuera, J. M., Rodríguez-Cobo, L., & Cobo, A. (2023, August 3). Advanced Light Source Technologies for Photodynamic Therapy of Skin Cancer Lesions. *Pharmaceutics*, *15*(8), 2075. https://doi.org/10.3390/pharmaceutics15082075

87. Algorri, J. F., Ochoa, M., Roldán-Varona, P., Rodríguez-Cobo, L., & López-Higuera, J. M. (2021, July 13). Light Technology for Efficient and Effective Photodynamic Therapy: A Critical Review. *Cancers*, *13*(14), 3484. https://doi.org/10.3390/cancers13143484

88. Li, B., & Lin, L. (2022, April 6). Internal light source for deep photodynamic therapy. *Light: Science & Applications*, *11*(1). https://doi.org/10.1038/s41377-022-00780-1

89. *Laser Application Systems*. Changchun New Industries Optoelectronics Technology Co., Ltd. http://www.cnilaser.com/laser_system.htm (Accessed: Dec 29 2023)

90. Brancaleon, L., & Moseley, H. (2002). Laser and non-laser light sources for photodynamic therapy. *Lasers in Medical Science*, *17*(3), 173–186. https://doi.org/10.1007/s101030200027

91. Kim, M. M. & Darafsheh, A. (2020) Light Sources and Dosimetry Techniques for Photodynamic Therapy. Photochemistry Photobiology, 96(2), 280–294. https://doi.org/10.1111/php.13219

92. Algorri, J. F., López-Higuera, J. M., Rodriguez-Cobo, L. & Cobo, A. (2023) Advanced Light Source Technologies for Photodynamic Therapy of Skin Cancer Lesions. Pharmaceutics, 15(8), 2075. https://doi.org/10.3390/pharmaceutics15082075

93. Gunaydin, G., Gedik, M. E., & Ayan, S. (2021, August 2). Photodynamic Therapy for the Treatment and Diagnosis of Cancer–A Review of the Current Clinical Status. *Frontiers in Chemistry*, *9*, 686303. https://doi.org/10.3389/fchem.2021.686303

94. Romano, G., Insero, G., Marrugat, S. N., & Fusi, F. (2022, January 1). Innovative light sources for phototherapy. *Biomolecular Concepts*, *13*(1), 256–271. https://doi.org/10.1515/bmc-2022-0020

95. Triana, M. A., Restrepo, A. A., Lanzafame, R. J., Palomaki, P., & Dong, Y. (2020, June 15). Quantum dot light-emitting diodes as light sources in photomedicine: photodynamic therapy and photobiomodulation. *Journal of Physics: Materials*, *3*(3), 032002. https://doi.org/10.1088/2515-7639/ab95e8

96. Shi, X., Yin, H., Dong, X., Li, H., & Li, Y. (2022, December 16). Photodynamic therapy with light-emitting diode arrays producing different light fields induces apoptosis and necrosis in gastrointestinal cancer. *Frontiers in Oncology*, *12*, 1062666. https://doi.org/10.3389/fonc.2022.1062666

97. Piksa, M., Lian, C., Samuel, I. C., Pawlik, K. J., Samuel, I. D. W., & Matczyszyn, K. (2023). The role of the light source in antimicrobial photodynamic therapy. *Chemical Society Reviews*, *52*(5), 1697–1722. https://doi.org/10.1039/d0cs01051k

98. Lee, C. N., Hsu, R., Chen, H., & Wong, T. W. (2020). Daylight Photodynamic Therapy: An Update. *Molecules*, *25*(21), 5195. https://doi.org/10.3390/molecules25215195

99. Nguyen, M., Sandhu, S. S., & Sivamani, R. K. (2019). Clinical utility of daylight photodynamic therapy in the treatment of actinic keratosis - a review of the literature. *Clinical, Cosmetic and Investigational Dermatology*, *12*, 427–435. https://doi.org/10.2147/CCID.S167498

100. Heerfordt, I. M., Philipsen, P. A., & Wulf, H. C. (2022, September). Bringing the gentle properties of daylight photodynamic therapy indoors: A systematic review of efficacy and safety. *Photodiagnosis and Photodynamic Therapy*, *39*, 102858. https://doi.org/10.1016/j.pdpdt.2022.102858

101. Photodynamic Therapy for Cancer - Light Source Measurement. International Light Technologies, Inc., Peabody, Massachusetts, USA. https://internationallight.com/applications/photodynamic-therapy (Accessed: Dec 28 2023)

102. Yao, Q. (2015, December). Spectral reflectance luminous efficacy. *Optik*, *126*(24), 5790–5796. https://doi.org/10.1016/j.ijleo.2015.09.005

103. Pogue, B. W., & Hasan, T. (1997). A Theoretical Study of Light Fractionation and Dose-Rate Effects in Photodynamic Therapy. *Radiation Research*, *147*(5), 551–559. https://doi.org/10.2307/3579621

104. Shafirstein, G., Bellnier, D. A., Oakley, E., Hamilton, S., Habitzruther, M., Tworek, L., Hutson, A., Spernyak, J. A., Sexton, S., Curtin, L., Turowski, S. G., Arshad, H., & Henderson, B. (2018, October 24). Irradiance controls photodynamic efficacy and tissue heating in experimental tumours: implication for interstitial PDT of locally advanced cancer. *British Journal of Cancer*, *119*(10), 1191–1199. https://doi.org/10.1038/s41416-018-0210-y

105. Algorri, J. F., Ochoa, M., Roldán-Varona, P., Rodríguez-Cobo, L., & López-Higuera, J. M. (2021). Light Technology for Efficient and Effective Photodynamic Therapy: A Critical Review. *Cancers*, *13*(14), 3484. https://doi.org/10.3390/cancers13143484

106. Breskey, J. D., Lacey, S. E., Vesper, B. J., Paradise, W. A., Radosevich, J. A., & Colvard, M. D. (2013). Photodynamic therapy: occupational hazards and preventative recommendations for clinical administration by healthcare providers. *Photomedicine and Laser Surgery*, *31*(8), 398–407. https://doi.org/10.1089/pho.2013.3496

107. Wang, Y., Wang, Y., Wang, Y., Murray, C. K., Hamblin, M. R., Hooper, D. C., & Dai, T. (2017). Antimicrobial blue light inactivation of pathogenic microbes: State of the art. *Drug Resistance Updates*, *33-35*, 1–22. https://doi.org/10.1016/j.drup.2017.10.002

108. Balhaddad, A. A., AlQranei, M. S., Ibrahim, M. S., Weir, M. D., Martinho, F. C., Xu, H. H. K., & Melo, M. A. S. (2020). Light Energy Dose and Photosensitizer Concentration Are Determinants of Effective Photo-Killing against Caries-Related Biofilms. *International Journal of Molecular Sciences*, *21*(20), 7612. https://doi.org/10.3390/ijms21207612

109. Hubbard, S. C., & Jones, P. B. (2005, August). Ionic liquid soluble photosensitizers. *Tetrahedron*, *61*(31), 7425–7430. https://doi.org/10.1016/j.tet.2005.05.072

110. Al-Omari S. (2013). Toward a molecular understanding of the photosensitizer-copper interaction for tumor destruction. *Biophysical Reviews*, *5*(4), 305–311. https://doi.org/10.1007/s12551-013-0112-4

111. Wang, S., Zhang, C., Fang, F., Fan, Y., Yang, J., & Zhang, J. (2023). Beyond traditional light: NIR-II light-activated photosensitizers for cancer therapy. *Journal of Materials Chemistry B*, *11*(35), 8315–8326. https://doi.org/10.1039/d3tb00668a

112. Zheng, G., Chen, J., Stefflova, K., Jarvi, M., Li, H., & Wilson, B. C. (2007, May 22). Photodynamic molecular beacon as an activatable photosensitizer based on protease-controlled singlet oxygen quenching and activation. *Proceedings of the National Academy of Sciences*, *104*(21), 8989–8994. https://doi.org/10.1073/pnas.0611142104

113. Lima, E., & Reis, L. V. (2023, June 29). Photodynamic Therapy: From the Basics to the Current Progress of N-Heterocyclic-Bearing Dyes as Effective Photosensitizers. *Molecules*, *28*(13), 5092. https://doi.org/10.3390/molecules28135092

114. Li, X., Chen, L., Huang, M., Zeng, S., Zheng, J., Peng, S., Wang, Y., Cheng, H., & Li, S. (2023). Innovative strategies for photodynamic therapy against hypoxic tumor. *Asian Journal of Pharmaceutical Sciences*, *18*(1), 100775. https://doi.org/10.1016/j.ajps.2023.100775

115. Josefsen, L. B., & Boyle, R. W. (2008). Photodynamic therapy and the development of metal-based photosensitisers. *Metal-based drugs*, *2008*, 276109. https://doi.org/10.1155/2008/276109

116. Wu, W., Shao, X., Zhao, J., & Wu, M. (2017, June 23). Controllable Photodynamic Therapy Implemented by Regulating Singlet Oxygen Efficiency. *Advanced Science*, *4*(7), 1700113. https://doi.org/10.1002/advs.201700113

117. Atchison, J., Kamila, S., McEwan, C., Nesbitt, H., Davis, J., Fowley, C., Callan, B., McHale, A. P., & Callan, J. F. (2015). Modulation of ROS production in photodynamic therapy using a pH controlled photoinduced electron transfer (PET) based sensitiser. *Chemical Communications*, *51*(94), 16832-16835. https://doi.org/10.1039/C5CC07022H

118. Singh, R., Chen, D. G., Wang, C. H., Wu, C. C., Hsu, C. H., Wu, C. H., Lai, T. Y., Chou, P. T., & Chen, C. T. (2022). Tuning intramolecular charge transfer and spin–orbit coupling of AIE-active type-I photosensitizers for photodynamic therapy. *Journal of Materials Chemistry B*, *10*(32), 6228–6236. https://doi.org/10.1039/d2tb01224c

119. Pucelik, B., Sułek, A., & Dąbrowski, J. M. (2020, August). Bacteriochlorins and their metal complexes as NIR-absorbing photosensitizers: properties, mechanisms, and applications. *Coordination Chemistry Reviews*, *416*, 213340. https://doi.org/10.1016/j.ccr.2020.213340

120. Oleinick, N. L., Morris, R. L., & Belichenko, I. (2002, January). The role of apoptosis in response to photodynamic therapy: what, where, why, and how. *Photochemical & Photobiological Sciences*, *1*(1), 1–21. https://doi.org/10.1039/b108586g

121. Kessel, D., & Oleinick, N. L. (2018, January 16). Cell Death Pathways Associated with Photodynamic Therapy: An Update. *Photochemistry and Photobiology*, *94*(2), 213–218. https://doi.org/10.1111/php.12857

122. Mishchenko, T., Balalaeva, I., Gorokhova, A., Vedunova, M., & Krysko, D. V. (2022, May 13). Which cell death modality wins the contest for photodynamic therapy of cancer? *Cell Death & Disease*, *13*(5), 455. https://doi.org/10.1038/s41419-022-04851-4

123. Rajora, M. A., Lou, J. W. H., & Zheng, G. (2017). Advancing porphyrin's biomedical utility via supramolecular chemistry. *Chemical Society Reviews*, *46*(21), 6433–6469. https://doi.org/10.1039/c7cs00525c

124. Smith, K. (1984). Porphyrins, Corrins and Phthalocyanines. *Comprehensive Heterocyclic Chemistry*, *4*, 377–442. https://doi.org/10.1016/b978-008096519-2.00057-6

125. *Nanostructures for Antimicrobial Therapy*. Ficai, A., & Grumezescu, A. M. (Eds). Elsevier: Amsterdam, Netherlands (2017). https://www.sciencedirect.com/book/9780323461528/nanostructures-for-antimicrobial-therapy

126. Kumar, G., Pant, G., Hossain, K., Ahmad, A. & Alshammari, M. B. (2023) Perspectives on Usage of Functional Nanomaterials in Antimicrobial Therapy for Antibiotic-Resistant Bacterial Infections, *ACS Omega*, *8(15)*, 13492–13508. https://doi.org/10.1021/acsomega.3c00110

127. Guberman-Pfeffer, M. J., Greco, J. A., Samankumara, L. P., Zeller, M., Birge, R. R., Gascón, J. A., & Brückner, C. (2016, December 20). Bacteriochlorins with a Twist: Discovery of a Unique Mechanism to Red-Shift the Optical Spectra of Bacteriochlorins. *Journal of the American Chemical Society*, *139*(1), 548–560. https://doi.org/10.1021/jacs.6b12419

128. Pereira, N. A. M., Laranjo, M., Casalta-Lopes, J., Serra, A. C., Piñeiro, M., Pina, J., Seixas de Melo, J. S., Senge, M. O., Botelho, M. F., Martelo, L., Burrows, H. D., & Pinho e Melo, T. M. V. D. (2017, February 27). Platinum(II) Ring-Fused Chlorins as Near-Infrared Emitting Oxygen Sensors and Photodynamic Agents. *ACS Medicinal Chemistry Letters*, *8*(3), 310–315. https://doi.org/10.1021/acsmedchemlett.6b00476

129. Takahashi, T., Ogasawara, S., Shinozaki, Y., & Tamiaki, H. (2019, September 3). Synthesis of Cationic Pyridinium-(Bacterio)Chlorophyll Conjugates Bearing a Bacteriochlorin, Chlorin, or Porphyrin π-Skeleton and their Photophysical and Electrochemical Properties. *European Journal of Organic Chemistry*, *2019*(37), 6333–6340. https://doi.org/10.1002/ejoc.201901172

130. Frank, H., & Cogdell, R. (2012). 8.6 Light Capture in Photosynthesis. *Comprehensive Biophysics*, *8*, 94–114. https://doi.org/10.1016/b978-0-12-374920-8.00808-0

131. Kunieda, M., Mizoguchi, T., & Tamiaki, H. (2004, December). Syntheses and optical properties of stable 8-alkylidene-bacteriochlorins mimicking the molecular structures of natural bacteriochlorophylls-b and g. *Tetrahedron*, *60*(50), 11349–11357. https://doi.org/10.1016/j.tet.2004.09.091

132. Huang, L., Krayer, M., Roubil, J. G., Huang, Y. Y., Holten, D., Lindsey, J. S., & Hamblin, M. R. (2014, December). Stable synthetic mono-substituted cationic bacteriochlorins mediate selective broad-spectrum photoinactivation of drug-resistant pathogens at

nanomolar concentrations. *Journal of Photochemistry and Photobiology B: Biology*, *141*, 119–127. https://doi.org/10.1016/j.jphotobiol.2014.09.016

133. Pratavieira, S., Uliana, M. P., dos Santos Lopes, N. S., Donatoni, M. C., Linares, D. R., de Freitas Anibal, F., de Oliveira, K. T., Kurachi, C., & de Souza, C. W. O. (2021, June). Photodynamic therapy with a new bacteriochlorin derivative: Characterization and *in vitro* studies. *Photodiagnosis and Photodynamic Therapy*, *34*, 102251. https://doi.org/10.1016/j.pdpdt.2021.102251

134. Sindelo, A., Osifeko, O. L., & Nyokong, T. (2018, May). Synthesis, photophysicochemical and photodynamic antimicrobial chemotherapy studies of indium pyridyl phthalocyanines: Charge versus bridging atom. *Inorganica Chimica Acta*, *476*, 68–76. https://doi.org/10.1016/j.ica.2018.02.020

135. Costa-Tuna, A., Chaves, O. A., Loureiro, R. J., Pinto, S., Pina, J., & Serpa, C. (2024, January). Interaction between a water-soluble anionic porphyrin and human serum albumin unexpectedly stimulates the aggregation of the photosensitizer at the surface of the albumin. *International Journal of Biological Macromolecules*, *255*, 128210. https://doi.org/10.1016/j.ijbiomac.2023.128210

136. Dąbrowski, J. M., Pucelik, B., Regiel-Futyra, A., Brindell, M., Mazuryk, O., Kyzioł, A., Stochel, G., Macyk, W., & Arnaut, L. G. (2016, October). Engineering of relevant photodynamic processes through structural modifications of metallotetrapyrrolic photosensitizers. *Coordination Chemistry Reviews*, *325*, 67–101. https://doi.org/10.1016/j.ccr.2016.06.007

137. Bhupathiraju, N. V. S. D. K., Rizvi, W., Batteas, J. D., & Drain, C. M. (2016). Fluorinated porphyrinoids as efficient platforms for new photonic materials, sensors, and therapeutics. *Organic & Biomolecular Chemistry*, *14*(2), 389–408. https://doi.org/10.1039/c5ob01839k

138. Nsairat, H., Khater, D., Sayed, U., Odeh, F., Al Bawab, A., & Alshaer, W. (2022, May). Liposomes: structure, composition, types, and clinical applications. *Heliyon*, *8*(5), e09394. https://doi.org/10.1016/j.heliyon.2022.e09394

139. Jiang, J., Vairaprakash, P., Reddy, K. R., Sahin, T., Pavan, M. P., Lubian, E., & Lindsey, J. S. (2014). Hydrophilic tetracarboxy bacteriochlorins for photonics applications. *Organic & Biomolecular Chemistry*, *12*(1), 86–103. https://doi.org/10.1039/c3ob41791c

140. Andrade, S. M., Teixeira, R., Costa, S. M., & Sobral, A. J. (2008, March). Self-aggregation of free base porphyrins in aqueous solution and in DMPC vesicles. *Biophysical Chemistry*, *133*(1–3), 1–10. https://doi.org/10.1016/j.bpc.2007.11.007

141. Babu, B., Soy, R. C., Mack, J., & Nyokong, T. (2020). Non-aggregated lipophilic water-soluble tin porphyrins as photosensitizers for photodynamic therapy and photodynamic antimicrobial chemotherapy. *New Journal of Chemistry*, *44*(26), 11006–11012. https://doi.org/10.1039/d0nj01564d

142. Babu, B., Amuhaya, E., Oluwole, D., Prinsloo, E., Mack, J., & Nyokong, T. (2019). Preparation of NIR absorbing axial substituted tin(iv) porphyrins and their photocytotoxic properties. *MedChemComm*, *10*(1), 41–48. https://doi.org/10.1039/c8md00373d

143. Rajora, M. A., Ding, L., Valic, M., Jiang, W., Overchuk, M., Chen, J., & Zheng, G. (2017). Tailored theranostic apolipoprotein E3 porphyrin-lipid nanoparticles target glioblastoma. *Chemical Science*, *8*(8), 5371–5384. https://doi.org/10.1039/c7sc00732a

144. Senge, M. O., Sergeeva, N. N., & Hale, K. J. (2021). Classic highlights in porphyrin and porphyrinoid total synthesis and biosynthesis. *Chemical Society Reviews*, *50*(7), 4730–4789. https://doi.org/10.1039/c7cs00719a

145. Ding, L., Etemad-Moghadam, G., Cros, S., Auclair, C., & Meunier, B. (1989). Cytotoxic hybrid molecules 'metalloporphyrin–ellipticine' having a high affinity for DNA. *Journal of the Chemical Society, Chemical Communications*, *22*, 1711–1713. https://doi.org/10.1039/c39890001711

146. Gomes-da-Silva, L. C., Zhao, L., Bezu, L., Zhou, H., Sauvat, A., Liu, P., Durand, S., Leduc, M., Souquere, S., Loos, F., Mondragón, L., Sveinbjørnsson, B., Rekdal, Y.,

Boncompain, G., Perez, F., Arnaut, L. G., Kepp, O., & Kroemer, G. (2018, May 28). Photodynamic therapy with redaporfin targets the endoplasmic reticulum and Golgi apparatus. *The EMBO Journal*, *37*(13). https://doi.org/10.15252/embj.201798354

147. Nishida, K., Tojo, T., Kondo, T., & Yuasa, M. (2021, January 21). Evaluation of the correlation between porphyrin accumulation in cancer cells and functional positions for application as a drug carrier. *Scientific Reports*, *11*(1), *2046*. https://doi.org/10.1038/s41598-021-81725-3

148. Zielonka, J., Joseph, J., Sikora, A., Hardy, M., Ouari, O., Vasquez-Vivar, J., Cheng, G., Lopez, M., & Kalyanaraman, B. (2017, June 27). Mitochondria-Targeted Triphenylphosphonium-Based Compounds: Syntheses, Mechanisms of Action, and Therapeutic and Diagnostic Applications. *Chemical Reviews*, *117*(15), 10043–10120. https://doi.org/10.1021/acs.chemrev.7b00042

149. Babu, B., Mack, J., & Nyokong, T. (2022). A Sn(iv) porphyrin with mitochondria targeting properties for enhanced photodynamic activity against MCF-7 cells. *New Journal of Chemistry*, *46*(11), 5288–5295. https://doi.org/10.1039/d2nj00350c

150. Magadla, A., Babu, B., Mack, J., & Nyokong, T. (2021). Positively charged styryl pyridine substituted Zn(ii) phthalocyanines for photodynamic therapy and photoantimicrobial chemotherapy: effect of the number of charges. *Dalton Transactions*, *50*(26), 9129–9136. https://doi.org/10.1039/d1dt01047f

151. Xiao, J., Cong, H., Wang, S., Yu, B., & Shen, Y. (2021). Recent research progress in the construction of active free radical nanoreactors and their applications in photodynamic therapy. *Biomaterials Science*, *9*(7), 2384–2412. https://doi.org/10.1039/d0bm02013c

152. Xu, H., Li, S., & Liu, Y. (2022, July 11). Nanoparticles in the diagnosis and treatment of vascular aging and related diseases. *Signal Transduction and Targeted Therapy*, *7*, 231. https://doi.org/10.1038/s41392-022-01082-z

153. Augustine, S., Singh, J., Srivastava, M., Sharma, M., Das, A., & Malhotra, B. D. (2017, January 1). Recent advances in carbon based nanosystems for cancer theranostics. *Biomaterials Science*, *5*, 901–952. https://doi.org/10.1039/c7bm00008a

154. Pinals, R. L., Chio, L., Ledesma, F., & Landry, M. P. (2020). Engineering at the nano-bio interface: harnessing the protein corona towards nanoparticle design and function. *The Analyst*, *145*(15), 5090–5112. https://doi.org/10.1039/d0an00633e

155. Bhatti, R., Shakeel, H., Malik, K., Qasim, M., Khan, M. A., Ahmed, N., & Jabeen, S. (2022). Inorganic Nanoparticles: Toxic Effects, Mechanisms of Cytotoxicity and Phytochemical Interactions. *Advanced Pharmaceutical Bulletin*, *12*(4), 757–762. https://doi.org/10.34172/apb.2022.077

156. Mashima, R., & Takada, S. (2022, October 19). Lipid Nanoparticles: A Novel Gene Delivery Technique for Clinical Application. *Current Issues in Molecular Biology*, *44*(10), 5013–5027. https://doi.org/10.3390/cimb44100341

157. Zielińska, A., Carreiró, F., Oliveira, A. M., Neves, A., Pires, B., Venkatesh, D. N., Durazzo, A., Lucarini, M., Eder, P., Silva, A. M., Santini, A., & Souto, E. B. (2020, August 15). Polymeric Nanoparticles: Production, Characterization, Toxicology and Ecotoxicology. *Molecules*, *25*(16), 3731. https://doi.org/10.3390/molecules25163731

158. Patel, K. D., Singh, R. K., & Kim, H. W. (2019). Carbon-based nanomaterials as an emerging platform for theranostics. *Materials Horizons*, *6*(3), 434–469. https://doi.org/10.1039/c8mh00966j

159. Xiao, L., & Sun, H. (2018). Novel properties and applications of carbon nanodots. *Nanoscale Horizons*, *3*(6), 565–597. https://doi.org/10.1039/c8nh00106e

160. Nakamura, Y., Mochida, A., Choyke, P. L., & Kobayashi, H. (2016, September 2). Nanodrug Delivery: Is the Enhanced Permeability and Retention Effect Sufficient for Curing Cancer? *Bioconjugate Chemistry*, *27*(10), 2225–2238. https://doi.org/10.1021/acs.bioconjchem.6b00437

161. Stapleton, S., Milosevic, M., Allen, C., Zheng, J., Dunne, M., Yeung, I., & Jaffray, D. A. (2013, December 2). A Mathematical Model of the Enhanced Permeability and

Retention Effect for Liposome Transport in Solid Tumors. *PLoS ONE*, *8*(12), e81157. https://doi.org/10.1371/journal.pone.0081157

162. Liu, J., Li, R., & Yang, B. (2020, December 14). Carbon Dots: A New Type of Carbon-Based Nanomaterial with Wide Applications. *ACS Central Science*, *6*(12), 2179–2195. https://doi.org/10.1021/acscentsci.0c01306

163. Li, M., Mai, B., Wang, A., Gao, Y., Wang, X., Liu, X., Song, S., Liu, Q., Wei, S., & Wang, P. (2017). Photodynamic antimicrobial chemotherapy with cationic phthalocyanines against *Escherichia coli* planktonic and biofilm cultures. *RSC Advances*, *7*(65), 40734–40744. https://doi.org/10.1039/c7ra06073d

164. Elsayad, K. (2023, June). What Ancient Egyptian Medicine Can Teach Us. *JCO Global Oncology*, *9*, e2300146. https://doi.org/10.1200/go.23.00146

165. Tan, S., & Tatsumura, Y. (2015, July). Alexander Fleming (1881–1955): Discoverer of penicillin. *Singapore Medical Journal*, *56*(07), 366–367. https://doi.org/10.11622/smedj.2015105

166. Littman, R. J. (2009, September 28). The Plague of Athens: Epidemiology and Paleopathology. *Mount Sinai Journal of Medicine: A Journal of Translational and Personalized Medicine*, *76*(5), 456–467. https://doi.org/10.1002/msj.20137

167. Black Death: Definition, Cause, Symptoms, Effects, Death Toll, & Facts. Encyclopedia Britannica, Merriam-Webster, Chicago, Illinois, USA. https://www.britannica.com/event/Black-Death {Accessed: 28 Dec 2023}

168. Antimicrobial resistance. World Health Organization, Geneva, Switzerland. https://www.who.int/news-room/fact-sheets/detail/antimicrobial-resistance {Accessed: 28 Dec 2023}

169. Silhavy, T. J., Kahne, D., & Walker, S. (2010, April 14). The Bacterial Cell Envelope. *Cold Spring Harbor Perspectives in Biology*, *2*(5), a000414–a000414. https://doi.org/10.1101/cshperspect.a000414

170. Erickson, H. P. (2017, July 12). How bacterial cell division might cheat turgor pressure – a unified mechanism of septal division in Gram-positive and Gram-negative bacteria. *BioEssays*, *39*(8). https://doi.org/10.1002/bies.201700045

171. de Oliveira, B. P., Aguiar, C. M., & Câmara, A. C. (2014, July). Photodynamic therapy in combating the causative microorganisms from endodontic infections. *European Journal of Dentistry*, *08*(03), 424–430. https://doi.org/10.4103/1305-7456.137662

172. Lindsey, J. S., Hsu, H. C., Schreiman, I. C. (1986) Synthesis of tetraphenylporphyrins under very mild conditions, *Tetrahedron Letters*, *27(41)*, 4969–4970. https://doi.org/10.1016/S0040-4039(00)85109-6

173. Koifman, O. I., & Ageeva, T. A. (2022, April). Main Strategies for the Synthesis of *meso*-Arylporphyrins. *Russian Journal of Organic Chemistry*, *58*(4), 443–479. https://doi.org/10.1134/s1070428022040017

174. Rothemund, P. (1935, October). Formation of porphyrins from pyrrole and aldehydes. *Journal of the American Chemical Society*, *57*(10), 2010–2011. https://doi.org/10.1021/ja01313a510

175. Senge, M. O. (2001). Highly Substituted Porphyrins. *Handbook of Porphyrin Science*, *Vol. 1*, Kadish K. M.; Smith, K. M.; Guilard, R., (Eds.), Academic Press, Cambridge, Massachusetts, USA.

176. Adler, A. D., Longo, F. R., Finarelli, J. D., Goldmacher, J., Assour, J., & Korsakoff, L. (1967, February). A simplified synthesis for *meso*-tetraphenylporphine. *The Journal of Organic Chemistry*, *32*(2), 476–476. https://doi.org/10.1021/jo01288a053

177. Shy, H., Mackin, P., Orvieto, A. S., Gharbharan, D., Peterson, G. R., Bampos, N., & Hamilton, T. D. (2014). The two-step mechanochemical synthesis of porphyrins. *Faraday Discussions*, *170*, 59–69. https://doi.org/10.1039/c3fd00140g

178. Pineiro, M. (2014, April). Microwave-Assisted Synthesis and Reactivity of Porphyrins. *Current Organic Synthesis*, *11*(1), 89–109. https://doi.org/10.2174/15701794113106660088

179. Moura, N. M. M., Monteiro, C. J. P., Tomé, A. C., Neves, M. G. P. M. S., & Cavaleiro, A. J. A. S. (2022, January 14). Synthesis of chlorins and bacteriochlorins from cycloaddition reactions with porphyrins. *Arkivoc*, *2022*(2), 54–98. https://doi.org/10.24820/ark.5550190.p011.696

180. Pereira, M. M., Abreu, A. R., Goncalves, N. P. F., Calvete, M. J. F., Simões, A. V. C., Monteiro, C. J. P., Arnaut, L. G., Eusébio, M. E., & Canotilho, J. (2012). An insight into solvent-free diimide porphyrin reduction: a versatile approach for *meso*-aryl hydroporphyrin synthesis. *Green Chemistry*, *14*(6), 1666. https://doi.org/10.1039/c2gc35126a

181. Dukh, M., Tabaczynski, W. A., Seetharaman, S., Ou, Z., Kadish, K. M., D'Souza, F., & Pandey, R. K. (2020, October 22). *meso*- and β-Pyrrole-Linked Chlorin-Bacteriochlorin Dyads for Promoting Far-Red FRET and Singlet Oxygen Production. *Chemistry – A European Journal*, *26*(65), 14996–15006. https://doi.org/10.1002/chem.202003042

182. Jing, H., Tang, Q., Bocian, D. F., & Lindsey, J. S. (2022, February 7). De Novo Synthesis of Bacteriochlorins Bearing Four Trideuteriomethyl Groups. *Organics*, *3*(1), 22–37. https://doi.org/10.3390/org3010002

183. Brueckner, C., Samankumara, L., & Ogikubo, J. (2012). Syntheses of Bacteriochlorins and Isobacteriochlorins. *Handbook of Porphyrin Science*, *Vol. 17*, Kadish K. M.; Smith, K. M.; Guilard, R., (Eds.), World Scientific, Singapore. https://doi.org/10.1142/9789814335508_0003

184. Lindsey, J. S., & Woodford, J. N. (1995, March). A Simple Method for Preparing Magnesium Porphyrins. *Inorganic Chemistry*, *34*(5), 1063–1069. https://doi.org/10.1021/ic00109a011

185. Fuhrhop, J. H., & Mauzerall, D. (1969, July). One-electron oxidation of metalloporphyrins. *Journal of the American Chemical Society*, *91*(15), 4174–4181. https://doi.org/10.1021/ja01043a027

186. Yao, S. A., Hansen, C. B., & Berry, J. F. (2013, July). A convenient, high-yielding, chromatography-free method for the insertion of transition metal acetates into porphyrins. *Polyhedron*, *58*, 2–6. https://doi.org/10.1016/j.poly.2012.05.038

187. Alves, E., Costa, L., Carvalho, C., Tomé, J. P. C., Faustino, M. A. F., Neves, M. G. P. M. S., Tomé, A. C., Cavaleiro, J. A. S., Cunha, N., & Almeida, A. (2009, April 15). Charge effect on the photoinactivation of Gram-negative and Gram-positive bacteria by cationic *meso*-substituted porphyrins. *BMC Microbiology*, *9*, 70. https://doi.org/10.1186/1471-2180-9-70

188. Chiyumba, C. (2022) MSc thesis. Rhodes University, Makhanda, South Africa.

189. Tran Thi, T. H., Desforge, C., Thiec, C., & Gaspard, S. (1989, February). Singlet-singlet and triplet-triplet intramolecular transfer processes in a covalently linked porphyrin-phthalocyanine heterodimer. *The Journal of Physical Chemistry*, *93(4)*, 1226–1233. https://doi.org/10.1021/j100341a013

190. Openda, Y. I., Ngoy, B. P., & Nyokong, T. (2021, March 11). Photodynamic Antimicrobial Action of Asymmetrical Porphyrins Functionalised Silver-Detonation Nanodiamonds Nanoplatforms for the Suppression of *Staphylococcus aureus* Planktonic Cells and Biofilms. *Frontiers in Chemistry*, *9*, 628316. https://doi.org/10.3389/fchem.2021.628316

191. Gaussian 09, Revision E.01, Frisch, M. J., Trucks, G. W., Schlegel, H. B., Scuseria, G. E., Robb, M. A., Cheeseman, J. R., Scalmani, G., Barone, V., Mennucci, B., Petersson, G. A., Nakatsuji, H., Caricato, M., Li, X., Hratchian, H. P., Izmaylov, A. F., Bloino, J., Zheng, G., Sonnenberg, J. L., Hada, M., Ehara, M., Toyota, K., Fukuda, R., Hasegawa, J., Ishida, M., Nakajima, T., Honda, Y., Kitao, O., Nakai, H., Vreven, T., Montgomery, J. A., Jr., Peralta, J. E., Ogliaro, F., Bearpark, M., Heyd, J. J., Brothers, E., Kudin, K. N., Staroverov, V. N., Kobayashi, R., Normand, J., Raghavachari, K., Rendell, A., Burant, J. C., Iyengar, S. S., Tomasi, J., Cossi, M., Rega, N., Millam, J. M., Klene, M., Knox, J. E., Cross, J. B., Bakken, V., Adamo, C., Jaramillo, J., Gomperts,

R., Stratmann, R. E., Yazyev, O., Austin, A. J., Cammi, R., Pomelli, C., Ochterski, J. W., Martin, R. L., Morokuma, K., Zakrzewski, V. G., Voth, G. A., Salvador, P., Dannenberg, J. J., Dapprich, S., Daniels, A. D., Farkas, Ö., Foresman, J. B., Ortiz, J. V., Cioslowski, J. & Fox, D. J. Gaussian, Inc., Wallingford CT, 2009.

192. Mack, J. (2017) Expanded, Contracted, and Isomeric Porphyrins: Theoretical Aspects. *Chemical Reviews*, *117*, 3444–3478. http://dx.doi.org/10.1021/acs.chemrev.6b00568

193. Gouterman, M., Wagnière, G. H. & Snyder, L. C. (1963) Spectra of porphyrins: Part II. Four orbital model. *Journal of Molecular Spectroscopy*, *11(1–6)*, 108–127. https://doi.org/10.1016/0022-2852(63)90011-0

194. Michl, J. (1984) Magnetic circular dichroism of aromatic molecules. *Tetrahedron*, *40(20)*, 3845– 3934. https://doi.org/10.1016/S0040-4020(01)99999-5

195. Xie, J., Wang, Y., Choi, W., Jangili, P., Ge, Y., Xu, Y., Kang, J., Liu, L., Zhang, B., Xie, Z., He, J., Xie, N., Nie, G., Zhang, H., & Kim, J. S. (2021). Overcoming barriers in photodynamic therapy harnessing nano-formulation strategies. Chemical Society Reviews, 50(16), 9152–9201. https://doi.org/10.1039/d0cs01370f

196. Hutchings, M. I., Truman, A. W., & Wilkinson, B. (2019, October). Antibiotics: past, present and future. Current Opinion in Microbiology, 51, 72–80. https://doi.org/10.1016/j.mib.2019.10.008

197. Pajerski, W., Ochonska, D., Brzychczy-Wloch, M., Indyka, P., Jarosz, M., Golda-Cepa, M., Sojka, Z., & Kotarba, A. (2019, August). Attachment efficiency of gold nanoparticles by Gram-positive and Gram-negative bacterial strains governed by surface charges. Journal of Nanoparticle Research, 21(8). https://doi.org/10.1007/s11051-019-4617-z